THE UNIVERSITY OF CHICAGO

THE CHEMICAL AND PHYSICAL PROPERTIES OF CARBON-BEARING PHASES IN THE DEEP EARTH

A DISSERTATION SUBMITTED TO

THE FACULTY OF THE DIVISION OF THE PHYSICAL SCIENCES

IN CANDIDACY FOR THE DEGREE OF

DOCTOR OF PHILOSOPHY

DEPARTMENT OF THE GEOPHYSICAL SCIENCES

BY

ANNE HOPE DAVIS

CHICAGO, ILLINOIS

MARCH 2022

TABLE OF CONTENTS

LIST OF FIGURES

LIST OF TABLES

ACKNOWLEDGMENTS

I would like to thank my committee members for their support and assistance: Andrew J. Campbell (the University of Chicago), Dion L. Heinz (the University of Chicago), Fred J. Ciesla (the University of Chicago), Andrew M. Davis (the University of Chicago), and Razvan Caracas (Université de Paris). I would also like to acknowledge the students and postdocs I have had the pleasure to work with, with special thanks to Natalia Solomatova and Lily Thompson for taking me under their wings. A huge thank you to my family for their encouragement and support over the years. And finally, a thank you to Jack Arnold, whose kindness and patience is boundless and who never fails to amuse me.

ABSTRACT

Carbon is ubiquitous throughout the Earth's surface, but plays an important role in the Earth's interior as well. Carbon is known to influence a host of physical properties in minerals and melts, including melting temperature (Dasgupta et al., 2007), electrical conductivity (Gaillard et al., 2008), density (Solomatova and Caracas, 2021), and rheology (Stagno et al., 2018). However, much is still unknown about the deep Earth carbon cycle, from the amount of carbon contained in the Earth to the distribution of carbon between the upper mantle, lower mantle, and core. Improving our understanding of the phases that host carbon in the Earth and their potential interactions with other phases is crucial to understanding the processes that govern carbon distribution in the deep Earth. Equipped with this knowledge, we can better predict the fate of carbon in the Earth's deep interior and explain observable geophysical phenomena.

This thesis focuses on the fate of carbonates, which are regularly introduced into the Earth's mantle in subducting slabs (Sano and Williams, 1996), and thus, serve as a constant source of carbon into the mantle. Previous studies of carbonates in the lower mantle focus on the stability of carbonates in isolation (Biellmann et al., 1993; Cerantola et al., 2017; Santos et al., 2019), but this research aims to investigate carbon stability in a more realistic petrologic context. In this thesis, I outline a possible delivery mechanism of carbonates into the lower mantle by reacting carbonates with iron alloys and exploring their stability fields. I then investigate the fate of carbonate phases in the lower mantle by examining the interaction of carbonate melts with silicate and metal melts. This research indicates that carbonate-silicate-metal melts could be parent melts for diamonds and iron carbides, as carbon forms complex polymers with high degrees of C-Fe bonding. Finally, this thesis concludes by investigating the densities and

miscibilities of carbonate-silicate-metal melts as a possible explanation for ultralow velocity zones (ULVZs), which have been proposed to be gravitationally stable pockets of partial melt situated at the core-mantle boundary (Williams and Garnero, 1996).

CHAPTER 1

CARBON IN THE DEEP EARTH

Carbon plays an important role at Earth's surface as a vital part of the biosphere and the atmosphere, but its role in the Earth's interior is less well understood. The amount of carbon contained in the Earth is relatively unknown, with reports varying from 120 ppm (McDonough and Sun, 1995) to 526 ppm (Marty, 2012). However, knowing the amount of carbon and its relative distribution between layers of the Earth is important, as carbon is known to influence a host of processes in the Earth's interior. In particular, carbon has a reported effect on the melting temperatures of minerals (Dasgupta and Hirschmann, 2010; Dasgupta et al., 2007), rheology (Stagno et al., 2018), electrical conductivity (Ghosh and Karki, 2017), atomic diffusivity (Hayden and Watson, 2008), and elemental partitioning (Dalou et al., 2009). Additionally, carbon is a major component of geologically interesting phases in the Earth's interior, such as diamond and iron carbide, whose physical properties can be used to explain lower mantle processes (Smit et al., 2019) and seismological observations (Prescher et al., 2015). Despite the importance of carbon, however, there are still unanswered questions about its role in the Earth's interior, from the amount of carbon, to its distribution, to the phase relations of carbon-bearing phases in the mantle and core.

Carbon has an established role in the upper mantle that has been well-studied (Dasgupta and Hirschmann, 2006; Manning et al., 2013; Sun and Dasgupta, 2019). Carbon is regularly introduced to the upper mantle through subduction of oceanic lithosphere (Hammouda, 2003; Presnall and Gudfinnsson, 2005) and is directly recycled from the mantle to the atmosphere through volcanic degassing of CO_2 (Kerrick, 2001). Similarly, carbon is thought be a component

of the Earth's core (Prescher et al., 2015; Wood et al., 2013; Zhang and Yin, 2012). In fact, it has been calculated that more than 90 percent of Earth's carbon is stored in the core (Javoy, 1997; McDonough, 2003), due to the highly siderophile nature of carbon established through metal-silicate partitioning experiments (Armstrong et al., 2015; Chi et al., 2014; Li et al., 2015). The amount and role of carbon in the lower mantle, however, is more unclear. Carbon in the lower mantle is thought to come from two sources: 1) primordial remnants of a magma ocean (Labrosse et al., 2007), or 2) carbonates preserved in subducting slabs (Dorfman et al., 2018; Korsakov and Hermann, 2006; Lv et al., 2021). Previous studies would indicate that this is a relatively small amount of carbon, due to the highly siderophile nature of carbon that would result in the transport of primordial carbon to the core during core-mantle differentiation, and due also to the tendency for carbonates in subducting slabs to melt or decarbonate before entering the lower mantle (Takafuji et al., 2006; Thomson et al., 2016). However, more recent studies indicate that more carbon may be present in the lower mantle than previously thought. New measurements of carbon partitioning coefficients imply that carbon is less siderophile at high pressure than initial reports indicated (Fichtner et al., 2021; Fischer et al., 2020; Grewal et al., 2021), allowing for more carbon to be stored in the mantle during core-mantle differentiation. Additionally, carbonate inclusions found in diamonds returned from the lower mantle indicate that carbonates are stable and present under lower mantle conditions (Agrosì et al., 2019; Korsakov and Hermann, 2006), indicating that a pathway may exist in which carbonates are preserved to the lower mantle in a subducting slab.

This thesis explores the role and the fate of carbonates in the lower mantle and at the core-mantle boundary. Carbonates are a particularly interesting carbon-bearing phase in the deep

Earth. They are constantly subducted into the mantle, and thus provide a link between the Earth's interior and atmosphere, which has interesting implications when considering the future of carbon storage in the Earth and the evolution of Earth's atmosphere (Hayes and Waldbauer, 2006). Additionally, carbonate minerals exhibit intriguing behavior under pressure. Carbonates melt at relatively low temperatures (Li et al., 2017b), creating carbonatitic melt compositions with unusually low viscosities (Stagno et al., 2018) and high electrical conductivities (Gaillard et al., 2008). Carbon's bonding versatility allows it to behave as either a cation or an anion (Sen et al., 2013; Solomatova et al., 2019) depending on the chemical context, which leads to interesting redox reactions. Finally, carbonate minerals are also known to undergo phase transitions in the lower mantle, transitioning from sp^2 hybridized carbon to sp^3 (Boulard et al., 2015; Merlini et al., 2012) at around 80 GPa for $MgCO_3$ (Boulard et al., 2011; Isshiki et al., 2004; Oganov et al., 2008) and between 105 and 130 GPa for $CaCO_3$ (Lobanov et al., 2017; Oganov et al., 2006; Ono et al., 2007). This change in carbonate structure from a triangular coordination to a tetrahedral coordination marks a profound change in the petrological and the geochemical behavior of carbonate minerals and melts, such that lower pressure studies may not accurately predict carbonate behavior in the lowermost mantle.

Previous studies of carbonates in the lower mantle tend to focus on the behavior of carbonate minerals in isolation (Biellmann et al., 1993; Mao et al., 2011; Merlini et al., 2017; Vennari and Williams, 2018). However, the stability of carbonates depends on a host of thermodynamic variables, including pressure, temperature, oxygen fugacity, and reactivity with other mantle phases. Studying carbonates in conjunction with common mantle phases is key to understanding their stability and reactivity in a realistic mantle environment. Some studies

represent progress along this front. Carbonates have been reacted with iron in the upper mantle as a mechanism for diamond formation (Martirosyan et al., 2015a; Martirosyan et al., 2015b; Martirosyan et al., 2016; Palyanov et al., 2013). Reactions of carbonates with metal in the lower mantle have yielded diamond, Fe_3C, and Fe_7C_3 (Dorfman et al., 2018; Zhu et al., 2019). Lv et al. (2021) found carbonate stability when reacting carbonates and silicates, and Gavryushkin et al. (2021) found that carbonates reacting with MgO formed Mg_2CO_4. However, there are no previous lower mantle experimental studies that involve silicon, carbon, and iron in the same system. Silicon is an important component of lower mantle phase assemblages, as bridgmanite ($MgSiO_3$) is the most abundant mineral in the Earth's lower mantle. Iron is a less obvious component of lower mantle phase assemblages. Metallic iron is abundant at the core-mantle boundary, but could also be present throughout the lower mantle due to iron disproportionation (Frost et al., 2004). Most iron in the upper mantle is Fe^{2+}, but bridgmanite in the lower mantle has a chemical preference for Fe^{3+} due to the coupled substitution of Al^{3+} and Fe^{3+} for Mg^{2+} and Si^{4+}. Bridgmanite's chemical preference for Fe^{3+} results in the disproportionation of Fe^{2+} into Fe^{3+} and Fe^0. Estimates from the Fe^{3+}/total Fe ratio in bridgmanite result in ~1 wt% of metallic Fe contained in the lower mantle (Frost et al., 2004), implying that metallic iron could play an important role throughout the Earth's lower mantle. Thus, petrologic studies of carbonates in conjunction with both silicates and metals are important to constrain the behavior of carbonates in the lower mantle.

In this thesis, I use both experimental and computational methods to study carbonate reactions with silicates and metals. In Chapter 2, I utilize experimental methods to investigate solid carbonate reactions with iron alloys and use the results to propose a possible

delivery mechanism for carbonates into the Earth's lower mantle. The mantle is chemically heterogenous and structurally complex (Stracke, 2012), which allows for carbonate stability to be dictated by conditions set by local redox chemistry. Thus, I investigate the behavior of carbonates in an example lower mantle phase assemblage as a proxy for the types of conditions that could exist in the Earth's interior today. The analysis of the reactions results in a phase diagram illustrating the conditions under which carbonates are stable. A direct comparison of this phase diagram to known conditions in the Earth's lower mantle illustrates how carbonates may remain stable in a subducting slab to the Earth's lowermost mantle.

In Chapters 4 and 5, I use computational methods to examine carbonate melt reactions in the lower mantle and at the core-mantle boundary. Carbonate minerals not only melt at relatively low temperatures (Thomson et al., 2016), but their presence is known to cause melting point depression in silicates (Dasgupta et al., 2013). Thus, solid or molten carbonates transported to the lower mantle in subducting slabs likely interact with silicate and metal melt phases, particularly at the core-mantle boundary. In Chapter 4, I examine in detail speciation and coordination changes in a carbonate-silicate-metal melt with pressure. The composition studied is $Mg_{24}Si_{12}C_{12}O_{72}Fe_{13}$, which translates to 12 $MgSiO_3$ units, 12 $MgCO_3$ units, and 13 Fe units. Most previous studies examine carbonate melts (Li et al., 2017b; Xu et al., 2020), or carbon-bearing silicate melts (Bajgain and Mookherjee, 2021; Ghosh et al., 2017; Ghosh and Karki, 2017; Ghosh et al., 2007), but this study examines a composition with subequal amounts of carbon, silicon, and metal, which has never been studied with *ab initio* methods before. This study is also one of a handful that examines carbon in the presence of iron in a deep Earth melt (Karki et al., 2020; Solomatova and Caracas, 2021; Solomatova et al., 2019). From the speciation

and coordination analysis, I evaluate the evolving role of carbon in the melt network, identify possible exsolving phases from a melt of this composition, quantify redox exchange within the melt, examine atomic diffusivities, and finally, evaluate the electronic structure of the melt.

In Chapter 5, I examine the densities and miscibilities of carbonate-silicate-metal melts as a possible explanation for ultralow velocity zones (ULVZs). ULVZs are areas with low P- and S-wave velocities (reduced by up to 10 and 30 percent respectively) and increased densities imaged directly above the core-mantle boundary. They are typically hundreds of kilometers wide but only 5 to 40 km thick (Garnero and McNamara, 2008). Many explanations exist to explain ULVZs (Garnero and McNamara, 2008; Li et al., 2017a; Thompson et al., 2021; Williams and Garnero, 1996), but a popular explanation posits that they are gravitationally stable melt structures (Williams and Garnero, 1996). Melt is a likely explanation for ULVZs due to the 3:1 ratio of S-to-P wave velocity reduction found in ULVZs (Garnero and McNamara, 2008; Williams and Garnero, 1996) and the general association with the edges of large low velocity provinces (LLVPs), which are thought to be the hottest regions along the core-mantle boundary (Garnero and McNamara, 2008). Thus, gravitationally stable carbonate-silicate-melt compositions could serve as an explanation for these seismically observed phenomena. Through my analysis of the densities of various melt mixtures, I identify melt compositions that are both miscible and denser than the surrounding mantle, giving a host of possible ULVZ compositions. Additionally, I identify immiscible melt compositions and evaluate bond abundances within the melts to identify species exsolution. The implications of this work for carbon storage in the deep Earth are evaluated.

Finally, there are other projects I have worked on over the course of my tenure as a PhD student, but their results have been excluded as they are thematically distant from this thesis.

CHAPTER 2

CARBONATE-METAL REACTIONS IN THE LOWER MANTLE

2.1 Introduction

The storage and the cycling of carbon in the deep Earth are intimately connected to the Earth's formation and development throughout geologic time. Carbonates are components of subducting slabs, making them important carriers of carbon into the mantle and important players in the deep Earth carbon cycle (Dasgupta and Hirschmann, 2010; Dobretsov and Shatskiy, 2012). In the upper mantle, carbonates are known to undergo a host of processes including pressure-induced phase transitions (Arapan and Ahuja, 2010; Gavryushkin et al., 2017; Ono et al., 2005), melting to form carbonatite melts (Dalou et al., 2009; Li et al., 2017; Xu et al., 2020), decarbonation reactions with free silica (Drewitt et al., 2019; Kakizawa et al., 2015; Li et al., 2018), and redox reactions with silicates, metals, and oxides to form diamond and/or carbide (Brey et al., 1983, Palyanov et al., 2013; Rohrbach and Schmidt, 2011). Studies on carbonates and their stability in upper mantle phase assemblages have been plentiful (Kushiro, 1975; Martirosyan et al., 2015; Thomson et al., 2016). However, similar petrologic studies on carbonates in the lower mantle are lacking, with a few notable exceptions (Dorfman et al., 2018; Lv et al., 2021; Zhu et al., 2019).

The dearth of petrologic lower mantle carbonate studies stems partly from differing views on the amount of carbon contained in the lower mantle and the stability of carbonates at lower mantle conditions. Out of an estimated yearly total of 62 megatons of carbonate subducted per year (Clift, 2017), estimates on the amount of carbon contained in carbonates that are subducted into the lower mantle vary from 0.0001 to 52 megatons yearly (Dasgupta and Hirschmann, 2010;

Kelemen and Manning, 2015), and estimates of primordial carbon contained in the mantle vary from 30 to 1000 ppm (Dasgupta and Hirschmann, 2010). Additionally, carbonate stability has been shown to depend on pressure (Kraft et al., 1991; Oganov et al., 2008), temperature (Biellmann et al., 1993; Cerantola et al., 2017), and oxygen fugacity (Rohrbach and Schmidt, 2011; Stagno et al., 2013). Under reducing conditions, carbonates have been shown to reduce to diamond and/or carbide phases (Dorfman et al., 2018; Palyanov et al., 2013; Zhu et al., 2019). The instability of carbonates under reducing conditions has led to the redox-freezing hypothesis (Rohrbach and Schmidt, 2011; Stagno et al., 2011), which suggests that the mantle becomes increasingly metal-saturated and reducing with depth, forcing carbon to transition from an oxidized to a reduced form.

Alternatively, it can be argued that because the mantle is chemically heterogeneous (Stracke, 2012), carbonate stability may depend on redox conditions set by local chemistry. Carbonate inclusions in deep Earth diamonds (Kaminsky et al., 2009; Korsakov and Hermann, 2006) and constraints on the kinetics of carbonate-metal redox reactions (Martirosyan et al., 2016) provide evidence that carbonates could be stable and present in the lower mantle. Thus, to fully evaluate carbonate stability in the lower mantle, it is necessary to study carbonates under relevant pressures, temperatures, and oxygen fugacities as set by lower mantle mineral phase assemblages. Past petrologic studies of carbonates at lower mantle conditions have been scarce. Dorfman et al. (2018) reacted $(Mg,Ca)CO_3$ and Fe to produce a mixture of diamond, Fe_7C_3, and (Mg,Fe)O and found that $CaCO_3$ was preserved to deep mantle conditions. Zhu et al. (2019) found that reactions between $MgCO_3$ and Fe produce diamond, and that the rate of the reaction depends positively on temperature and negatively on pressure. Lv et al. (2021) reacted carbonate

and silicate together and found a reversible cation exchange reaction that preserved $CaCO_3$ over $MgCO_3$. However, more petrologic studies of carbonates at lower mantle conditions are necessary as the behavior of lower mantle minerals is complicated by phase transitions, coordination changes, and melting that could significantly affect their chemical and physical properties.

Thus, we present results from petrology experiments on carbonate-metal redox reactions in the laser heated diamond anvil cell to determine the stable carbon-bearing phase in an example lower mantle phase assemblage. We react either magnesite ($MgCO_3$) or calcite ($CaCO_3$) with Fe_3Si at pressures up to 123 GPa and temperatures up to 3200 K. Iron-silicon alloy is selected as a reactant due to the presumed presence of Fe in the lower mantle through disproportionation reactions (Frost et al., 2004) and as a candidate phase in the Earth's outer core (Fischer et al., 2012). By selecting Fe_3Si as a reactant, we also introduce silicon into the system, allowing us to directly compare our results to the work of Dorfman et al. (2018) and Zhu et al. (2019) and elucidate the role of silicon in carbonate-metal reactions.

2.2 Methods

The $CaCO_3$ used in this study was obtained either from Sigma Aldrich (Lot D380C128, anhydrous) or from an optically pure natural calcite sample of composition $(Ca_{0.99992}Sr_{0.00008})CO_3$. Natural samples of magnesite were from Snarum, Norway (University of Chicago mineral collection, number 3733) with composition $(Mg_{0.95}Ca_{0.03}Fe_{0.02})CO_3$. Carbonate compositions were confirmed by X-ray fluorescence and structures were confirmed by Raman spectroscopy, performed at the University of Chicago. The Fe-Si alloy (Fe_3Si) used in the study

contained 15.9 wt% silicon ($Fe_{0.73}Si_{0.27}$ by mole), based on electron microprobe measurements at the University of Maryland, and was chemically homogenous (Fischer et al., 2014). All starting materials were individually ball milled for 1.5 hours at 20 Hz in a tungsten carbide (WC) capsule.

Samples were then loaded using one of the following 2 configurations: 1) $CaCO_3$ and Fe_3Si were blended together in a 1:1 molar ratio in a WC capsule using a ball mill at 20 Hz for 1.5 hours. The mixture was then pressed between diamonds to form platelets 5-10 μm thick and approximately 50 μm in diameter. Argon, used as a hydrostatic pressure medium and pressure standard, was loaded cryogenically as a liquid; 2) Fe_3Si was pressed between diamonds to form platelets 5-10 μm thick and approximately 50 μm in diameter. Fe_3Si was loaded between powdered samples of either $CaCO_3$ or $MgCO_3$, with no additional pressure medium. Both configurations used rhenium gaskets preindented to ~28 GPa in symmetric diamond-anvil cells (DACs), and diamonds with culet sizes of 250 or 150 microns were used depending on the pressure range. Prepared sample assemblies were baked for 30 minutes at 100 °C prior to closing the DACs to mitigate the effect of water absorption.

X-ray diffraction experiments were performed at 13-ID-D (GSECARS) at the Advanced Photon Source, Argonne National Laboratory. Experiments were performed at pressures between 28-123 GPa and up to 3208 K (see Table 2.1 for experimental conditions). Laser-heating experiments were performed with a monochromatic incident X-ray (λ = 0.3344 Å or 0.2952 Å) of area 3×4 μm at full-width at half maximum of the focused spot. Sample-to-detector distances and tilt were calibrated using 1-bar diffraction of LaB_6. Integration of diffraction patterns to produce 2θ plots was performed using DIOPTAS (Prescher and Prakapenka, 2015). Positions of

individual diffraction peaks were determined using PeakFit (Systat Software) by fitting individual peaks to single Gaussian curves. In samples containing argon, pressures in laser-heated samples were determined using the Ross et al. (1986) equation of state for argon with temperatures adjusted for axial temperature gradients within the insulator as described by Campbell et al. (2009). For samples without an argon pressure standard, pressures were measured before and after laser heating using diamond edge Raman (Akahama and Kawamura, 2006), with additional thermal pressure (15-20% of the pre-heating pressure) estimated based on previous experiments with a similar geometry (Fischer et al., 2015).

Sample	Pressure(GPa)	Maximum Temperature (K)	Pressure medium	Reactants	Products
AD7	28	2419	Ar	Fe_3Si, $CaCO_3$-VII	$CaSiO_3$, Fe_3C, Fe_7C_3, FeO, SiO_2, CaO
AD1	32	1632	Ar	Fe_3Si, $CaCO_3$-VII	$CaSiO_3$, (Fe,Ca)O
AD7	38	2544	Ar	Fe_3Si, $CaCO_3$ (post-aragonite)	$CaSiO_3$, Fe_3C, Fe_7C_3, FeO, SiO_2, CaO
AD1	39	2172	Ar	Fe_3Si, $CaCO_3$ (post-aragonite)	$CaSiO_3$, (Fe,Ca)O
AD22	40	1633	None	Fe_3Si, $CaCO_3$ (post-aragonite)	$CaSiO_3$, Fe_3C, Fe_7C_3, FeO, SiO_2, CaO
AD1	47	2423	Ar	Fe_3Si, $CaCO_3$ (post-aragonite)	$CaSiO_3$, (Fe,Ca)O
AD7	52	2843	Ar	Fe_3Si, $CaCO_3$ (post-aragonite)	$CaSiO_3$, Fe_3C, Fe_7C_3, FeO, CaO, SiO_2
AD7	52	3168	Ar	Fe_3Si, $CaCO_3$ (post-aragonite)	$CaSiO_3$, Fe_3C, Fe_7C_3, FeO, CaO, SiO_2
AD1	57	2567	Ar	Fe_3Si, $CaCO_3$ (post-aragonite)	$CaSiO_3$, Fe_3C
AD58	79	2970	None	Fe_3Si, $CaCO_3$ (post-aragonite)	$CaSiO_3$, Fe_3C, Fe_7C_3, FeO, CaO, SiO_2
AD58	103	3107	None	Fe_3Si, $CaCO_3$ ($P2_1/c$)	$CaSiO_3$, Fe_3C, Fe_7C_3, FeO, CaO, SiO_2
AD58	123	3208	None	Fe_3Si, $CaCO_3$ ($P2_1/c$)	$CaSiO_3$, Fe_3C, Fe_7C_3, FeO, CaO, SiO_2
AD54	33	2214	None	Fe_3Si, $MgCO_3$	$MgSiO_3$, Fe_3C, Fe_7C_3, (Mg,Fe)O, SiO_2
AD59	42	2706	None	Fe_3Si, $MgCO_3$	$MgSiO_3$, Fe_3C, Fe_7C_3, (Mg,Fe)O, SiO_2
AD54	46	2571	None	Fe_3Si, $MgCO_3$	$MgSiO_3$, Fe_3C, Fe_7C_3, (Mg,Fe)O, SiO_2
AD54	53	2526	None	Fe_3Si, $MgCO_3$	$MgSiO_3$, Fe_3C, Fe_7C_3, (Mg,Fe)O, SiO_2
AD59	54	2785	None	Fe_3Si, $MgCO_3$	$MgSiO_3$, Fe_3C, Fe_7C_3, (Mg,Fe)O, SiO_2
AD54	63	2451	None	Fe_3Si, $MgCO_3$	$MgSiO_3$, Fe_3C, Fe_7C_3, (Mg,Fe)O, SiO_2
AD59	66	2733	None	Fe_3Si, $MgCO_3$	$MgSiO_3$, Fe_3C, Fe_7C_3, (Mg,Fe)O, SiO_2
AD59	77	3040	None	Fe_3Si, $MgCO_3$	$MgSiO_3$, Fe_3C, Fe_7C_3, (Mg,Fe)O, SiO_2

Table 2.1: Experimental conditions for the $CaCO_3$ reaction (orange) and the $MgCO_3$ reaction (blue). Products are phases identified upon quench.

For sample recovery experiments, samples were decompressed and secured within the gasket to 0.5" aluminum SEM pin stubs. They were coated with a thin (~10 nm) layer of carbon to provide a conductive surface for electron beam imaging. Samples were sectioned along the axis of compression through the center of the laser-heated spot using a TESCAN LYRA3 focused ion beam – scanning electron microscope (FIB-SEM) at the University of Chicago. The sample regions were fortified by a platinum strip deposited on top of the section, attached to a tungsten needle, and removed from the sample chamber. The FIB sections were secured to copper TEM grids and thinned to less than 0.5 μm. Chemical analysis was performed on the same instrument using an Oxford energy dispersive X-ray spectrometer (EDS) equipped with two XMax 80 mm^2 silicon drift detectors and Aztec software using a 10 keV electron beam.

2.3 Results

We heat $CaCO_3$ or $MgCO_3$ and Fe_3Si to produce the following carbon, silicon exchange reactions,

$$CaCO_3 + Fe_3Si \rightarrow CaSiO_3 + Fe_3C$$

$$MgCO_3 + Fe_3Si \rightarrow MgSiO_3 + Fe_3C \quad (2.1)$$

Carbon and silicon exchange to form either bridgmanite or davemaoite and iron carbide. In this reaction, an oxidized form of carbon, carbonate, is on the left side of the equation while a reduced form of carbon, carbide, is on the right side of the equation. Evaluating whether this reaction proceeds at the pressure and temperature conditions of the mantle allows us to determine whether carbonate or carbide is the stable carbon-bearing phase in the mantle.

2.3.1 XRD Results

Both reactants and products were identified through powder X-ray diffraction (Figure 2.1 and Figure 2.2) and EDS measurements (Figure 2.3 and Figure 2.4). Samples are compressed to a target pressure and X-ray diffraction is used to measure the sample before, during, and after laser heating experiments. Figure 2.1 displays example diffraction patterns for the $CaCO_3$ reaction at 54 GPa before (Figure 2.1a) and after (Figure 2.1b) reaction. Before reaction, peaks from the starting materials, Fe_3Si and $CaCO_3$, and the pressure medium, Ar, are present. Fe_3Si adopts the B2 structure (Fischer et al., 2012), while $CaCO_3$ adopts the orthorhombic $P2_12_12$ post-aragonite structure (Ono et al., 2005). After reaction, many more peaks are present. There are still peaks corresponding to argon, but there are also peaks corresponding to unreacted Fe_3Si, indicating that the reaction did not go to completion. The incompleteness of the reaction is evident in the SEM image as well (Figure 2.3), which shows that a large axial temperature gradient was present throughout the sample, allowing unreacted material to remain at the cold edges of the sample. However, new peaks corresponding to expected reaction products also appear in the second diffraction image, indicating that a reaction occurred even if it did not reach completion. Peaks corresponding to cubic $Pm\bar{3}m$ $CaSiO_3$ (davemaoite) (Stixrude et al., 2007) and orthorhombic Pnma Fe_3C (Li et al., 2002) are present as expected. Additionally, peaks corresponding to B1 FeO (Fischer et al., 2011), B1 CaO (Richet et al., 1988), SiO_2 (stishovite) (Chao et al., 1962), and orthorhombic Fe_7C_3 (Prescher et al., 2015) appear. FeO, CaO, SiO_2, and Fe_7C_3 are intermediate phases that occur along the reaction pathway for equation 2.1, and appear in the diffraction pattern due to the incompleteness of the reaction. Based on these observations, a plausible reaction pathway is as follows:

$$15CaCO_3 + 13\,Fe_3Si \rightarrow 5Fe_7C_3 + 13CaSiO_3 + 4FeO + 2CaO \quad (2.2)$$

$$5Fe_7C_3 + 4FeO + 2Fe_3Si \rightarrow 15Fe_3C + 2SiO_2 \quad (2.3)$$

$$2SiO_2 + 2\,CaO \rightarrow 2\,CaSiO_3 \quad (2.4)$$

Equations 2.2 through 2.4 add up to equal 15 of equation 2.1, and show a complete pathway for the carbon-silicon exchange reaction. First, unequal molar amounts of $CaCO_3$ and Fe_3Si react to form Fe_7C_3, $CaSiO_3$, FeO, and CaO. Fe_7C_3, FeO, and Fe_3Si then react to make Fe_3C and SiO_2, and SiO_2 reacts with CaO to make $CaSiO_3$. Because the X-rays probe the entire sample across the large axial temperature gradient, the diffraction pattern captures phases at all three stages of the reaction: 1) unreacted starting material (Fe_3Si and $CaCO_3$); 2) intermediate phases that form during the

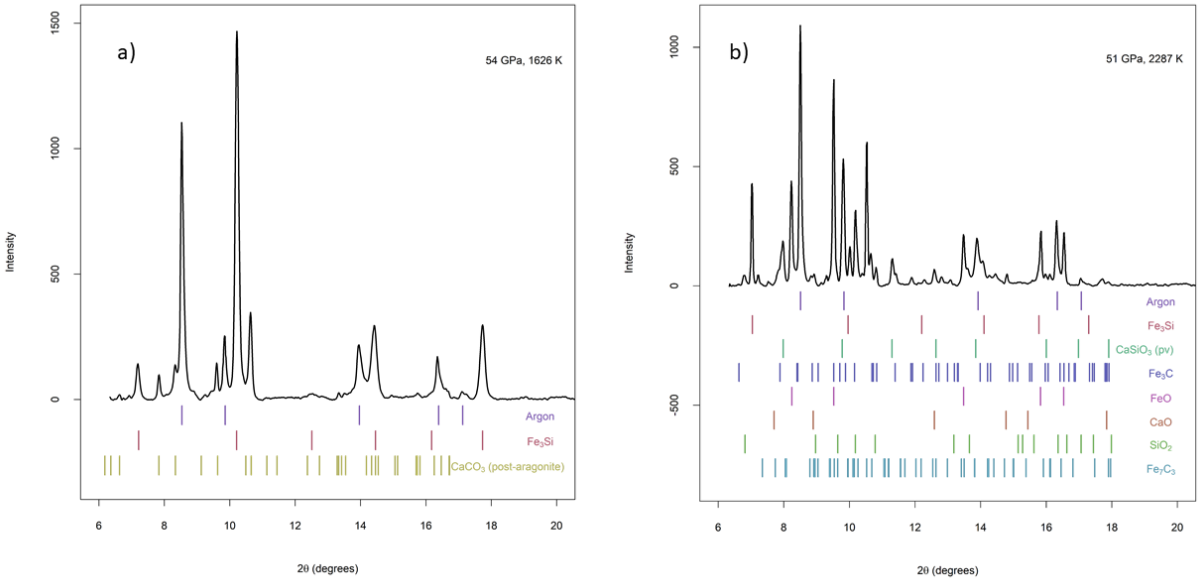

Figure 2.1: X-ray diffraction patterns for the reaction $CaCO_3$ + Fe_3Si at a) 54 GPa and 1626 K (before reaction) and b) 51 GPa and 2287 K (after reaction). Before reaction, only the starting materials, Fe_3Si (B2) and $CaCO_3$ (post-aragonite), and the pressure medium, Ar, are identified. After reaction, the new phases $CaSiO_3$ (davemaoite) and Fe_3C are present in addition to the intermediate phases FeO, CaO, SiO_2 (stv), and Fe_7C_3, and to Ar and unreacted Fe_3Si.

reaction (CaO, Fe_7C_3, SiO_2, and FeO); and 3) completed exchange reaction products (Fe_3C and $CaSiO_3$). The experimental conditions and reaction products upon quench for all samples of the $CaCO_3$ reaction are highlighted in orange in Table 2.1. $CaCO_3$ adopts the $CaCO_3$-VII structure (Gavryushkin et al., 2017) below 38 GPa, the post-aragonite structure from 38-79 GPa, and the tetrahedrally coordinated $P2_1/c$ phase (Boulard et al., 2011) above 79 GPa.

The $MgCO_3$ reaction behaves similarly to the $CaCO_3$ reaction. Figure 2.2 displays example X-ray diffraction patterns at 33 GPa before reaction (Figure 2.2a) and after reaction (Figure 2.2b). In Figure 2.2a, peaks corresponding to Fe_3Si and $MgCO_3$ (Ross, 1997) are identified. In the diffraction pattern after reaction, peaks corresponding to unreacted starting material are joined by new peaks corresponding to end products $MgSiO_3$ (bridgmanite) and

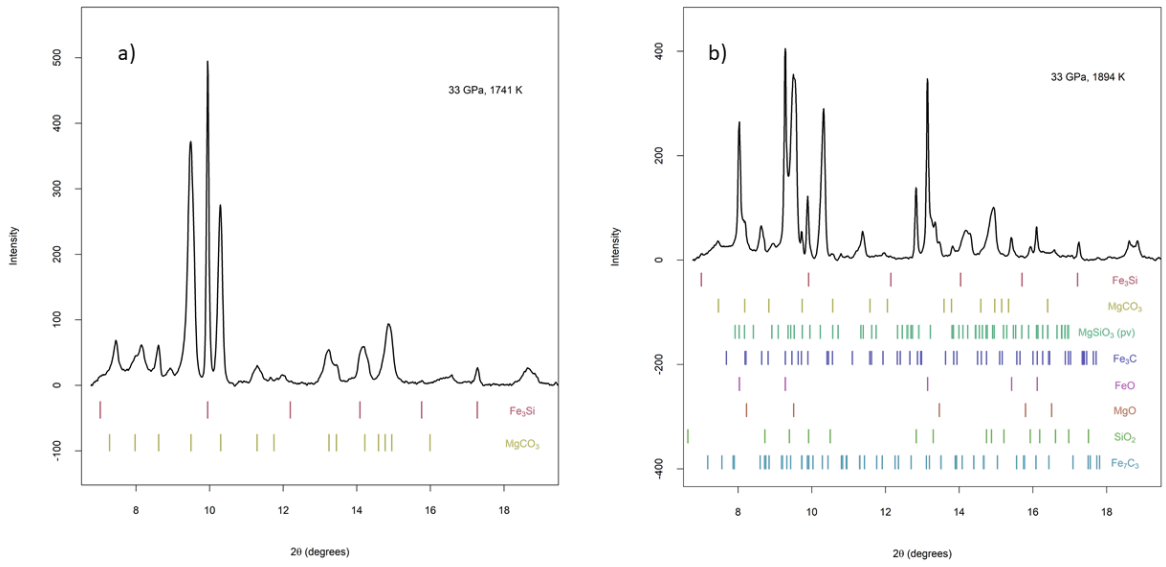

Figure 2.2: X-ray diffraction patterns for the reaction $MgCO_3$ + Fe_3Si at a) 33 GPa and 1741 K (before reaction) and b) 33 GPa and 1894 K (after reaction). Before reaction, only the starting materials, Fe_3Si (B2) and $MgCO_3$ are identified. After reaction, the new phases $MgSiO_3$ (bridgmanite) and Fe_3C, are present in addition to the intermediate phases FeO, MgO, SiO_2 (stv), and Fe_7C_3 and to unreacted starting material.

Fe_3C, and intermediate products FeO, MgO, SiO_2, and Fe_7C_3. Similar to in the $CaCO_3$ reaction, FeO, MgO, and Fe_7C_3 are formed from equations 2.2 to 2.4, where Ca is replaced by Mg. The experimental conditions and quench products for the $MgCO_3$ reaction are identified in blue in Table 2.1.

2.3.2 EDS Results

Our X-ray diffraction data is supported through EDS analysis of recovered samples. A sample of the $CaCO_3$ reaction recovered from 40 GPa and quenched from 1613 K is shown in Figure 2.3 and Figure 2.4 (see also Figure A.1). Figure 2.3a is the back-scattered electron image,

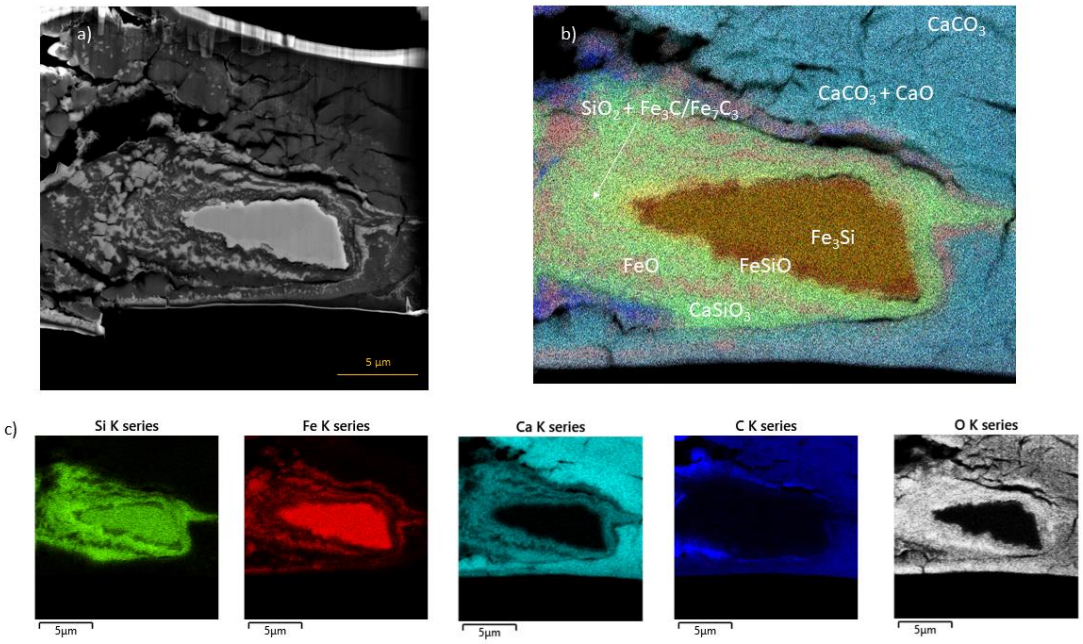

Figure 2.3: SEM image of $CaCO_3$ + Fe_3Si reaction, quenched from 1613 K at 40 GPa. a) BSE image of the recovered sample mounted on a TEM grid. b) EDS map of the recovered sample, with identified compounds labelled. Unreacted Fe_3Si is surrounded by a fine-grained quench matrix, containing $CaSiO_3$, FeO, Fe_3C, Fe_7C_3, and SiO_2. Surrounding the quench matrix is a halo containing $CaCO_3$ and CaO. The reacted material is surrounded by unreacted $CaCO_3$. c) EDS maps of individual elements.

and Figure 2.3b,c and Figure 2.4 are EDS maps and point analyses, respectively. The EDS maps are QuantMaps, where a full EDS analysis is done on each pixel and the weight percent of each element is mapped. Because the sample was carbon-coated and due to the difficulty of measuring carbon through EDS analysis, we only take carbon measurements for the point analyses in the carbon-rich regions identified from the carbon EDS map. In carbon-poor regions, carbon measurements are excluded to get more accurate compositions.

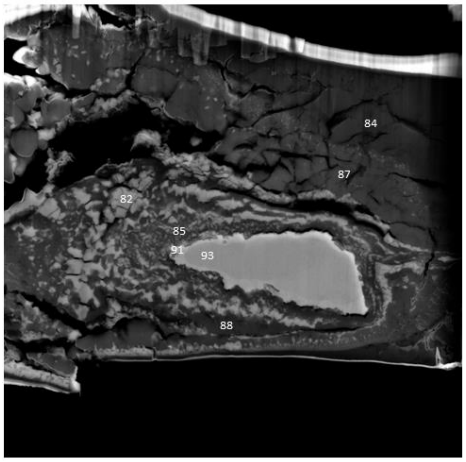

Point	O (%)	Si (%)	Ca (%)	Fe (%)	C (%)	Phases
82	50.22	2.64	2.66	44.49	0	$FeO + CaSiO_3$
84	52.23	0.31	24.94	0	22.52	$CaCO_3$
85	48.97	17.94	4.00	21.45	7.64	SiO_2 + Fe_3C/Fe_7C_3
87	52.19	0.25	27.42	1.40	18.73	$CaCO_3 + CaO$
88	61.64	16.64	18.91	2.80	0	$CaSiO_3$
91	17.58	16.15	0.7	65.57	0	$Fe_3(Si,O)$
93	0	26.26	0	73.74	0	Fe_3Si

Figure 2.4: Compositions obtained from EDS point analysis. All elemental abundances are listed in atomic percent.

From the EDS analyses, we see a multitude of different phases across the sample cross section, highlighting the axial temperature gradient in our samples. The cold edges of the sample contain unreacted $CaCO_3$ starting material. Moving closer to the center of the sample, we identify a halo of $CaCO_3$ that is enriched in calcium and iron. We interpret this region as CaO + $CaCO_3$, and it represents the reaction front. Additionally, this region is depleted in carbon. Carbon is a highly mobile element, as evidenced by the measured fast diffusion of CO_2 through carbonates (Liu et al., 2021) and the high calculated diffusivities of carbon in silicate melt (see

Chapter 4 and Solomatova et al. 2019). We conclude that carbon diffuses quickly through the carbonate to react with Fe_3Si at the edge of the reaction front. We identify the central metal blob as unreacted Fe_3Si, which remains in the sample because the reaction did not go to completion. The edges of the metal blob are enriched in Fe and O, and depleted in Si (Figure 2.5b), indicating that Si diffuses more quickly out of the Fe_3Si material to react with $CaCO_3$. The material surrounding the metal blob forms bands of FeO and $CaSiO_3$. The material immediately to the left of the metal blob was directly in the path of the laser, and is very fine-grained compared to other regions of the sample due to the higher temperature. Due to the small size of the grains and the resolution limits of the SEM, there is some overlap in the measurement of individual grains. However, from the point analyses, we deduce that the quench matrix consists of a mixture of

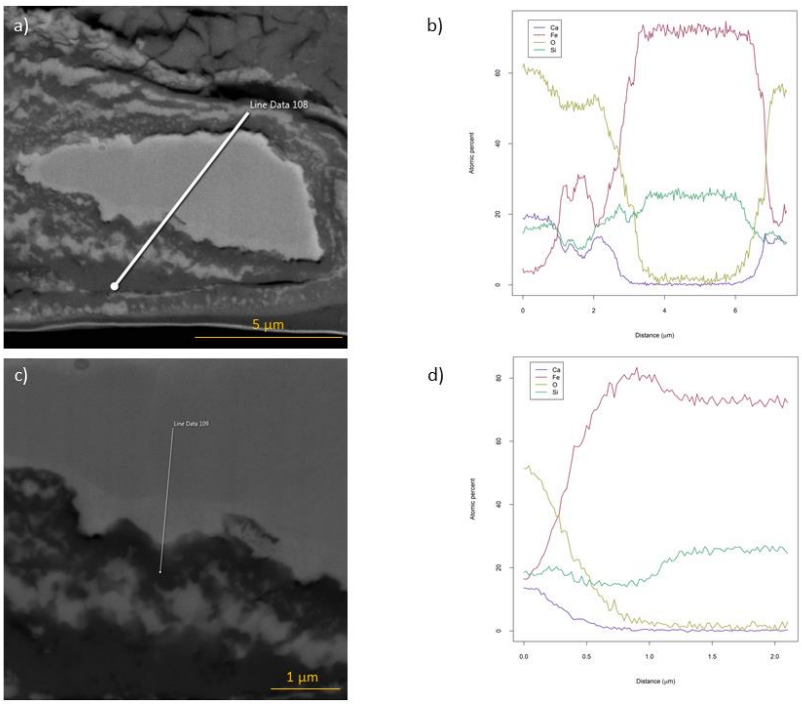

Figure 2.5: EDS line scans across a)-b) the center of the sample and c)-d) the edge of the metal blob. The metal blob is unreacted Fe_3Si, but the edge of the metal blob is depleted in silicon.

$CaSiO_3$, FeO, SiO_2, Fe_3C, and Fe_7C_3. Additionally, there are regions of the sample that appear to have unusually high carbon contents, as indicated by the carbon EDS map (Figure 2.3c). These regions tend to occur around cracks in the sample. We therefore attribute the high carbon content around the cracks to deposition of carbon resulting from the platinum deposition process or from ubiquitous carbon contamination. Combined with the X-ray diffraction results, the EDS results confirm the carbon, silicon redox exchange reaction (equation 2.1) as well as the intermediary steps of the reaction (equations 2.2-2.4).

2.3.3 Phase diagrams

Based on the identification of phases in the X-ray diffraction patterns, we construct phase diagrams for this particular mantle phase assemblage (Figure 2.6 and Figure 2.7). In each diffraction experiment, we identify the pressure and temperature conditions under which the carbonate and Fe_3Si are stable, and the pressure and temperature conditions under which iron carbide and perovskite phase are stable. The perovskite phase always appears among the first new phases formed during the reaction, and is the most obvious phase to identify in the diffraction pattern. Thus, it is a useful indicator of the exchange reaction. We use the first appearance of perovskite in the diffraction pattern to set a reaction temperature above which the carbonate phase is no longer stable. The temperature measured during the diffraction experiments is the temperature at the optically opaque surface. At the moment of reaction, the optically opaque surface is the unreacted Fe_3Si starting material, and the temperature measured corresponds to the temperature at the center of the sample where the unreacted Fe_3Si sits (Figure 2.3). This depth within the sample is also the depth at which we observe the exchange reaction taking place in the SEM image, indicating that the measured temperature corresponds to the

temperature of the reaction. In Figure 2.6, points above the reaction temperature are plotted with filled green circles, while points below the reaction temperature are plotted with open purple circles (see also Tables A.1-A.2). Experiments measured in argon have minimal thermal

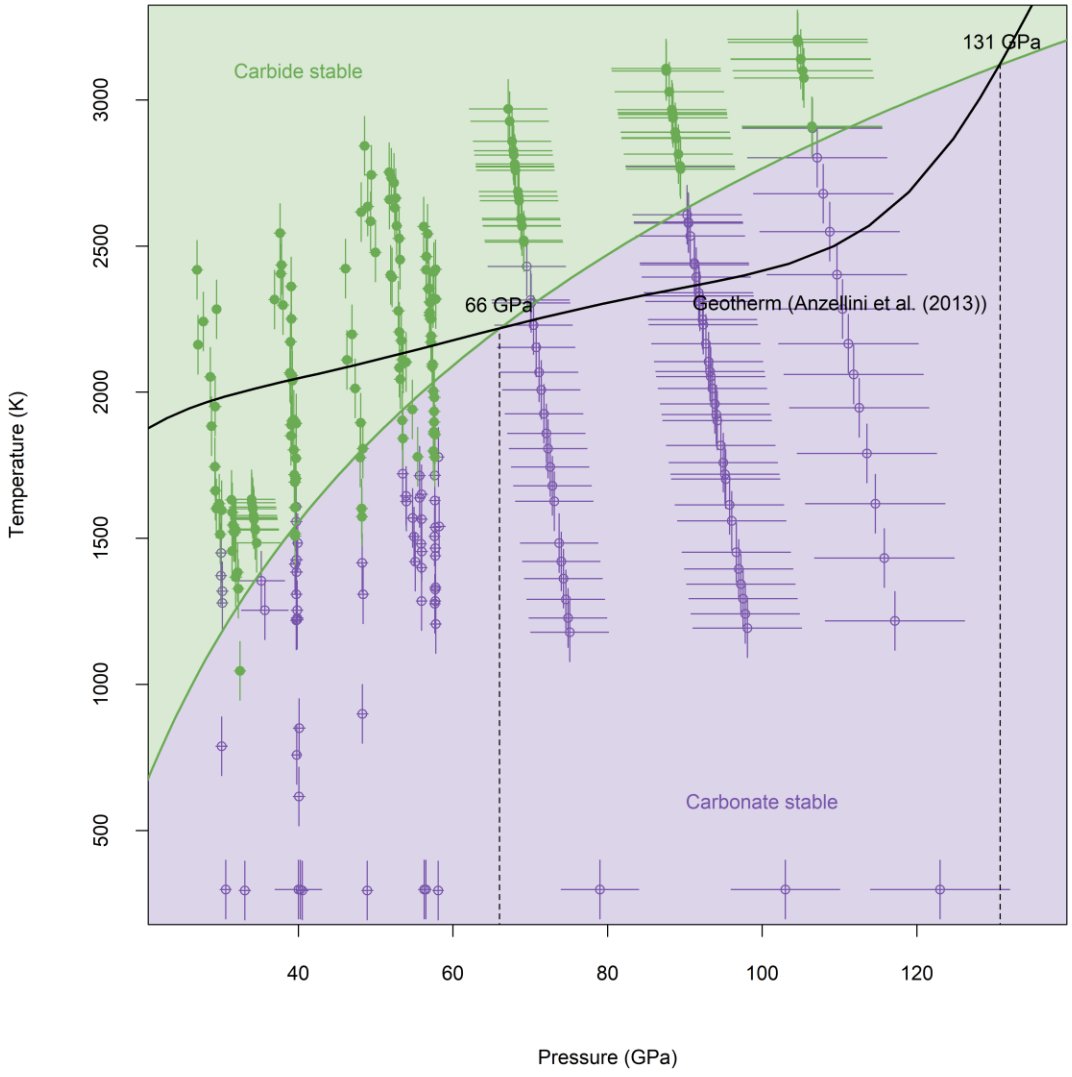

Figure 2.6: Phase diagram illustrating the conditions under which the $CaCO_3$ reaction products, $CaSiO_3$ and Fe_3C, are stable (green) and the conditions under which the $CaCO_3$ reactants, $CaCO_3$ and Fe_3Si, are stable (purple). The green curve is the fit to the reaction temperature and is compared to the Anzellini et al. (2013) geotherm.

expansion, except at high temperature when the argon pressure medium begins to melt (Datchi et al., 2000). We fit the reaction temperatures to a logarithmic function (green line), which allows us to map out the regions where carbonate is the stable carbon-bearing phase (purple), and where carbide is the solid carbon-bearing phase (green). The temperature at which the reaction occurs increases with pressure, indicating that in this particular phase assemblage, the carbonate phase is stabilized to higher temperatures with increasing depth in the mantle. Comparing our reaction line to an example mantle geotherm (Anzellini et al., 2013), we find the lines cross initially at 66 GPa and again at 131 GPa. Below 66 GPa, the mantle temperature is hotter than the reaction temperature, leading to the formation of carbide phases. Between 66 and 131 GPa, the mantle temperature is colder than the reaction temperature, and we would expect carbonate to be the stable carbon-bearing phase for much of the lower mantle. From 131 GPa to the core-mantle boundary, the mantle temperature is again hotter than the reaction temperature, and we anticipate the formation of carbide phases.

The data for the $MgCO_3$ reaction is plotted in Figure 2.7, and is similar to the $CaCO_3$ reaction data. We identify the reaction temperature by the appearance of bridgmanite in the diffraction pattern. Points above the reaction temperature are plotted with filled blue circles, and points below the reaction temperature are plotted with open red circles. We fit the reaction temperatures to a logarithmic function (blue line), and have shaded the regions where carbide is stable in blue and the regions where carbonate is stable in red. The temperature at which the reaction occurs increases with pressure, indicating that the $MgCO_3$ phase is stabilized to increasingly high temperatures with depth in the mantle. Comparing this reaction line to the Anzellini et al. (2013) geotherm, we find two crossover points at 33 and 130 GPa. In this system,

below 30 GPa and above 130 GPa, the stable carbon-bearing phase is iron carbide and between 30 and 130 GPa, the stable carbon-bearing phase is $MgCO_3$. Additionally, we compare the $MgCO_3$ reaction directly to the $CaCO_3$ reaction (the green line). The $MgCO_3$ line first crosses the

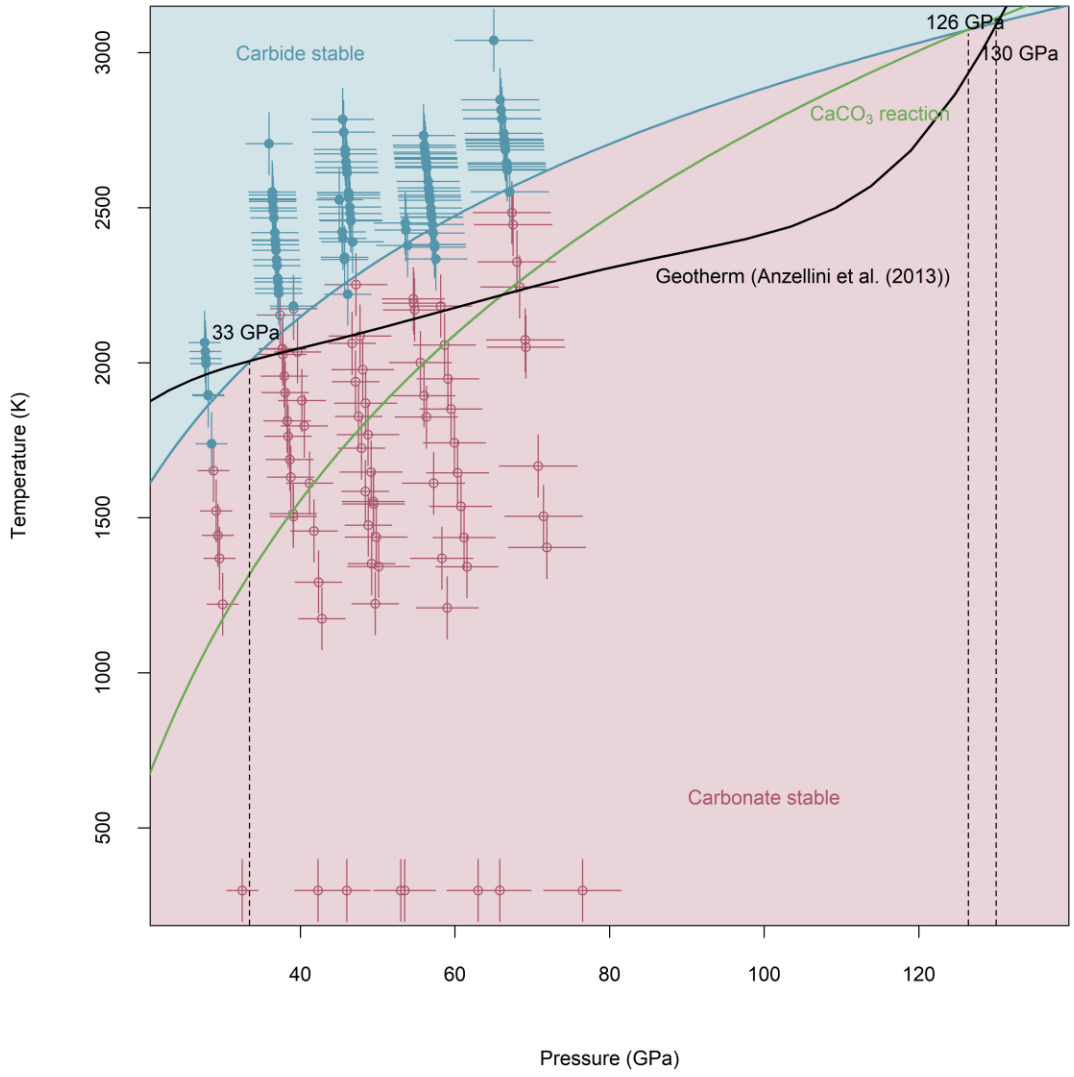

Figure 2.7: Phase diagram illustrating the conditions under which the $MgCO_3$ reaction products, $MgSiO_3$ and Fe_3C, are stable (blue) and the conditions under which the $MgCO_3$ reactants, $MgCO_3$ and Fe_3Si, are stable (red). The blue curve is the fit to the reaction temperature and is compared to the Anzellini et al. (2013) geotherm and the $CaCO_3$ reaction (green line).

geotherm around 30 GPa lower than the first crossing for the $CaCO_3$ reaction, indicating that $MgCO_3$ is stabilized at a shallower depth than $CaCO_3$. Additionally, the $MgCO_3$ line lies above the $CaCO_3$ line until the two lines cross at 126 GPa. Thus, below 126 GPa, we expect $MgCO_3$ to be stabilized relative to $CaCO_3$, but above 126 GPa, we expect $CaCO_3$ to replace $MgCO_3$ as the stable carbonate phase. Since our $MgCO_3$ reaction data must be extrapolated above ~80 GPa, the exact pressure at which this crossover occurs is ambiguous. However, the crossover of the two lines is suggestive of switching stability regimes between the two carbonates, and is in agreement with recent work (Dorfman et al., 2018; Lv et al., 2021).

2.4 Discussion

The crossover of the carbonate reaction line with the mantle geotherm indicates that in this particular phase assemblage, carbonate is the stable carbon-bearing phase for much of the lower mantle. The stability of the carbonate phase under these conditions is anomalous. Previous studies of carbonates at the pressure and temperature conditions of the lower mantle indicate that carbonates primarily melt (Dasgupta and Hirschmann, 2010; Xu et al., 2020), decarbonate (Drewitt et al., 2019; Li et al., 2018), or are reduced to diamond or carbide via redox freezing (Arima et al., 2002; Rohrbach and Schmidt, 2011). However, many processes dictate the stability of carbonates, including reactions with surrounding phases. In this particular phase assemblage, the carbonate phase is favored over more reduced forms of carbon at most lower mantle conditions. If such a phase assemblage exists in subducting slabs, this process could be an important mechanism for transportation of carbon into the Earth's deep interior.

Other lower mantle petrologic studies of carbonates have seen both similar and different results. In both Dorfman et al. (2018) and Zhu et al. (2019), carbonate reacted with iron to make iron carbides and diamond. Similarly, in Chapters 4 and 5 of this thesis, we use *ab initio* molecular dynamics calculations to show that carbonate, silicate, and metal melt interact to form carbon and iron clusters indicative of dense Fe-C liquids and diamond nucleation. However, in this work, we see no evidence for diamond formation in either the X-ray diffraction data or the EDS measurements. In Lv et al. (2021), carbonate and silicate undergo a cation exchange reaction and there is no evidence of carbon reduction in any form. Taking these five studies together, we conclude that carbonate is only reduced in the presence of metal. Additionally, it appears that carbonates only reduce to diamond under moderately reducing conditions. In this study, carbonates react with an iron-silicon alloy, which is more reducing than pure iron metal. The reaction of carbonates with a stronger reducing agent drives the system towards iron carbide formation rather than diamond formation. Thus, the behavior of carbon is greatly influenced by the presence of other species and based on the surrounding phase assemblage and redox conditions of the mantle, we might expect a variety of carbon-bearing phases to be stable.

Both Dorfman et al. (2018) and Lv et al. (2021) find that $CaCO_3$ is the stable carbonate phase in the lowermost mantle over $MgCO_3$. Dorfman et al. (2018) reacted dolomite with iron metal at pressures between 51-113 GPa and temperatures between 1800-2500 K, and discovered that only the $MgCO_3$ component reacted with iron while the $CaCO_3$ component remained stable. Lv et al. (2021) reacted carbonate and silicate together, and found that $MgCO_3$ reacted with silicates to form $CaCO_3$ at pressures between 70-95 GPa, depending on the temperature. In this study, we find that $MgCO_3$ is the stable carbonate for the majority of the lower mantle, but we

also identify a phase boundary where $CaCO_3$ becomes more stable than $MgCO_3$ at ~126 GPa. The exact pressure at which this crossover take place is ambiguous, due to the extrapolation of the $MgCO_3$ reaction line beyond 80 GPa in our dataset. However, the fact that we identify a phase boundary in the lower mantle lends credence to the notion that $CaCO_3$ replaces $MgCO_3$ as the stable carbonate in the lowermost mantle. The transition from $MgCO_3$ to $CaCO_3$ has been previously attributed to polymorphic phase transitions associated with sp^2-sp^3 bonding changes in $CaCO_3$ (Lv et al., 2021), which have been observed experimentally at ~105 GPa and 2000 K (Lobanov et al., 2017) and computationally between ~70 (Zhang et al., 2018) and ~100 GPa (Santos et al., 2020) at lower mantle temperatures. Our predicted transition is at a slightly higher pressure than these reported transitions.

The slope of the carbonate reaction line indicates that carbon becomes less siderophile with increasing pressure with respect to silicon. Previous low pressure and temperature measurements (less than 20 GPa and 2600 K) of the carbon partition coefficient $D_C^{metal/silicate}$ (Armstrong et al., 2015; Chi et al., 2014; Dasgupta et al., 2013; Li et al., 2015) suggest partition coefficients on the order of 10^2-10^3 between metal and silicate melts. Partition coefficients of this magnitude indicate that carbon is highly siderophile and imply that the majority of Earth's carbon was sequestered into the core upon formation. However, measurements conducted at higher pressures and temperatures corresponding to a deep magma ocean (up to 59 GPa and 5200 K) report D_C values on the order of 1-100 (Fischer et al., 2020), implying that less carbon may have been sequestered into the core upon formation than previously thought. The decrease in D_C values by several orders of magnitude with increasing pressure supports the trend observed in this study, and implies that more carbon may be present in the lower mantle and at the core-

mantle boundary than previously imagined. Additionally, D_C values are dependent on bulk carbon content, and have been shown to increase with increasing carbon concentration (Grewal et al., 2021). In the work of Grewal et al. (2021), the authors report that previous measurements may have overestimated the amount of carbon in the core due to high D_C values from oversaturation of carbon in the measured systems, further increasing the notion that more carbon is present in the lower mantle than previously thought.

Figure 2.8 summarizes some different pathways that carbonates undergo in the mantle. Previous pathways that have been studied are denoted with arrows on the right side of the figure

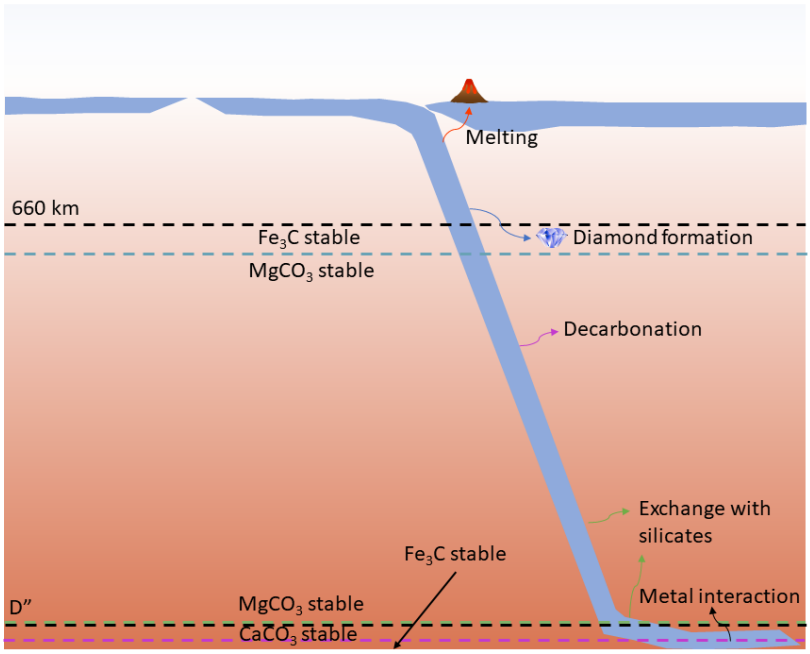

Figure 2.8: Schematic of possible carbonate fates in a subducting slab in the mantle. The dotted blue line denotes the depth at which the stable carbon-bearing phase switches from Fe_3C to $MgCO_3$ in our example phase assemblage, while the green line denotes the depth at which $CaCO_3$ becomes more stable than $MgCO_3$. The purple line denotes the depth at which the stable carbon-bearing phase switches from $CaCO_3$ back to Fe_3C. The arrows indicate other processes that carbonates undergo, including melting, redox freezing to form diamond, decarbonation, exchange with silicates, and interactions with metals.

and include melting to form carbonatitic compositions, diamond formation through redox freezing, decarbonation with free silica, exchange with lower mantle silicates, and interactions with free metal in the mantle or from the core. On the left side of the figure, we denote the regions where Fe_3C, $MgCO_3$, and $CaCO_3$ are stable based on the reactions studied in this work. $MgCO_3$ is the stable carbon-bearing phase for the majority of the lower mantle, indicating that carbonates are stable in the lower mantle at much greater depth than previously assumed. $CaCO_3$ becomes the stable carbon-bearing phase just before the D" transition, before Fe_3C becomes the stable carbon-bearing phase just before above the core-mantle boundary.

The stability of the carbonate phases in these exchange reactions indicate the importance of petrologic context in understanding the behavior of carbon-bearing systems. This work and other recent studies (Dorfman et al., 2018; Lv et al., 2021; Zhu et al., 2019) represent progress in multiphase mantle petrology in the lower mantle, but more studies are necessary to elucidate the stability and reactivity of carbonates in the lower mantle and to fully understand the deep Earth carbon cycle.

2.5 Conclusions

Carbonates in the lower mantle participate in reactions with Fe_3Si to make perovskite phases and iron carbides. However, the temperature at which these reactions occur increases with pressure, indicating that the stability field of carbonates also increases with pressure. Additionally, the increased stability of the carbonate phase with depth implies that carbon becomes less siderophile with increasing pressure with respect to silicon. Comparing the exchange reaction temperature to a mantle geotherm, we find an initial crossover point where

carbonates become the stable carbon-bearing phase in the mantle over iron carbide. The crossover point occurs at 33 GPa in the $MgCO_3$ reaction and 66 GPa in the $CaCO_3$ reaction and the carbonate phases remain the stable carbon-bearing phases in the mantle until a second crossover point is reached at ~130 GPa for both reactions. $MgCO_3$ is stabilized to higher temperatures than $CaCO_3$, indicating that it is the more stable carbonate phase. However, we find a crossover point in the $CaCO_3$ and $MgCO_3$ reaction lines at 126 GPa, indicating that $CaCO_3$ replaces $MgCO_3$ as the stable carbonate phase in the lowermost mantle just above the D" transition. In this mantle phase assemblage, the carbonate phase is stabilized throughout much of the lowermost mantle. Thus, in similar phase assemblages in subducting slabs, carbonates could survive into the lower mantle where they could participate in reactions with other lower mantle phases.

CHAPTER 3

AB INITIO MOLECULAR DYNAMICS: THEORY

3.1 Introduction

In this chapter, I describe the methodology behind *ab initio* molecular dynamics calculations, which are used in chapters 4 and 5. For more background reading, the text *Ab initio* molecular dynamics: basic theory and advanced methods (Marx and Hutter, 2009) is recommended. *Ab initio* molecular dynamics simulations utilize density functional theory calculations, and serve as useful tools to calculate systems and properties that would be difficult to measure experimentally. Although no system can be solved exactly with density functional theory methods, there are numerous examples where computational results have matched experimental results, validating the use of density functional theory and *ab initio* molecular dynamics methods as a predictive tool for calculating system properties. For instance, these computational methods have corrected predicted the structure of the post-aragonite phase of $CaCO_3$ (Oganov et al., 2006), matched the experimentally measured density of $CaCO_3$ melts (Genge et al., 1995), and correctly predicted the spin transition of iron in iron-bearing $MgSiO_3$ melts (Ghosh and Karki, 2020).

Both classical and quantum mechanical methods have been used to simulate systems on an atomic level. Classical methods require empirically derived potentials to describe interatomic forces. These potentials are system-dependent and sometimes fail to describe high pressure systems. External potentials also require a lot of experimental data. Quantum mechanical methods, however, are *ab initio*. They simulate electronic structure without using empirical

potentials or experimental input, and thus, are better suited to describe atomic systems at extreme pressures.

The Schrödinger equation is the quantum mechanical equivalent of Newton's equation of motion. It is a partial differential equation that describes how a wavefunction of a particle evolves under an external potential over time. The Schrödinger equation for an electron takes the form:

$$i\hbar\frac{\delta\Psi}{\delta t} = -\frac{\hbar^2}{2m_e}\frac{\delta^2\Psi}{\delta x^2} + V\Psi \tag{3.1}$$

where ħ is Planck's constant, m_e is the electron mass, V is the time independent potential, and Ψ is the wavefunction, which is a function of space and time. The equation can be solved through separation of variables, which results in two ordinary differential equations, one a function of time, the other a function of position. To obtain electronic structure, the time-independent Schrödinger equation must be solved:

$$-\frac{\hbar^2}{2m_e}\frac{d^2\psi}{dx^2} + V\psi = E\psi \tag{3.2}$$

where ψ is the time-independent wavefunction. The time-independent Schrödinger equation can only be solved for the hydrogen atom. For an N-body system, where more than one electron is present, the Schrödinger equation cannot be solved exactly, and approximate methods must be used.

The Born-Oppenheimer is one such approximation that allows the wavefunction to be separated into an electronic and a nuclear component:

$$\Psi_{total} = \Psi_{electronic}\, x\, \Psi_{nuclear} \tag{3.3}$$

Since the nuclei are much larger than the electrons, they move more slowly. Thus, we can assume that at any moment, the electrons are in their ground state with respect to an instantaneous nuclear configuration, allowing for just the electronic part of the wavefunction to be solved. However, even with the Born-Oppenheimer approximation, the N-body Schrödinger equation is still too complicated to solve.

3.2 Density Functional Theory (DFT)

To simplify the N-body problem, Hohenberg and Kohn devised two theorems in 1964. In the first, they identify that there is a direct link between the electronic density of a system and its wavefunction. This means that there is no information loss in rewriting the wavefunction as an electronic density. Thus, the electron density uniquely determines the external potential and the ground state properties of the N-body system. The total energy can then be written as:

$$E[n(r)] = \int V_{ext}(r)n(r)dr + F_{HK}[n(r)] \tag{3.4}$$

where n(r) is the scalar electron density, $V_{ext}(r)$ is the external potential, and $F_{HK}[n(r)]$ is the Hohenberg-Kohn functional, which does not depend on the external potential. $F_{HK}[n(r)]$ contains T[n(r)], the kinetic energy function of the interacting electrons, and J[n(r)], the Coulomb potential functional for the interacting system. In the second theorem, they demonstrate that the ground state density and the electron density corresponding to the lowest total energy are the same. Thus, if $F_{HK}[n(r)]$ is calculated, the ground state density for a given $V_{ext}(r)$ can also be determined through minimizing the energy. The Hohenberg-Kohn theorems simplify the N-body problem to a 3-dimensional scalar field, but because $F_{HK}[n(r)]$ is unknown, it is still impossible to solve the Schrödinger equation.

In 1965, Kohn and Sham rewrote $F_{HK}[n(r)]$ as:

$$F_{HK}[n(r)] = T_0[n(r)] + V_H[n(r)] + V_{XC}[n(r)] \quad (3.5)$$

where $T_0[n(r)]$ represents the kinetic energy functional for non-interacting electrons, $V_H[n(r)]$ is the classical Hartree potential (which is the electrostatic potential from the electron charge density), and $V_{XC}[n(r)]$ is the exchange-correlation potential. With this formalism, the easily computable terms are extracted, allowing the energy functional for the non-interacting system to be written as:

$$E[n(r)] = T_0[n(r)] + V_H[n(r)] + V_{XC}[n(r)] + V_{ext}[n(r)] \quad (3.6)$$

The Hamiltonian for this system is:

$$\left[-\frac{\hbar^2}{2m_e}\nabla^2 + V_{KS}(r)\right]\psi_i(r) = \varepsilon_i\psi_i(r) \quad (3.7)$$

where m_e is the mass of an electron, ψ_i are the one electron Kohn-Sham orbitals where i varies from 1 to N/2, and $V_{KS}(r)$ is a potential with a ground state electron density of n(r). This Hamiltonian results in the same ground state electron density as the original system. Now the only unknown term is $V_{XC}[n(r)]$, which is approximated in many ways.

The two most common approximations are the local density approximation (LDA) (Kohn and Sham, 1965; Perdew, 1979) and the generalized gradient approximation (GGA) (Perdew, 1986; Perdew et al., 1996). With LDA, the exchange correlation is:

$$V_{XC}^{LDA}[n(r)] = \int n(r)\varepsilon_{XC}[n(r)]dr \quad (3.8)$$

and is approximated as a function of the local density of a homogenous electron gas, which is determined through Monte-Carlo simulations. LDA assumes that the density distribution is uniform over all space, but GGA includes the local gradient in the density. With GGA, the exchange correlation is:

$$V_{XC}^{GGA}[n(r)] = \int n(r)\varepsilon_{XC}[n(r), |\nabla n(r)|]dr \quad (3.9)$$

A more accurate form of GGA known as Perdew-Burke-Ernzerhof (PBE) (Perdew et al., 1996) was proposed in 1996. It is a simpler and more efficient GGA, where all parameters have been replaced with fundamental constants. It falls under the GGA umbrella of approximations. Since LDA and GGA are approximations, they cannot exactly solve the Schrödinger equation. In fact, LDA generally underestimates and GGA generally overestimates the cohesive energy, leading to underestimations and overestimations of volume, respectively.

Equipped with these approximations, we can solve the Kohn-Sham equations. The Kohn-Sham Hamiltonian depends on the electron density, n(r), which depends on the $\psi_i(r)$ being calculated. However, we do not know $\psi_i(r)$ until the Kohn-Sham equations are solved. Because of this, an iterative procedure is required. We start with an initial guess of n(r) to calculate $\psi_i(r)$, use the calculated $\psi_i(r)$ to get a new n(r), and repeat until n(r) achieves convergence. The Kohn-Sham equations are necessary formalisms to solve the N-body problem, and thus, serve as the basis upon which all density functional theory calculations are built.

3.3 Plane Waves

In crystallography, crystal lattices are often represented in reciprocal or *k*-space by applying a Fourier transform to a real space lattice. In reciprocal space, the primitive cell is known as the first Brillouin zone. The Brillouin zone is sampled computationally with a uniform mesh of *k*-points, and the wavefunction can be characterized in the first Brillouin zone using periodic conditions. With periodic boundary conditions, an infinite system can be approximated with a finite number of atoms by assuming that the atoms in each unit cell move identically to the atoms in all other unit cells. Blöchl's theorem states that the wavefunction of an electron within a periodic potential can be written as the product of a wave-like term and a term with the

periodicity of the unit cell. Thus, the electronic wavefunction at each *k*-point can be expanded in terms of a plane wave basis set. The plane wave basis set is truncated to include plane waves with kinetic energies smaller than some cutoff. In these calculations, I choose a cutoff energy determined through convergence of the energy to a desired accuracy. Larger cutoff energies are more accurate.

Core electrons are often treated with a different basis set than valence electrons using augmented planewaves (APW), pseudopotentials (PP), or projector-augmented waves (PAW). This is because valence wavefunctions oscillate rapidly near the atomic nucleus, and inaccurate descriptions of these rapid oscillations result in an improper description of the valence orbitals. APW (Slater, 1937) defines a sphere around the atom that is the approximate size of the covalent radius. The radial Schrödinger equation is solved within the sphere for the spherically-averaged effective potential. In the interstitial regions between spheres, plane waves are solved. The linear augmented plane wave method (LAPW) (Andersen, 1975; Soler and Williams, 1989) makes the basis functions and the derivatives continuous. LAPW explicitly includes core electrons in its calculations. To avoid this, the core potential can be replaced with a smoothly varying pseudopotential and simple pseudo-wavefunctions (Antončík, 1959; Phillips and Kleinman, 1959). With the pseudopotential method, the orthogonality condition in the orthogonalized plane-wave method (Herring, 1940) is replaced with an effective potential. Pseudopotentials are commonly norm-conserving (Hamann et al., 1979) or ultrasoft (Vanderbilt, 1990). With norm-conserving pseudopotentials, the norm of the pseudo-wavefunctions within the core radius is constrained to be the same as the true wavefunctions. With ultrasoft pseudopotentials, the norm-conserving constraint is relaxed, creating softer pseudopotentials, where the softness refers to the

ability to use as few planewaves as possible in the expansion of the valence pseudo-wavefunctions. To correct for the non-conservation of norms, localized atom-centered augmentation charges must be introduced. The PAW method (Blochl, 1994) is a combination of the APW and PP methods, where a linear transformation connects the true wavefunctions with soft pseudo-wavefunctions.

3.4 Molecular Dynamics

In molecular dynamics (MD), atoms are moved by interatomic forces and obey Newtonian mechanics. In classical MD, electronic interactions are replaced by simplified interatomic potentials, which need to be known ahead of time. In *ab initio* MD, the interatomic forces are fully computed in a first principles framework. In this thesis, I use Born-Oppenheimer MD (Payne et al., 1986; Payne et al., 1992), which allows for the contributions of the nuclei and the electrons to the wavefunction to be decoupled.

In each timestep in the calculation, the electronic contribution to the wavefunction is determined in a static system by solving the time-independent Schrödinger equation. For this to work, we assume that the electrons adjust instantaneously to their equilibrium positions after the movement of the nuclei. The movement of the nuclei occurs concurrently and is solved using classical mechanics (i.e. a Verlet algorithm (Verlet, 1967)). The equations describing Born-Oppenheimer molecular dynamics are:

$$MR(t) = -\nabla_i \Psi_0 \{\langle \Psi_0 | H_e^{KS} | \Psi_0 \rangle\} \tag{3.10}$$

$$E_0 \Psi_0 = H_0 \Psi_0 \tag{3.11}$$

where M is the mass of the nucleus, R is its position, t is the time, and H_e^{KS} is the Hamiltonian describing the Kohn-Sham electronic contribution.

Ab initio molecular dynamics proceed in the following way: 1) Set up an initial configuration; 2) Perform a DFT calculation and get the electronic ground state; 3) Calculate the atomic forces; 4) Propagate the nuclei; 5) Repeat steps 2-4 until convergence is reached. Convergence is achieved when the system has an energy equal to a cutoff energy imposed upon the system. After convergence, 1 time step has been completed. Simulations are run for the appropriate number of time steps that allows the atoms to sample all of configuration space within the imposed volume.

3.4.1 Nosé-Hoover thermostat

A common computational method for treating temperature in MD simulations is the Nosé-Hoover thermostat (Nosé, 1984). In the Nosé-Hoover thermostat, a fictitious dynamical variable is introduced and acts as a frictional parameter, which slows down or accelerates particles until the temperature reaches a desired value. The equations of motion in 3-dimensions that describe the thermostat are:

$$m_i \frac{d^2 r_i}{dt^2} = f_i - \zeta m_i v_i \tag{3.12}$$

$$\frac{d\zeta(t)}{dt} = \frac{1}{Q}\left[\sum_{i=1}^{N} m_i \frac{v_i^2}{2} - \frac{3N+1}{2} k_B T\right] \tag{3.13}$$

where m_i is the mass of the atom, r_i is its position in 3-D space, t is time, f_i is the force the atom is subjected to, ζ is the friction, v_i is the velocity, Q determines the relaxation of the dynamics of the friction, N is the number of atoms, k_B is the Boltzmann constant, and T denotes the target temperature. The temperature using this thermostat is not fixed, but tends towards the target value.

3.5 VASP inputs and parameters

In this thesis, I implement *ab initio* molecular dynamics calculations using the VASP code (Kresse and Furthmuller, 1996). VASP requires five different input files: INCAR, POSCAR, POTCAR, KPOINTS, and a submission script. The POSCAR file contains the initial atomic configuration. It is user generated, and lists the cell size, the type and number of each atom, and the atomic coordinates. The POTCAR file contains the pseudopotentials for each atomic species, listed in the order specified in the POSCAR file. The KPOINTS file specifies the *k*-point positions. It lists the gamma point division of the Brillouin zone and the shift from that position. In this work, I used a Monkhorst-Pack generating scheme (Choudhary and Tavazza, 2019), which is the most commonly used flavor for automatic *k*-point grid generation and allow the subdivisions of the Brillouin zone to be supplied manually. Use of a Monkhorst-pack generating scheme is common for treatment of liquids at extreme conditions. I also used only one *k*-point, which is sufficient to describe a liquid. Finally, the INCAR file contains all of the details of the simulation and lists the selected parameters. The INCAR file is also where one can specify whether a spin-polarized calculation is run, and any Hubbard *U* parameters. A spin-polarized calculation will calculate magnetic moments of the atoms. Initial magnetic moments are specified for each ion, and the total magnetization is computed by subtracting the total number of spin-down configurational states from the total number of spin-up configurational states. Hubbard *U* parameters are implemented when systems contain atoms with transition metals, which have strongly correlated d and f electrons that are poorly treated by LDA or GGA alone. Conventional DFT methods without a Hubbard *U* can miscalculate the electron-electron repulsion, resulting in overestimation of the delocalized electrons to give a metallic ground state

in otherwise insulating materials. The Hubbard *U* parameter characterizes the intra-atomic Coulomb repulsions, and DFT with a Hubbard *U* treats the correlation effects well and accurately predicts magnetic insulators.

In this thesis, I implement *ab initio* molecular dynamics calculations using the PAW method of density functional theory with the VASP code. I use the generalized gradient approximation in the PBE form to treat electron exchange and correlation. All calculations are spin-polarized and use a Hubbard *U* parameter. The selected parameters are commonly used to describe liquids at high pressures ((Karki et al., 2020; Solomatova and Caracas, 2021) and have been tested against experimental data from silicate glasses (Kim et al., 2018; Prescher et al., 2014) to ensure accuracy of the results.

CHAPTER 4

SPECIATION AND COORDINATION OF CARBONATE-SILICATE-METAL MELTS

4.1 Introduction

Carbon is ubiquitous in the Earth's crust, but the amount and role of carbon in the deep Earth is less well understood. Carbon is regularly subducted into the mantle in the form of carbonates (Kelemen & Manning, 2015; Tao et al., 2018). However, out of an estimated yearly total of 62 megatons of carbonate being subducted per year (Clift, 2017), estimates of the amount of carbonate that survives into the lower mantle vary from 0.0001 to 52 megatons per year (Dasgupta & Hirschmann, 2010; Kelemen & Manning, 2015). The large discrepancy in estimation stems from carbon's varied behavior under specific thermodynamic and chemical conditions. For instance, carbonates are known to melt at relatively low temperatures (at 21 GPa, ~2000 K for $CaCO_3$ and ~1350 K for carbonated MORB) (Li et al., 2017; Thomson et al. 2016), to form diamonds and carbides under reducing conditions (Rohrbach & Schmidt, 2011; Stachel & Luth, 2015), and to react with surrounding mantle phases (Dorfman et al., 2018; Lv et al., 2021). However, recent evidence indicates that carbonates could be present in the lower mantle. Inclusions in diamonds returned from the top of the lower mantle contain carbonates coexisting with lower mantle phases (Agrosì et al., 2019; Korsakov & Hermann, 2006). Recent measurements of the metal-silicate partitioning coefficient of carbon show that carbon is less siderophile than originally thought (Fichtner et al., 2021; Fischer et al., 2020), indicating that less carbon is sequestered in the core, and could be stored in the mantle instead.

If carbonates are stable and present in the lower mantle, they are likely reacting with surrounding mantle phases. Previous studies of carbonate reactions in the lower mantle focus on

reactions of solid carbonates with silicates and metals (Dorfman et al., 2018; Lv et al., 2021; Martirosyan et al., 2016). However, few studies have examined carbonate melt interactions in the lower mantle. Carbonates have relatively low melting temperatures, allowing for generation of melt at present day mantle conditions. Additionally, the presence of volatiles such as carbon or water is known to cause melting point depression in silicates (Dasgupta et al., 2007). Understanding the behavior and interaction of carbonate melts in the Earth's interior is important to understand Earth's formation and evolution. In the early Earth, carbonate melts could react with both silicate and metal melts in the magma ocean, influencing how carbon was sequestered and stored. In the present day, carbonate, silicate, and metal melts could interact and mix freely at the core-mantle boundary, influencing the composition of the core and the density of melts in the deep mantle.

We examine the speciation and the coordination of a carbonate-silicate-metal melt at conditions relevant to a magma ocean and to the present-day Earth's lower mantle. Previous studies examine carbonate melts (Koura et al., 1996; Li et al., 2017; Xu et al., 2020), carbon-bearing silicate melts (Bajgain & Mookherjee, 2021; Ghosh & Karki, 2017; Ghosh et al., 2017; Karki et al., 2020), carbon and iron-bearing silicate melts (Karki et al., 2020; Solomatova & Caracas, 2021; Solomatova et al., 2019), and carbon partitioning between silicate and iron melts (Zhang & Yin, 2012). Our studied composition differs from previous studies in that it has subequal amounts of carbon, silicon, and metal, and acts as a representative composition of the types of mixed melts that could be present in the deep Earth. We examine how coordination distribution, speciation, cation diffusivity, and electrical conductivity evolve as a function of

pressure and temperature. These features have implications for melt properties, such as viscosity, miscibility, and reactivity with other mantle phases.

4.2 Methods

Ab initio molecular dynamics calculations were performed with density functional theory using the Vienna *ab initio* simulation package (VASP; Kresse & Furthmuller, 1996). The projector-augmented wave method (Blochl, 1994) was used to represent the core electrons. The generalized gradient approximation in the Perdew-Burke-Ernzerhof form (Perdew et al., 1996) was used to treat electron exchange and correlation. The calculations were spin polarized, meaning that the d electron spin states were unconstrained at all temperatures and pressures. A Hubbard U_{eff} (U-J) parameter of 4 eV was applied. In previous tests on iron-bearing pyrolite melt, a U_{eff} value of 4 eV was found to increase the magnetic moment of the iron atoms with only a small pressure effect (<1 GPa) (Caracas et al., 2019). The kinetic energy cutoffs for the plane-wave expansion of the wavefunctions were set to 600 eV. We used the canonical ensemble with constant volume, temperature, and number of atoms and with a Nosé-Hoover thermostat (Hoover, 1985; Nosé, 1984). Simulations were performed at 3,000 and 4,000 K and at volumes corresponding to pressures of 0-45 GPa at 3,000 K and 1-148 GPa at 4,000 K, with time steps of 1-2 fs for 18-80 picoseconds. Simulations at 3,000 K and at pressures above 45 GPa were not included due to the low mean-square displacement of the atoms suggesting glass-like rather than melt behavior, which indicates that the atoms in these simulations do not access enough configurational space to compute reasonable speciation statistics (see also Figure 4.1). The Brillouin zone was sampled at the gamma point. The mean-square displacement as a function of time shows a ballistic regime below approximately 1,000 fs, after which the atoms reach a

diffusive regime. All calculations were run with a minimum of two starting configurations, and results were averaged. For the density of states calculations, a k-point grid of either 8x8x8 or 6x6x6 was used depending on the density of the melt, where the number in the grid corresponds to the number of subdivisions along the reciprocal lattice vectors. Larger numbers indicate a greater sampling density, and lead to more accurate calculations of the electronic density of states. The conditions for all simulations are listed in Table B.1.

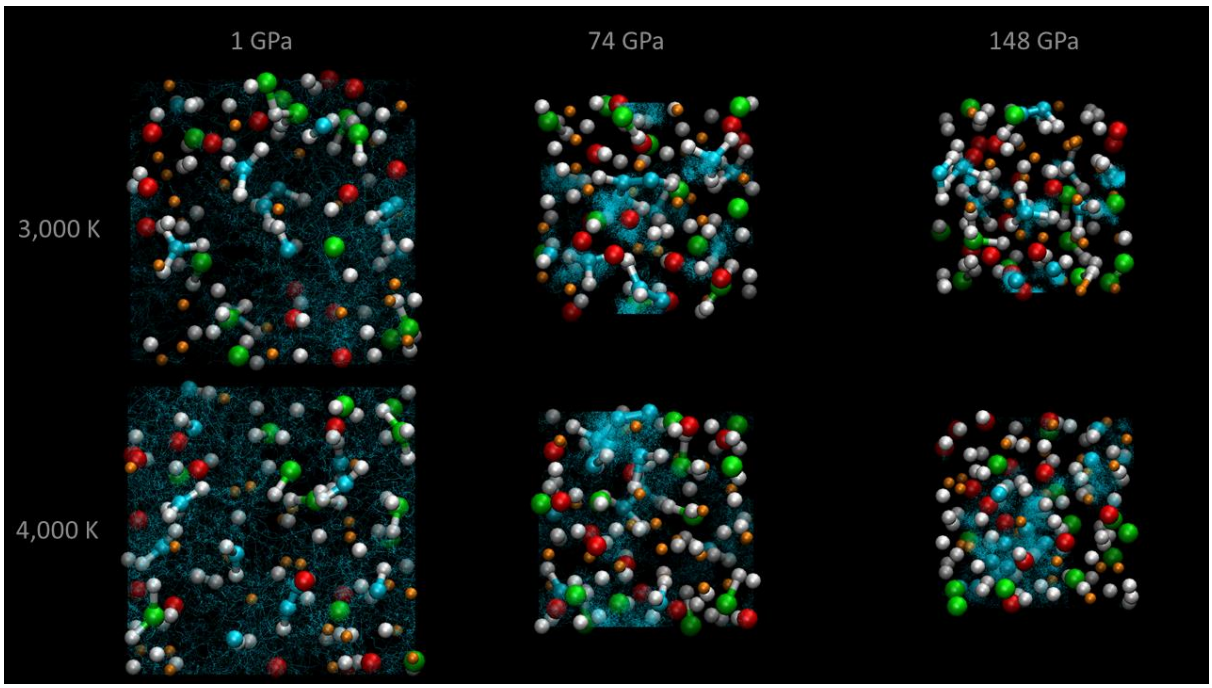

Figure 4.1: Carbon trajectory paths at 1, 74, and 148 GPa at 3,000 K and 4,000 K after 18,000 fs. The thin blue lines trace the paths of all 12 carbon atoms over the course of each simulation. Carbon diffuses through the entire cell at both 3,000 and 4,000 K at 1 GPa. At 74 and 148 GPa at 3,000 K, carbon barely moves over the course of the simulation, exhibiting glasslike rather than molten behavior. For this reason, these results were not included in the analysis. Additionally, the simulation times were doubled for all melts at 4,000 K due to the sluggish movement of carbon at 74 and 148 GPa after 18,000 fs.

The melt composition represents a carbonatite-metal melt with stoichiometry $Mg_{24}Fe_{13}Si_{12}C_{12}O_{72}$ (Figure 4.2). The composition can be split into 12 $MgSiO_3$ units, 12 $MgCO_3$ units, and 13 Fe units, for subequal amounts of silicon, carbon, and iron metal. Additionally, a simulation of an oxidized melt with stoichiometry $Mg_{20}Fe_{17}Si_{12}C_{12}O_{72}$ was conducted, where four magnesium atoms were replaced with four iron atoms to add ferrous rather than metallic iron to the starting composition. Bond distances were determined from the pair distribution functions (Figure 4.3). The first peak in the pair distribution function approximates the average bond length, while the first minimum in the pair distribution function marks the radius of the first coordination sphere for the reference atom. This minimum translates to the maximum acceptable

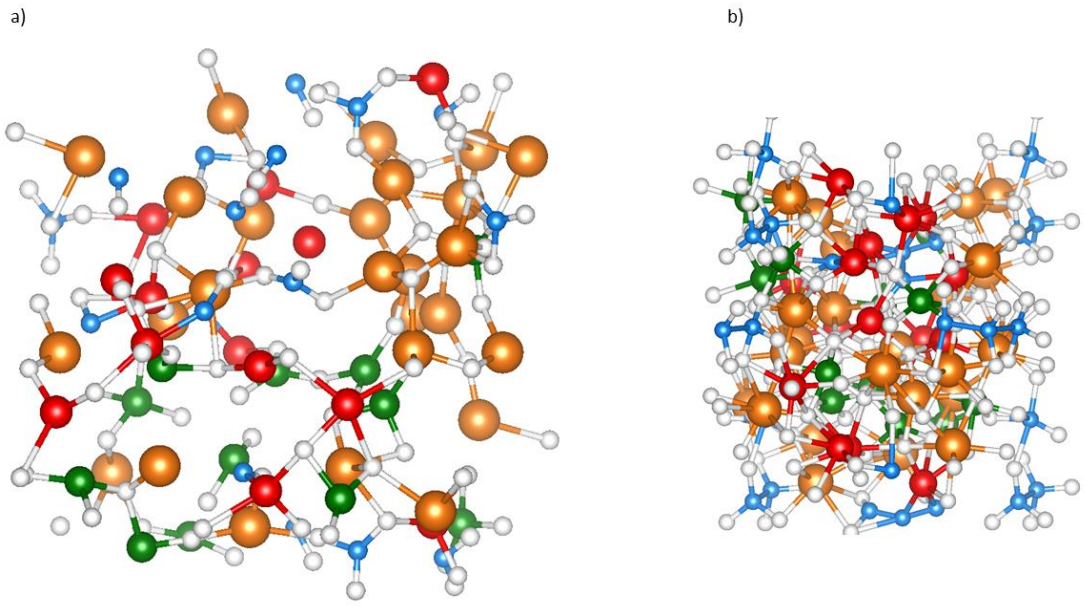

Figure 4.2: Structure of the carbonate-silicate-metal melt at a) 1 GPa and 4,000 K and b) 148 GPa and 4,000 K. Carbon is blue, silicon is green, iron is red, magnesium is orange, and oxygen is white. At low pressure, carbon has one, two, or three-fold coordination, and silicon has tetrahedral coordination. At high pressure, carbon adopts a tetrahedral coordination, and silicon is octahedrally coordinated.

bond distance for a bonding pair, and the fitted minimum values were used in the speciation and coordination analysis.

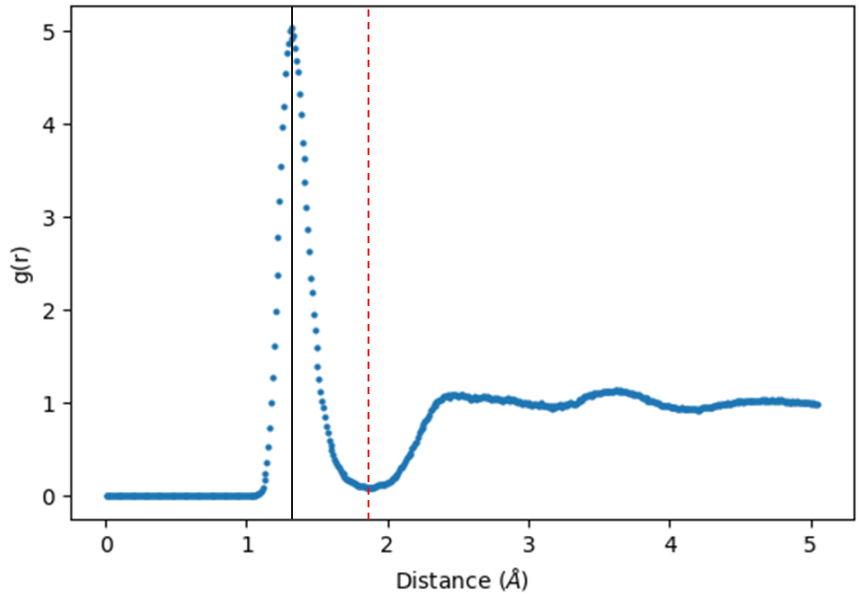

Figure 4.3: The pair distribution function of C-O at 3,000 K and 45 GPa. The solid black line marks the maximum in the pair distribution function and corresponds to the average bond length for C-O. The dashed red line marks the first minimum in the pair distribution function and corresponds to the maximum acceptable bond length to be considered a C-O bond. First minimums are used in speciation and coordination analysis to define a bond.

4.3 Results and Discussion

Using *ab initio* molecular dynamics simulations on a carbonate-silicate-metal melt up to core-mantle boundary pressures and temperatures of either 3,000 or 4,000 K, we evaluate the effects of pressure and temperature on interatomic bonds, chemical speciation, coordination states, cation diffusivity, and electrical conductivity.

4.3.1 Interatomic Bonds

The most frequent bond distance for an element pair corresponds to the first maximum in the pair distribution function (Figure 4.3). We take this maximum to be the average bond length. At 3,000 K and ambient pressure, we find average bond distances of 1.21 Å for C-O, 1.35 Å for C-C, 1.64 Å for Si-O, 1.87 Å for Si-C, 1.91 Å for Fe-O, 1.95 Å for Mg-O, and 2.03 Å for C-Fe (Figure 4.4, Tables B.2-B.3). Between 3,000 K and 4,000 K, bond lengths are similar, indicating that temperature does not have a large effect on bond length. Average bond length changes with increasing pressure and increasing coordination. With no change in melt structure, bonds would shorten and polyhedra shrink as ions move closer together. However, with increasing coordination, bonds can lengthen as polyhedra expand. At 4,000 K, C-Fe, Si-C, and Mg-O bonds demonstrate the most constant decrease in length over the pressure range studied. Other bonds decrease in length less dramatically. For these bonds, the pressure effect is accommodated mostly in the second coordination sphere rather than the first. All bonds decrease in length beyond 117 GPa. However, at pressures below 117 GPa, Fe-O, Mg-O, Si-O, C-C, and C-O bonds lengthen, corresponding to coordination changes in the cations (Figure 4.12). Fe and Mg have similar coordination environments, and Mg-O and Fe-O bonds exhibit similar behavior, lengthening during a rapid increase in coordination from 1 to 20 GPa before decreasing as the coordination increase slows. Si-O bonds lengthen between 15 and 70 GPa, the pressure regime when silicon coordination increases most rapidly, but remain largely unchanged over the entire pressure range studied. At 1 GPa, carbon species are molecular, and do not interact with the melt network. Thus, bond lengths at 1 GPa are far shorter than bond lengths at the other pressures studied. In fact, at 148 GPa, C-O and C-C bonds are longer than at 1 GPa (1.30 Å and 1.39 Å at

148 GPa, respectively, compared to 1.20 Å and 1.27 Å at 1 GPa). In the first 45 GPa, C-O and C-C bonds lengthen, corresponding to carbon's threefold to fourfold coordination change, and begin to shorten beyond 45 GPa.

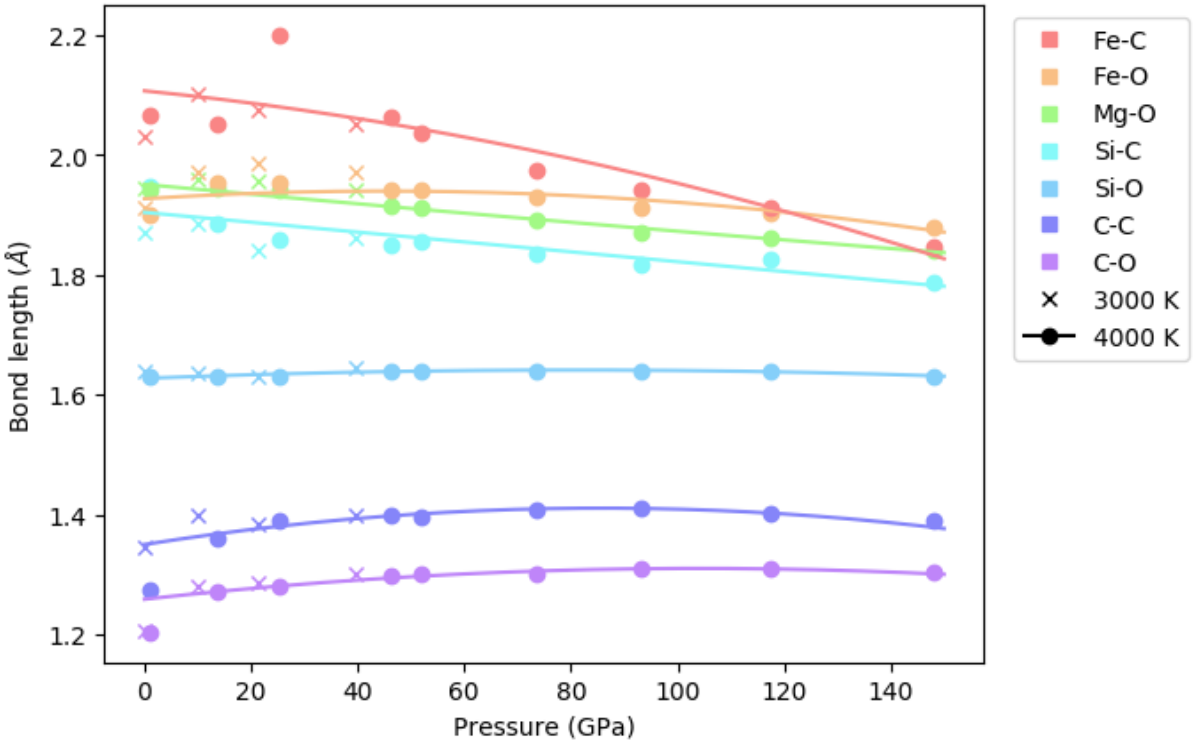

Figure 4.4: Average bond lengths of all bonding elements pairs as a function of pressure, as estimated from the first maximum in the pair distribution function.

4.3.2 Chemical Speciation

Through the definition of interatomic bonds, we identify and quantify chemical species in the melt. To simplify our analysis, we define a species as a central cation and the bonding atoms within the first coordination shell of that cation. This formalism allows us to easily compare coordination states and atomic bonding between cations and at various thermodynamic conditions. There is no minimum lifetime to be counted as a species, and thus, even species that

last for 1 fs in the simulation are counted. Speciation in the simulated carbonate-silicate-metal melt is complicated due to carbon's ability to act as both a cation and an anion. Carbon bonds to every element in the simulation except magnesium. Iron and silicon bond to both oxygen and carbon, and magnesium bonds only to oxygen. Carbon's bonding versatility allows for the creation of a multitude of species (Figure 4.5a, Table B.4). Over the entire 46 ps simulation at 117 GPa and 4,000 K, C_2O_3, C_2O_2, and FeC_2O_2 account for 33% of carbon species, and another 171 species account for the remaining 67%. The species formed are quite diverse and often have unusual bonding environments. Some examples of different types of carbon bonding are

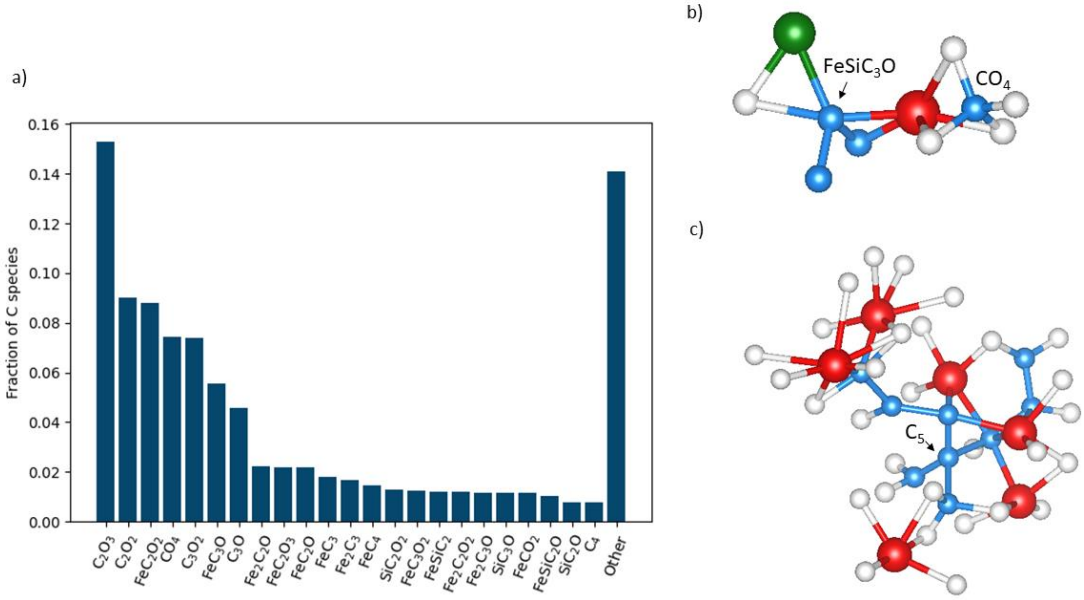

Figure 4.5: a) Variety of carbon species formed at 117 GPa and 4,000 K and their relative abundances. Carbon forms a diversity of bonds, and many species are present. b) and c) Examples of carbon species. Atoms are carbon (blue), oxygen (white), silicon (green), and iron (red). Magnesium atoms have been omitted for clarity. b) An example of a carbon atom exhibiting the four types of carbon bonds (C-Fe, C-C, C-O, and C-Si) (left) and an example of a carbonate group, where carbon is only bonded to oxygen (right). c) An example of a carbon-iron cluster consisting of nine carbon atoms and six iron atoms. A central carbon atom forms four C-C bonds, and could be a seed nucleus for diamond formation.

displayed in Figure 4.5b and c. In Figure 4.5b, carbon forms direct bonds to carbon, oxygen, silicon, and iron simultaneously to create a $FeSiC_3O$ species. While $FeSiC_3O$ is an example of an unusual bonding environment, we see an example of a more conventional carbon group in close proximity, a carbonate (CO_4), where carbon is bound only to oxygen. Figure 4.5c contains an example of a carbon-iron cluster containing nine carbon atoms and six iron atoms, demonstrating carbon's ability to polymerize and to bond with metal. Interestingly, the iron atoms are on the periphery of the carbon cluster, which contains a C_5 species that could act as a seed nucleus for diamond formation. The arrangement of the iron and carbon atoms suggests that diamonds grow from metallic liquids in the mantle, as suggested previously through analysis of metallic inclusions in diamonds (Smith et al., 2016). Both images shown in Figure 4.5 are a sample of the varied species carbon forms.

To evaluate speciation changes as a function of pressure, we examine bond abundances. Carbon displays the most varied speciation of the cations studied. Figure 4.6a plots the fraction of all carbon bonds that are C-X, where X is the bonding element to carbon, either O, C, Fe, or Si, as a function of pressure and temperature (see also Tables B.5-B.6). The 1 GPa simulations have notably different C-C and C-O bond abundances compared to the other pressure points. C-O bonds make up 87% of carbon bonds, while C-C bonds are low, at only 3% of carbon bonds. This discrepancy arises because at 1 GPa, carbon forms mostly CO and CO_2 molecules (Figure 4.12e). Beyond 1 GPa, carbon dissolves into the liquid and bonds more extensively with elements other than oxygen. In the 4,000 K results, C-Fe and C-C bonding both increase with pressure. C-Fe bonding increases linearly. At 1 GPa, 8% of all carbon bonds are C-Fe bonds, but at 148 GPa, 21% of all carbon bonds are C-Fe bonds. C-C bond abundances also increase with

pressure, but the majority of the change happens within the first 25 GPa, from 3% at 1 GPa to 27% at 25 GPa. Subsequently, C-O bonding shows an opposite trend with C-C bonding, and decreases rapidly from 1 to 25 GPa. C-O bond proportions fall from 87% at 1 GPa to 58% at 25 GPa to 51% at 148 GPa. C-Si bond abundances rise from 1% at 1 GPa to 5% at 37 GPa, before falling back to 2% at 148 GPa. Speciation results at 3,000 and 4,000 K show similar trends in bond abundances. Figure 4.6b contains the same bonding information as Figure 4.6a, plotted in coordination space (see Tables B.7-B.8). As pressure increases, the total number of carbon bonds increases as the average coordination number rises (Figure 4.12). However, the relative proportions of individual bonds evolve with pressure, indicating carbon's changing affinity for different elements. At 1 GPa and 4,000 K, carbon's average coordination to oxygen is 1.7, which accounts for 87% of the total coordination. At 148 GPa and 4,000 K, carbon's average coordination to oxygen is 2.1, which accounts for just 51% of the total coordination. The small rise in C-O coordination is outpaced by more rapid rises in C-C and C-Fe coordination with pressure. From 1 GPa to 148 GPa, C-C coordination increases from 0.1 to 1.0, and carbon-iron coordination increases from 0.2 to 0.9. Although carbon's affinity for carbon and iron increases with pressure, at no point is C-C or C-Fe bonding more abundant than C-O bonding. The overall effect is that as pressure increases, carbon begins to play a similar role as oxygen in the melt network, forming bonds to carbon, iron, and silicon. Carbon has been observed to substitute for oxygen in amorphous silicate structures in previous 1 bar NMR studies (Sen et al., 2013), indicating that carbon prefers to replace oxygen, an anion, instead of silicon, a cation, in the melt network.

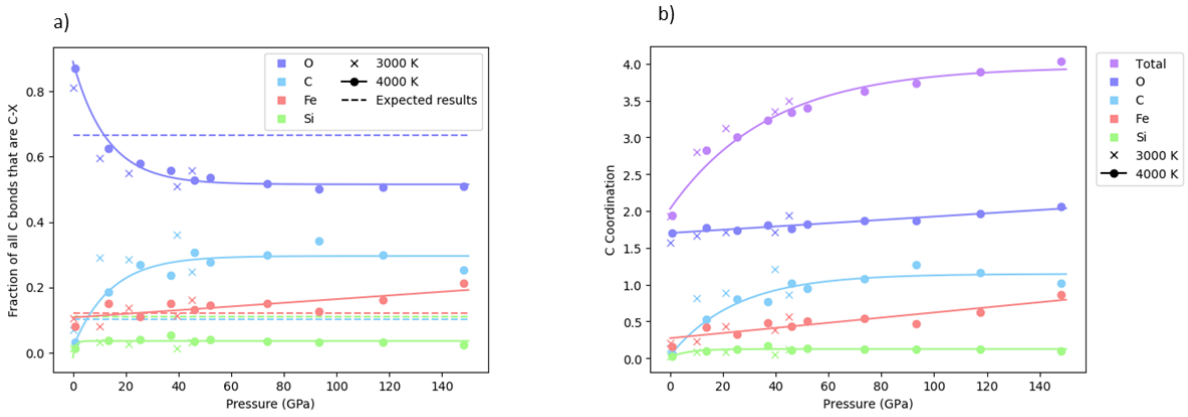

Figure 4.6: Carbon speciation as a function of pressure and temperature. a) Displays the fraction of all carbon bonds in a simulation that are C-O (purple), C-C (blue), C-Fe (red), and C-Si (green) bonds. C-C and C-Fe bonding increases with pressure, while C-O bonding decreases. Dashed lines are expected results from statistical sampling. Compared to statistical sampling, C-C and C-Fe bonding are more abundant than expected while C-O and C-Si bonding are less abundant than expected. b) Displays the average coordination number of carbon to oxygen (purple), carbon (blue), iron (red), silicon (green), and to all elements (lilac).

To put these observations into context, we compare our 4,000 K simulation results to expected results from statistical sampling (Figure 4.6a). Statistical sampling is calculated by assuming that each cation has no chemical preference for any of the bonding atoms. In other words, what bond abundances would we expect to see if each cation coordinates with a randomized selection from the available anions? To do so, we identify the bonding atoms for each cation type and calculate the fraction of total bonds we expect for each cation-anion pair. For example, we have identified that iron bonds only with carbon and oxygen. 84 anions (72 oxygen and 12 carbon) are available, and thus, 86% (72/84) of iron's bonds should be to oxygen, and 14% (12/84) to carbon, assuming no chemical preference for either. For carbon, we expect the number of C-C, C-Fe, and C-Si bonds to be similar due to the subequal amounts of the three elements. We also expect C-O bonds to make up the majority of carbon bonds. At 1 GPa, C-O

bonding is more prevalent than expected, and C-C, C-Fe, and C-Si bonding are all less prevalent. This result is unsurprising as carbon mostly forms molecular CO and CO_2 at these conditions. However, above 1 GPa, C-C and C-Fe bonding are more prevalent than expected, while C-O and C-Si bonding are less prevalent. The discrepancy between expected and actual results only grows with increasing pressure.

The large percentage of C-C and C-Fe bonds in our simulations suggests both a tendency for carbon to polymerize and to mix with iron to form more reduced species than might otherwise be expected in this oxygen-rich system. Indeed, the presence of Fe may aid in the formation of C-C bonds, as suggested by Belonoshko et al. (2015). Carbon appears to become more siderophile with increasing pressure, a phenomenon that has been previously reported (Dasgupta et al., 2013; Solomatova et al., 2019). Additionally, the low abundance of C-Si bonds indicates that carbon is less likely to mix with the silicate than might otherwise be expected. This is suggestive of silicate and carbonate melt immiscibility, which has been well documented in carbonatites (Bodeving et al., 2017; Lee & Wyllie, 1998).

Our work examines a melt with subequal amounts of carbon, silicon, and metal, differing from previous *ab initio* carbon-bearing melt studies (Du et al., 2017; Ghosh et al., 2017; Karki et al., 2020; Solomatova et al., 2019). In Figure 4.7, we compare the carbon speciation results of this work at 4,000 K directly to the work of Solomatova et al. (2019), which examined a carbon-bearing pyrolite melt (pyrolite + 3.35 wt% CO), and the work of Karki et al. (2020), which examined a carbon, hydrogen, and iron-bearing silicate melt, where the volatile species are added in both oxidized and reduced forms. We will thus refer to our system as carbonatitic, the system of Solomatova et al. (2019) as pyrolitic, and the oxidized and reduced systems of Karki et al.

(2020) as oxidized silicate and reduced silicate, respectively. The VASP code and similar input parameters were used for all three studies, with the main difference being that the Karki et al. (2020) system did not run spin-polarized calculations and had a smaller plane wave cutoff energy than both this study and Solomatova et al. (2019). The redox conditions of the system play a large role in speciation (Ghosh et al., 2017). The relative redox conditions between the four systems can be approximated by comparing the C/O ratios. The oxidized silicate melt is the most oxidized composition with a C/O ratio of 0.067 compared to 0.082, 0.083, and 0.170 for the pyrolitic, reduced silicate, and carbonatitic melts, respectively. We examine carbon bonds to the same four elements (carbon, oxygen, iron, and silicon) in all systems. In the case of the oxidized

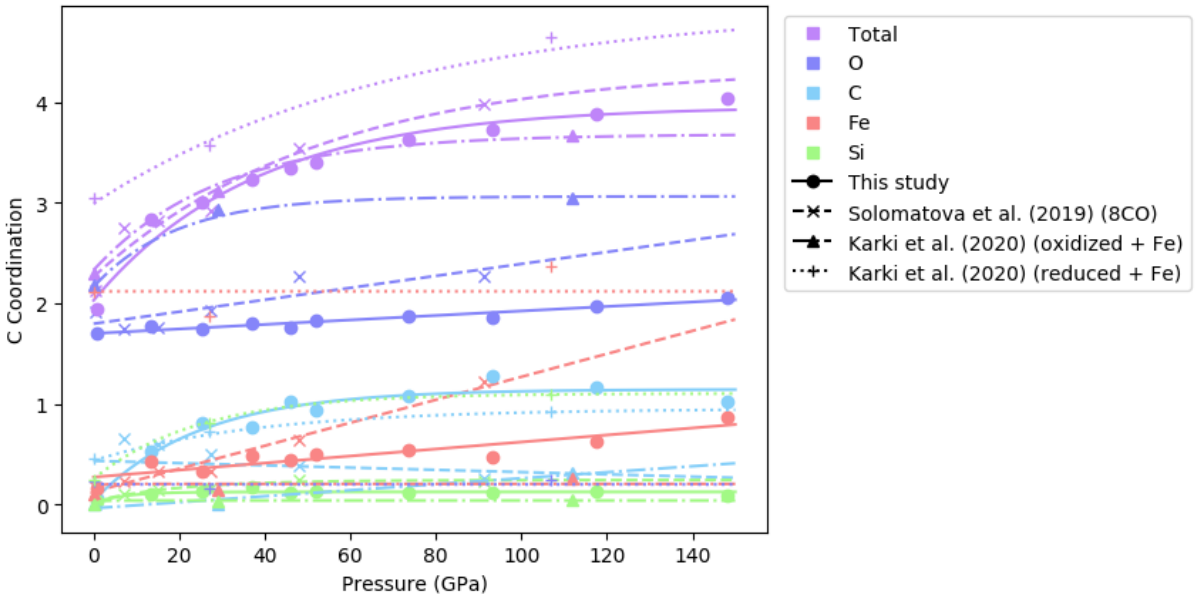

Figure 4.7: Carbon speciation as a function of pressure and temperature. Displays the average coordination of carbon as measured at 4,000 K in this study (solid line, circles) versus Solomatova et al. (2019) (dashed line, x's) and Karki et al. (2020) (dashed dotted line, triangles for oxidized melt and dotted line, plusses for reduced melt).

and reduced silicate systems, we have removed the bonds and subsequent coordination to hydrogen atoms for comparison purposes.

Average carbon coordination is similar between the carbonatitic, pyrolitic, and oxidized silicate systems. The reduced silicate system has a larger carbon coordination than the other systems. This is unusual, as average carbon coordination numbers in the reduced silicate system approach a value of 4.5 at high pressures; typically, carbon species at lower mantle pressures adopt a fourfold coordination. The coordination of carbon to each individual element varies widely across systems. In the carbonatitic system, the average coordination to oxygen is lower than in the pyrolitic system, a difference that increases with depth. Carbon bonding in the oxidized silicate melt consists mostly of carbon-oxygen bonds. Subsequently, carbon bonding to all other elements is suppressed. Alternatively, in the reduced silicate melt, carbon bonding to oxygen is suppressed and bonding to all other elements is elevated. All systems show increased carbon-oxygen coordination numbers with increasing pressure. Carbon-silicon coordination is low in all systems but the reduced silicate system, which approaches a coordination number of one at high pressures. Most striking are the differences in carbon-carbon and carbon-iron coordination numbers between systems. Due to the greater number of carbon atoms in the carbonatitic system, we would expect to see more carbon-carbon bonding than in any of the other systems, and this is generally true. However, the carbon-carbon coordination in the reduced silicate system is very similar despite only 4% of the atoms being carbon versus 9% in the carbonatitic system, indicating that the redox conditions of the system greatly influence carbon's behavior. Additionally, the average coordination of carbon to carbon increases in all systems but the pyrolitic system, which decreases with pressure. This can be partly explained by the high

affinity of carbon for iron in the pyrolitic system; the increase in C-Fe bonding may inhibit an increase in C-C bonding. In both the carbonatitic and pyrolitic systems, C-Fe coordination increases with pressure. However, the rate of increase is larger in the pyrolitic system. In fact, at 148 GPa, carbon forms on average one greater bond to iron in the pyrolitic system versus the carbonatitic system (1.9 versus 0.9). The differences in C-C and C-Fe bond abundances between the carbonatitic and pyrolitic systems suggests that carbon becomes less siderophile when in the presence of more carbon and chooses instead to polymerize. This conclusion disagrees with a recent paper by Grewal et al. (2021) that measured carbon partitioning coefficients and found that carbon becomes more siderophile with increasing bulk carbon content of the system. However, these measurements were taken at 3 GPa, and our calculations span a broader range of pressures. At 3 GPa, C-Fe bonds are actually more abundant than in the pyrolitic system, and C-Fe bond abundances in the pyrolitic system only overtake the carbonatitic system around 20 GPa. In the oxidized and reduced silicate systems, carbon-iron coordination numbers are more scattered, but generally invariant with pressure. The coordination number fluctuates around a value of 2.1 in the reduced silicate system and a value of 0.1 in the oxidized silicate system. In general, the carbonatitic system displays a propensity for C-C bonding that is unmatched by the other systems, likely due to the high number of carbon atoms. The increase in C-C bonding leads to compensatory drops in C-O, C-Fe, and C-Si bonding as compared to the pyrolitic and oxidized silicate systems. Extrapolating this trend, we expect to see increased C-C bonding in systems containing more carbon, at the expense of other elements.

Due to the high proportion of C-C bonding in the carbonatitic system, we expand our speciation analysis beyond the first coordination sphere of individual atoms. Instead, we search

for clusters of carbon atoms, where a cluster consists only of carbon atoms bound together by C-C bonds. Figure 4.8a examines the average carbon cluster size as a function of pressure and temperature (see also Tables B.9-B.10). In the 4,000 K results, average carbon cluster size rapidly increases from 1.1 carbon atoms at 1 GPa to 3.5 carbon atoms at 37 GPa, in line with the general increase in carbon-carbon bonding from 1 to 37 GPa (Figure 4.6a). Beyond 37 GPa, the average carbon cluster size oscillates around a value of 3.2. The 3,000 K results are similar. There is a rapid increase in carbon cluster size from 1.1 carbon atoms at ambient pressure to 4.1 carbon atoms at 40 GPa, suggestive of carbon's ability to polymerize and form diamond-like clusters. Similarly, we examine the size of C-Fe clusters with pressure in Figure 4.8b (see also Table B.10). An iron-carbon cluster consists only of C-C and C-Fe bonds, and must have at least one C-Fe bond to be considered. Generally, as both C-Fe and C-C bonding increase with pressure (Figure 4.6a), average iron-carbon cluster size also increases with pressure. The average cluster size increases from an average value of 2.3 at 1 GPa and 4,000 K to an average value of 6.4 at 93 GPa. From 93 to 148 GPa, the average cluster size drops slightly to 5.4 atoms.

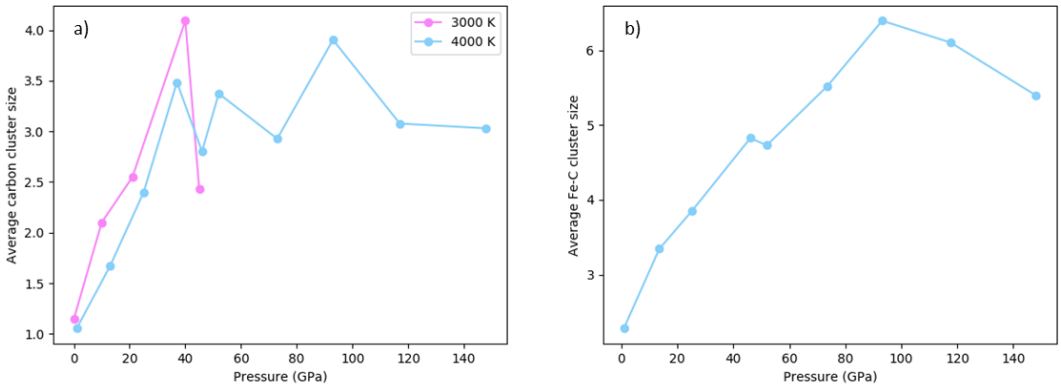

Figure 4.8: Average cluster sizes as a function of pressure and temperature for a) carbon only clusters and b) carbon-iron clusters. Cluster sizes generally increase with increasing pressure.

As C-C and C-Fe bond abundances rise with pressure, there is a decrease in carbonate abundance. Figure 4.9a examines carbonate speciation (carbon atoms bound only to oxygen and to no other element) as a function of pressure and temperature (see also Tables B.11-B.12). At the lowest pressure, the majority of carbon species are carbonates (69% at 3,000 K and 75% at 4,000 K). There is a rapid decrease in carbonate fraction with increasing pressure. At 13 GPa and 4,000 K, carbonate species are only 37% of total carbon species. From 13 to 148 GPa, carbonate percentage decreases more slowly to a value of 13%, as carbon increasingly forms bonds to other atoms (Figure 4.6a). The loss of carbonate species with increasing pressure indicates that carbon is becoming more reduced with depth. Although the total abundance of carbonates decreases with pressure, the abundances of individual carbonate coordination environments vary. More highly coordinated carbonate groups (such as CO_4 and CO_5) are more abundant at higher pressures, while carbonate groups with lower coordination are more abundant at lower pressures.

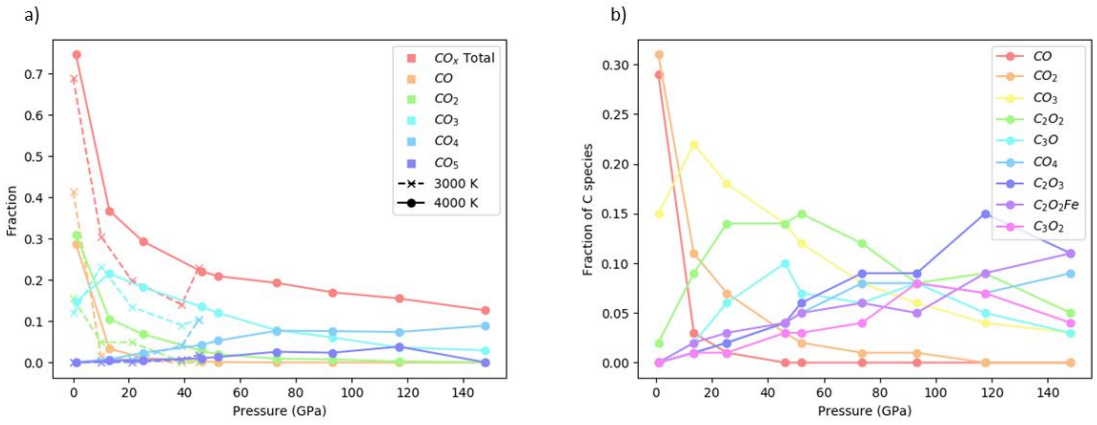

Figure 4.9: a) Abundances of carbonate species as a function of pressure and temperature. Individual carbonate coordination states are plotted in addition to the sum total of all carbonate groups (red line). b) Abundances of the nine most abundant carbon species across all 4,000 K simulations. Higher coordination species are more dominant at higher pressures, regardless of the elemental identity of the bonding atoms.

In fact, the relationship between more highly coordinated species and pressure holds for all carbon species, regardless of the coordinating atom. Figure 4.9b plots the abundances of the nine most common species across all 4,000 K simulations as a function of pressure (see also Table B.13). Species with higher coordination numbers are more dominant at higher pressures, regardless of the elemental identity of the coordinating atoms. For instance, at 13 GPa the three most dominant species are CO_3, CO_2, and C_2O_2, which exhibit either twofold or threefold coordination. At 148 GPa, the three most dominant species are C_2O_2Fe, C_2O_3, and CO_4 which all exhibit fourfold coordination.

Similar to our carbon speciation analysis, we evaluate iron speciation (Figure 4.10) and silicon speciation (Figure 4.11, see also Tables B.5-B.6). Iron and silicon both bond to two elements – oxygen and carbon. For both cations, speciation results are similar at 3,000 K and 4,000 K. From 1 to 148 GPa at 4,000 K the abundance of C-Fe bonds increases from 4% to 10%,

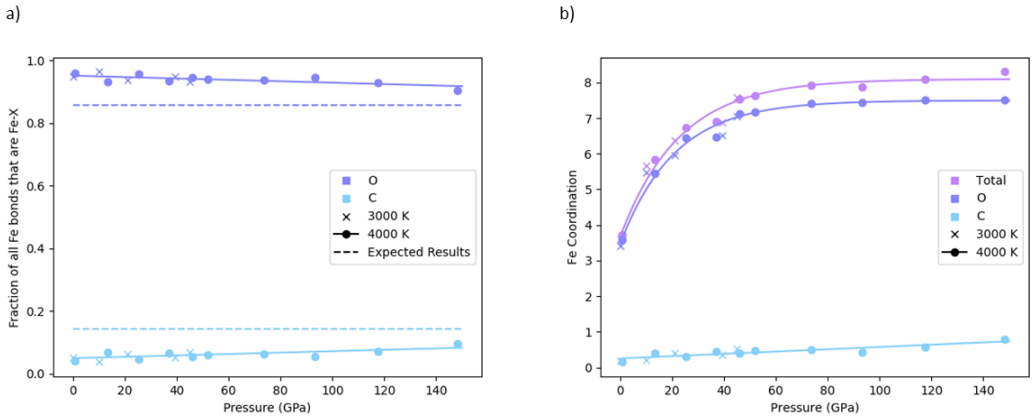

Figure 4.10: Iron speciation as a function of pressure. a) Displays the fraction of all iron bonds in a simulation that are Fe-O (purple) and C-Fe (blue) bonds. Dashed lines represent the results from statistical sampling. Fe-O bonding is more abundant than expected while C-Fe bonding is less abundant. b) Displays the average coordination number of iron to oxygen (purple), carbon (blue), and to all elements (lilac).

while the abundance of Fe-O bonds decreases from 96% to 90% (Figure 4.10a). The percentage of Si-C bonds increases from 0.8% at 1 GPa to 4% at 37 GPa, then decreases to 2% at 148 GPa and 4,000 K, with the balance taken up by Si-O bonds (Figure 4.11a). The speciation results are also presented in coordination space (Figure 4.10b and Figure 4.11b) and compared to the results from statistical sampling (Figure 4.10a and Figure 4.11a). Fe-O bonding is more prevalent and C-Fe bonding is less prevalent than expected from statistical sampling. The discrepancy between expected and actual results decreases with increasing pressure, as C-Fe abundance increases. Si-O bonding is also more prevalent while Si-C bonding is less prevalent than expected. This discrepancy increases with increasing pressure.

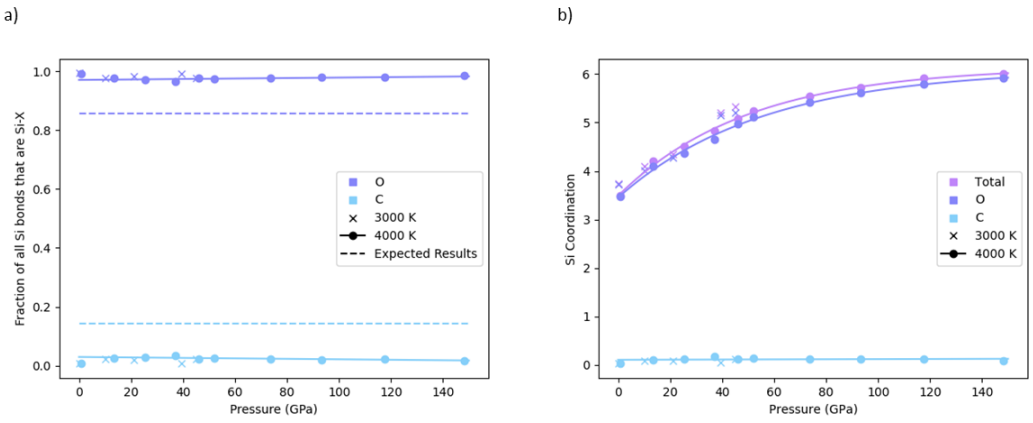

Figure 4.11: Silicon speciation as a function of pressure. a) Displays the fraction of all silicon bonds in a simulation that are Si-O (purple) and Si-C (blue) bonds. Dashed lines represent the results from statistical sampling. Si-O bonding is more abundant than expected while Si-C bonding is less abundant. b) Displays the average coordination number of silicon to oxygen (purple), carbon (blue), and to all elements (lilac).

4.3.3 Average coordination numbers

In a silicate melt, cation-oxygen bonds are typically the only bonds considered when evaluating coordination states (Ghosh et al., 2017; Solomatova & Caracas, 2019), as oxygen is

the most prominent bonding anion in the system. However, due to the complicated bonding in our carbon-rich system, we evaluate cation coordination to all bonding atoms, not just to oxygen.

The average coordination state of all cations increases with pressure (Figure 4.12a, Tables B.14-B.15). Iron's average coordination number increases from 3.7 to 8.3 from 1 to 148 GPa at 4,000 K. Over the same conditions, magnesium's coordination number increases from 4.0 to 7.8. For both elements, coordination increases rapidly from 0 to 45 GPa, then levels off. The coordination of both cations approaches eight at the highest pressure. Silicon's coordination increases gradually from tetrahedral at low pressure to octahedral at high pressure as expected from previous experimental (Williams & Jeanloz, 1988; Xue et al., 1989) and computational (de Koker et al., 2008; Ghosh et al., 2014; Karki et al., 2007) work on silicate melts and glasses. Carbon's coordination increases most rapidly from 1 to 13 GPa, where it evolves from twofold coordination to triangular coordination as it transitions from a molecular species to part of the

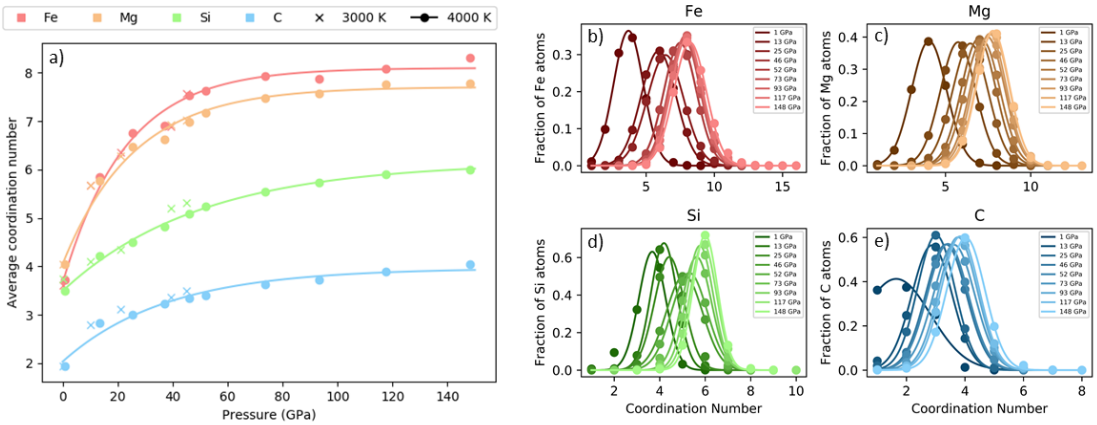

Figure 4.12: a) Average cation coordination number as a function of pressure and temperature. b-e) Coordination state distributions for b) iron, c) magnesium, d) silicon, and e) carbon as a function of pressure at 4,000 K. All distributions are fit to a gaussian profile and shift to higher coordination numbers with increasing pressure.

liquid framework. Beyond 13 GPa, coordination increases gradually from triangular coordination to tetrahedral coordination, mirroring the sp^2-sp^3 transition found in solid carbonates in the lower mantle (Boulard et al., 2015; Oganov et al., 2008). The 3,000 K results closely follow the 4,000 K results, and exhibit similar trends with pressure.

Figure 4.12 (b-e) plots the distribution of coordination states for iron, magnesium, silicon, and carbon at 4,000 K (also see Tables B.16-B.19). Generally, the distributions fit a gaussian profile and shift to higher coordination numbers with increasing pressure. The broadness of the distribution, measured by the full width at half maximum (FWHM) value, is an indication of the number of simultaneous coordination states and a proxy for the cation's preference for the central coordination number. Iron and magnesium have similar coordination distributions. Iron has the highest coordination numbers and the broadest distributions overall. For example, the FWHM value at 4,000 K and 117 GPa for iron is 2.70 versus 2.28, 1.53, and 1.36 for magnesium, carbon, and silicon respectively. Silicon coordination distributions are narrow when centralized around coordination numbers of 4 and 6 (FWHM values of 1.35 and 1.28), indicating its preference for regular coordination polyhedra. The distributions broaden when centralized around a coordination number of 5 (FWHM of 1.89). Carbon is the smallest cation, and therefore has the lowest coordination numbers. The coordination distributions are narrowest when centralized around threefold and fourfold coordination (FWHM values of 1.51 and 1.54), and broadest when transitioning between twofold and threefold coordination and between threefold and fourfold coordination (FWHM of 2.78 and 1.65). Coordination distributions are affected by temperature as well as pressure (Figure 4.13, Tables B.31-B.34). For all cations, distributions broaden with increasing temperature as greater thermal energy allows more simultaneous

coordination states to be accessed at a given pressure. On average, FWHM values for all cations increase by 0.27 when the temperature is increased from 3,000 to 4,000 K. For iron, the average coordination number slightly increases with temperature. Magnesium, silicon, and carbon's average coordination numbers slightly decrease with increasing temperature. A similar effect is observed in pyrolite melts (Solomatova & Caracas, 2019).

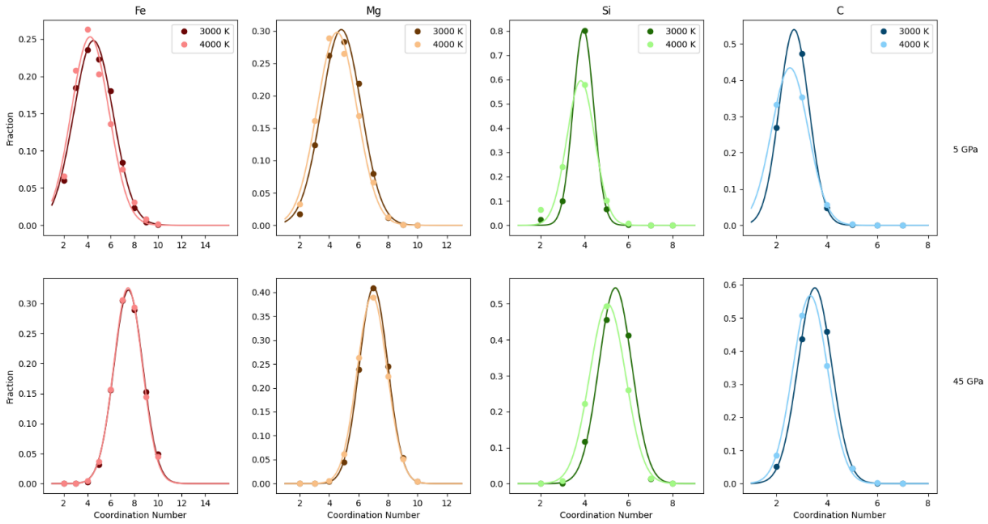

Figure 4.13: Coordination state distributions as a function of temperature at 5 GPa (top row) and 46 GPa (bottom row). With increasing temperature, distributions broaden and shift to lower average coordination numbers.

Coordination changes in the simulated melt are continuous. Silicon coordination at 4,000 K, for example, continuously increases from dominantly fourfold from 0 to ~30 GPa, to fivefold from 30 to ~60 GPa, and finally to sixfold from 60 GPa to >148 GPa (Figure 4.14, Tables B.16-B.19). Similarly, carbon coordination increases continuously from predominantly twofold from 0 to ~1 GPa, to threefold from 1 to 60~ GPa, to fourfold from 60 to >148 GPa. Iron and magnesium both jump from predominantly fourfold coordination at 1 GPa to predominantly

sixfold coordination at 13 GPa, but their coordination increases are continuous from sixfold to eightfold coordination. The continuous coordination changes in the melt are distinct from many glasses and solids, which tend to skip coordination states to achieve a preferred coordination at a given pressure and temperature. For instance, in many silicates in the mantle, silicon adopts a

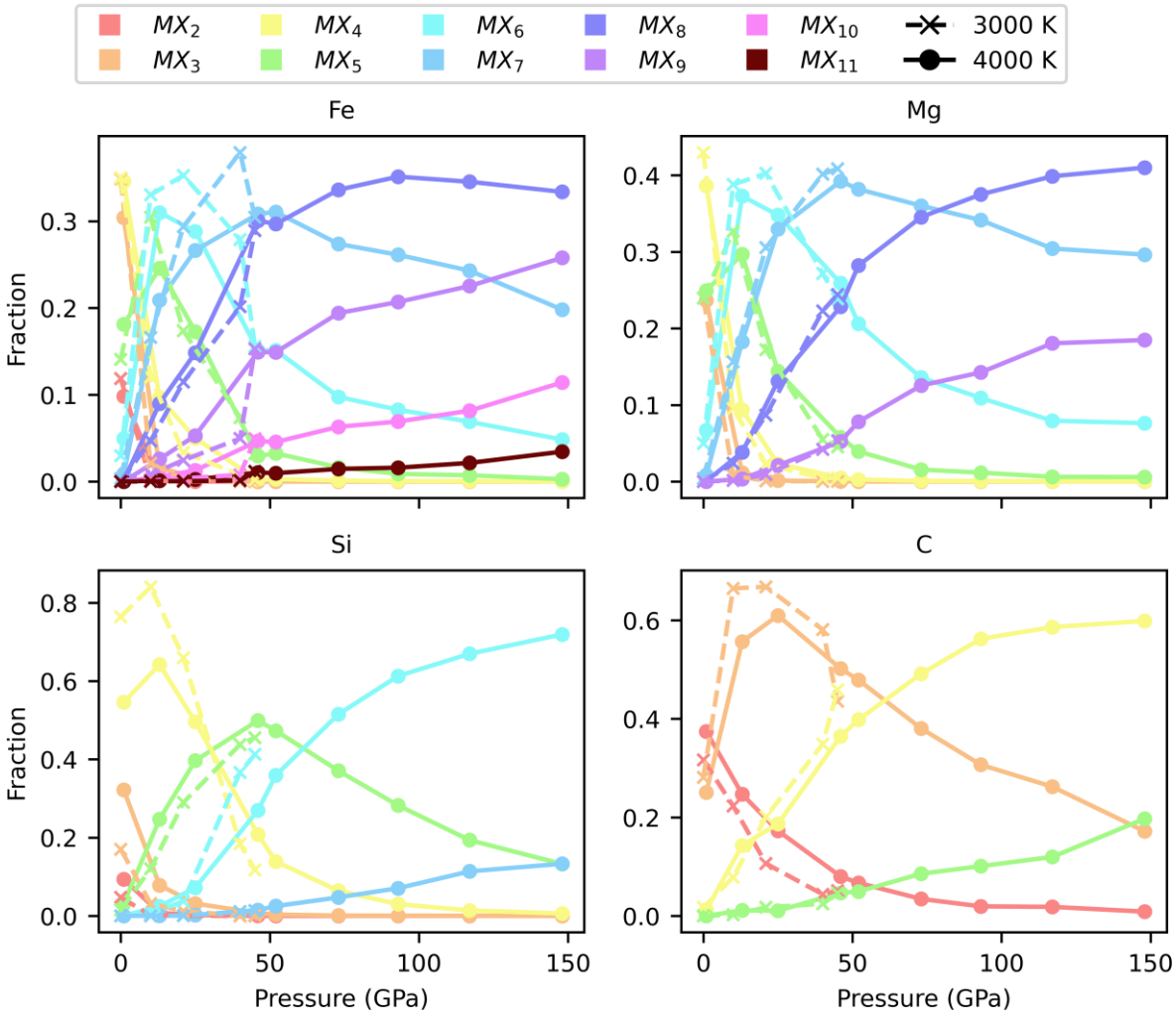

Figure 4.14: Abundances of coordination states as a function of pressure and temperature. Coordination states are color coded by the legend, where M indicates the cation of interest and X indicates a coordinating anion. For clarity, only two to eleven-fold coordination states are plotted. More highly coordinated cations are more abundant with increasing pressure. Most of the coordination changes occur in the first 50 GPa.

combination of fourfold and sixfold coordination states, rather than adopt a fivefold coordination state (Finger & Hazen, 2000; Xue et al., 1989). For all cations, higher coordination states are more abundant at higher pressures. Additionally, multiple coordination states coexist at the same conditions. For instance, carbon coordination at 52 GPa is 7% twofold, 48% threefold, 40% fourfold, and 5% fivefold.

Mean coordination lifetimes at 4,000 K are plotted in Figure 4.15 (see also Tables B.20-B.23). The lifetime of a specific coordination state is an indication of both its overall stability and the role of the cation as either a network former or a network modifier. Longer lifetimes typically indicate a network former, as the cation is largely unperturbed in the melt network, while shorter lifetimes indicate a network modifier. Coordination lifetime distributions are heavily skewed right (Figure B.1-B.3), but tend to have the same shape, suggesting that the mean coordination lifetime is a valid comparison of lifetime stability between cations. With increasing pressure, lifetimes shift to increasingly higher coordination states, indicating that at higher pressures, higher coordination numbers are more stable. However, the lifetimes of the coordination environments generally decrease with increasing pressure. For example, at 1 GPa, CX_1 species have the longest lifetime of all carbon species at 160 fs but at 148 GPa, CX_4 species have the longest lifetime at only 31 fs. Most of the changes in the lifetime distributions occur between 1 and 73 GPa, where the majority of coordination changes occur. Between 73 and 148 GPa, there are few changes in the lifetime distribution, matching the general flattening in the average coordination number for all cations at these pressures (Figure 4.12a). Silicon and carbon species have the longest lifetimes overall, but at 73 and 148 GPa, their average lifetimes are similar to iron and magnesium. The relatively long lifetimes at low pressure indicate that they

tend to be network formers at these conditions, as seen in previous studies on silicate melts and glasses (Kubicki & Stolper, 1995; Lesher et al., 1996). The longest lifetimes of silicon-bearing coordination environments are 157 fs, 39 fs, and 54 fs at 1 GPa, 73 GPa, and 148 GPa respectively. The longest lifetimes of carbon-bearing coordination environments are 160 fs, 28 fs, and 31 fs at the same conditions. Iron-bearing and magnesium-bearing coordination environments generally have shorter lifetimes, indicating that they behave more like network

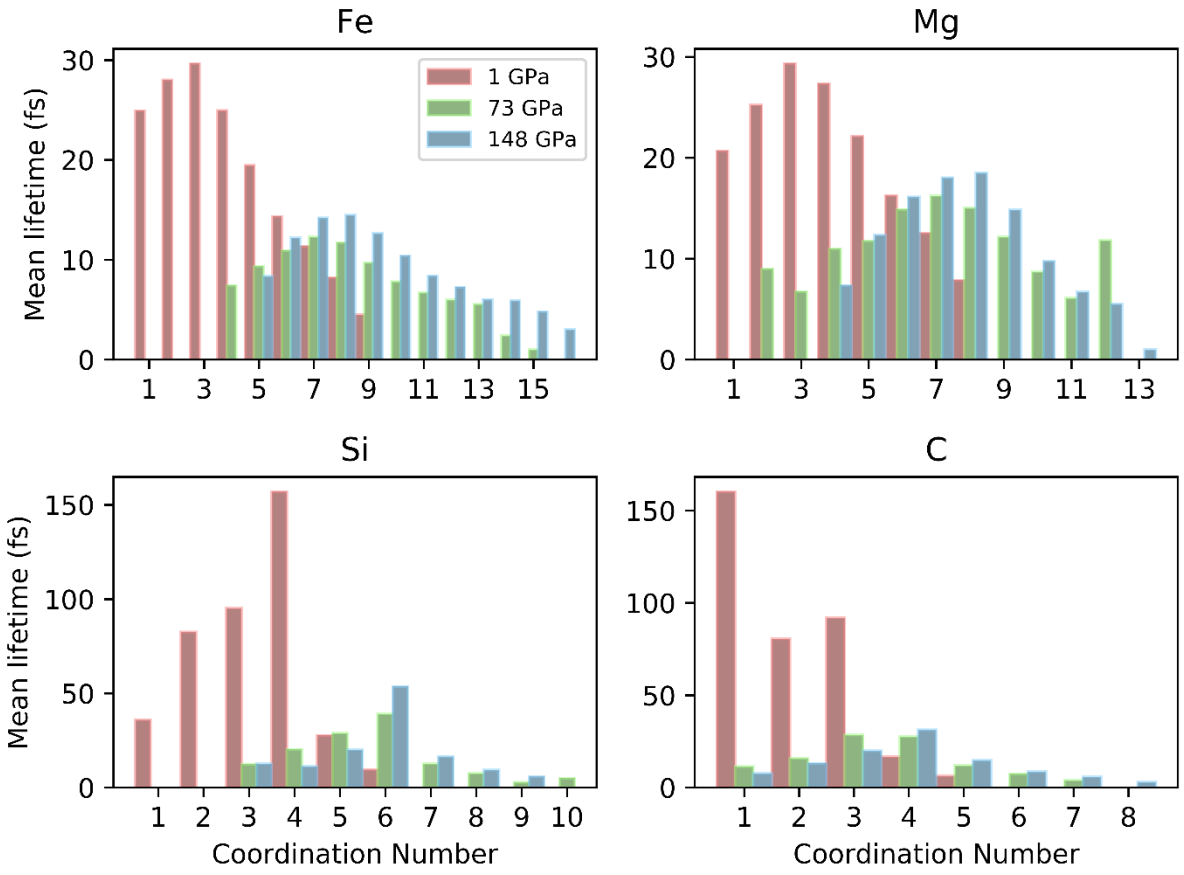

Figure 4.15: Average coordination state lifetimes in femtoseconds for a) iron, b) magnesium, c) silicon, and d) carbon at 1 GPa (red), 73 GPa (green) and 148 GPa (blue). With increasing pressure, lifetime distributions shift to higher coordination numbers, and mean lifetimes decrease substantially between 1 and 73 GPa.

modifiers. The longest lifetimes of iron-bearing coordination environments are 30 fs, 12 fs, and 14 fs, and the longest lifetimes of magnesium-bearing coordination environments are 29 fs, 16 fs, and 18 fs at 1, 73, and 148 GPa, respectively. Iron and magnesium have similar lifetimes across all pressures shown in Figure 4.15, whereas silicon and carbon have much longer lifetimes at 1 GPa compared to 73 and 148 GPa.

Overall, the simulations reveal that with increasing pressure, the melt evolves to a denser, more highly coordinated structure whose cations are rapidly exchanging nearest neighbors. The coordination polyhedra become increasingly transient species, while maintaining a relatively narrow spread of coordination numbers.

4.3.4 Redox conditions

To see how differing redox conditions affect melt behavior, we ran an additional simulation with an oxidized starting composition at 150 GPa and 4,000 K (see section 4.2 for simulation set up). FeO was added to the starting composition by replacing four Mg atoms with four Fe atoms to start with a mix of iron metal and FeO. The results are presented in Figure 4.16. Generally, speciation and coordination results are the same in both systems, with a few differences. C-Fe bonding is more abundant and C-C bonding is less abundant in the oxidized system (Figure 4.16b), although this observation can be explained by the increased number of Fe atoms in the system. Total carbonate percentage is slightly increased in the oxidized system (15% versus 13%), due to an increase of CO_4 groups. Additionally, we examined the effect of both pressure and redox conditions on the oxidation states of the elements in the simulation. To do so, we calculated Bader volumes, which involves finding the minima in the electronic charge

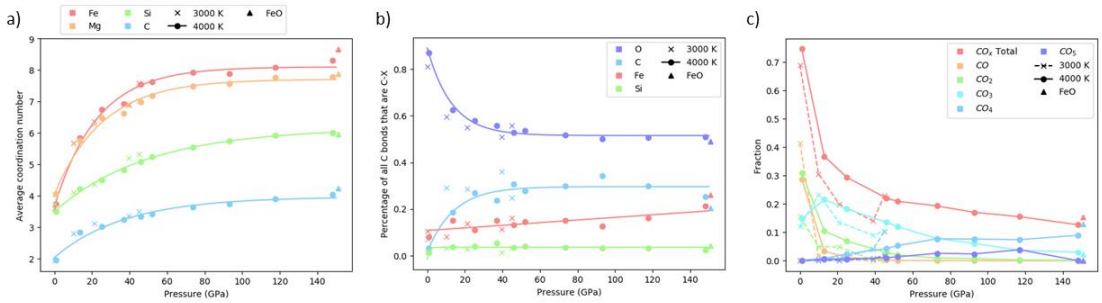

Figure 4.16: Results of simulations starting with 4 FeO units at 150 GPa and 4,000 K. a) Average cation coordination states as a function of pressure and temperature. Oxidized iron does not significantly change the average coordination state of cations. b) Carbon bond abundances as a function of pressure. The addition of oxidized iron slightly increases the fraction of C-Fe bonds and slightly lowers the fraction of C-C bonds. c) Abundances of carbonate species as a function of pressure and temperature. The addition of oxidized iron slightly increases the abundance of carbonates in the melt.

density to separate individual atoms from the melt structure and determine the total electronic charge of each atom. Bader charges were integrated using the Bader charge analysis algorithm (Henkelman et al., 2006; Sanville et al., 2007; Tang et al., 2009; Yu & Trinkle, 2011). Oxidation states of all five elements were found. Oxygen, silicon, and magnesium are essentially invariant with pressure, with average oxidation states of -1.4, 2.9, and 1.6, respectively. Due to redox exchange between iron and carbon, iron and carbon have oxidation states that vary with pressure (Figure 4.17a and Table B.24). With increasing pressure, carbon is reduced by iron. Iron's average oxidation state rises from 1.0 at 1 GPa to 1.2 at 73 GPa while carbon's average oxidation state falls from 1.1 at 1 GPa to 0.8 at 73 GPa. This change in oxidation state is evidenced not only by carbon's predilection to form reduced C-C and C-Fe species, but also by the overall decrease in carbonate groups (Figure 4.9a). Carbonate stability is particularly sensitive to the redox conditions of the system, and carbonates are typically only stable in oxidizing environments (Stagno et al., 2015; Stagno et al., 2011). Finally, we examined how the addition

of four FeO units affects the oxidation states of iron and carbon. The oxidation state of carbon increases with increasing oxygen fugacity. Carbon's oxidation state rises from 0.7 in the reduced composition to 0.9 in the oxidized composition, and iron's oxidation state falls from 1.2 in the reduced composition to 1.1 in the oxidized composition. Thus, the oxidation states of carbon and iron are dependent on the redox conditions of the system, and this dependency is manifested in the speciation results (Figure 4.6b). Figure 4.17a plots the oxidation states of carbon and iron averaged across all carbon and iron atoms. However, each individual atom has an oxidation state that is dependent on its bonding environment. Figure 4.17b examines the oxidation states of individual carbon atoms as a function of the fraction of bonds it forms that are C-O bonds (see also Tables B.25-B.28). Generally, oxidation states are higher for carbon atoms with more carbon-oxygen bonds. This trend is linear, and the trend lines at 73, 148 GPa, and 150 GPa (FeO

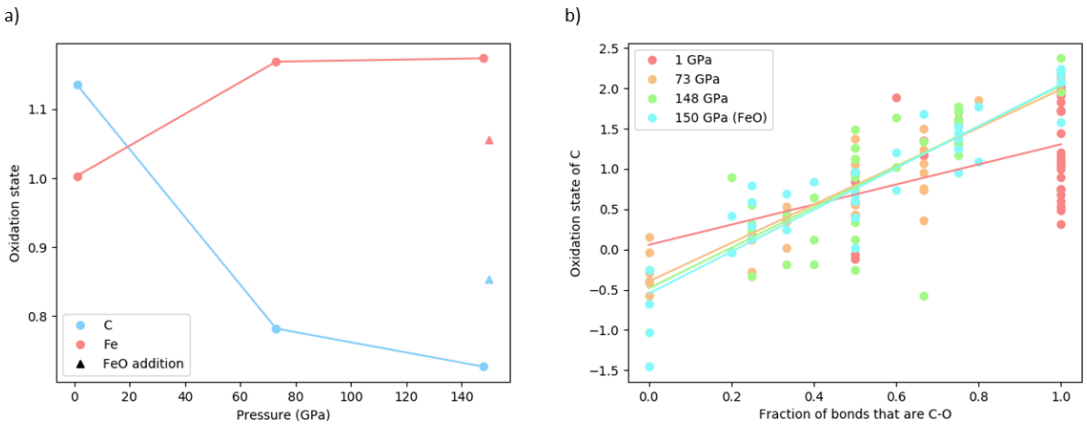

Figure 4.17: a) Average oxidation states of carbon and iron as a function of pressure. With increasing pressure, carbon becomes more reduced and iron becomes more oxidized. The addition of four FeO units (triangles) reduces iron and oxidizes carbon relative to the non-oxidized simulation. b) Oxidation states of individual carbon atoms as a function of fraction of bonds that are C-O bonds. Oxidation states of carbon increase linearly with increasing fraction of C-O bonds.

simulation) are in good agreement. At 1 GPa, there is more scatter in the data, due to the abundance of molecular CO and CO_2 groups. With increasing pressure, the abundance of carbon-oxygen bonds decreases and the abundance of carbon bonds to other elements increases (Figure 4.6a). Therefore, within melts of similar composition at increasing depth in the Earth, carbon oxidation states generally shift to the left side of the plot in Figure 4.17b, down the trendline, to yield lower average carbon oxidation states and more reduced carbon overall.

4.3.5 Diffusivities

The diffusion coefficients of all elements are plotted at 3,000 K in Figure 4.18a (see also Table B.29) and at 4,000 K in Figure 4.18b (see also Table B.30). Diffusion coefficients increase with increasing temperature and decrease with increasing pressure, as expected. The diffusivity of an individual element is an indication of its role in the melt. Less mobile elements tend to be network formers, while more mobile elements tend to be network modifiers. Generally, silicon is the least mobile element, followed by carbon, magnesium, oxygen, and iron. Silicon and carbon are network formers, while iron is a network modifier. Carbon's relative diffusivity compared to the other elements changes with pressure. At 1 GPa, carbon is the most mobile element, as it is mostly in molecular species. From 13 to 97 GPa, carbon is the second least mobile element, and from 97 to 148, carbon's diffusivity rises relative to the other elements, indicating its changing role in the melt network. Comparing this study to other carbon-bearing silicate compositions, we find similar results. At 3,000 K, this study is in good agreement with CO_2-bearing olivine melt (Solomatova et al., 2020). At 4,000 K, we find that carbon is less mobile in this study than in CO-bearing pyrolite (Solomatova et al., 2019), and similar to CO_2-bearing $MgSiO_3$ (Ghosh & Karki, 2017). The difference between this work and Solomatova et al. (2019) can be explained

by the degree of carbon polymerization in the melt. In this work, carbon forms large clusters, which are less mobile. Based on this reasoning, we would expect a melt of this composition to be more viscous than a CO-bearing pyrolite melt. However, when comparing carbon-bearing melts to a pure $MgSiO_3$ melt (Karki et al., 2009), all cations are more mobile, indicating that carbon-bearing melts are less viscous than their carbon-free counterparts. As incorporation of volatile species into silicate melts has been shown to lower viscosity (Ghosh & Karki, 2017), this result is expected.

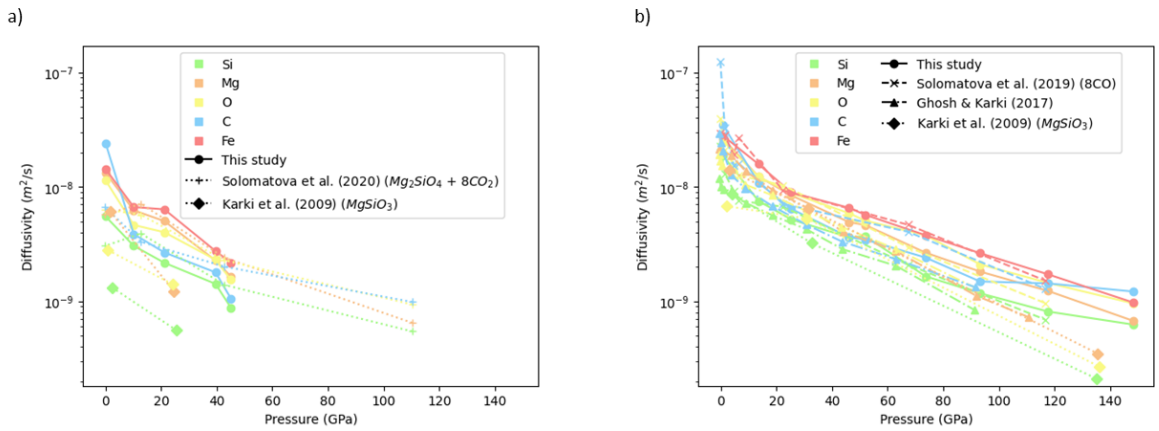

Figure 4.18: Diffusivities of silicon, magnesium, oxygen, carbon, and iron at a) 3,000 K and b) 4,000 K as a function of pressure. Values from this study (solid line, circles) are compared to Solomatova et al. (2020) (dotted line, plusses), Solomatova et al. (2019) (dashed line, x's), and Ghosh and Karki (2017) (dashed dotted line, triangles). Diffusivities increase with temperature and decrease with pressure.

The diffusivity of an element can be used as a proxy for the homogeneity of the melt. Melts with high diffusivities are more likely to be well mixed. By transforming the carbon diffusion coefficients at 4,000 K into length scales, we can estimate the distance carbon atoms will travel in 1 million years. At 0 GPa, carbon atoms travel 1042 m, 1912 m, and 879 m in the carbonatitic, pyrolitic, and CO_2-bearing $MgSiO_3$ melts, respectively. These numbers indicate that

carbonatite melts are less homogenous than carbon-bearing pyrolite melts, and similarly homogenous compared to CO_2-bearing $MgSiO_3$. At 136 GPa, the estimated distances drop significantly, with carbon atoms travelling 202 m, 202 m, and 98 m in the carbonatitic, pyrolitic, and CO_2-bearing $MgSiO_3$ melts, respectively. At core-mantle boundary pressures, the carbonatitic and pyrolitic melts are expected to be similarly homogenous, while the CO_2-bearing $MgSiO_3$ melt is expected to be less so. We would anticipate that all melts are less well-mixed at higher pressures, due to the decrease in diffusivity with pressure.

4.3.6 Electronic structure of the melt

With a significant iron component in our melt (~10 atomic % Fe), we examine the electronic density of states (DOS) to investigate conductivity behavior in the melt. Figure 4.19 plots the density of states at 1, 73, and 148 GPa and 4,000 K. The melt is conducting at all

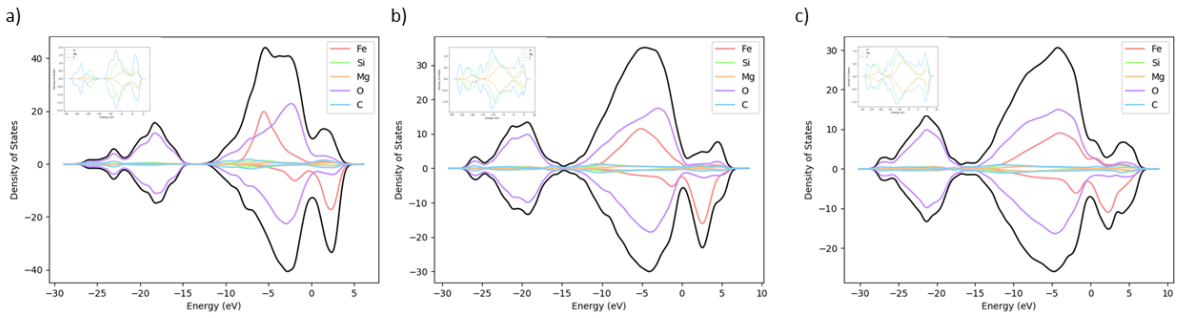

Figure 4.19: Density of states at a) 1 GPa, b) 73 GPa and c) 148 GPa and 4,000 K. The total DOS is plotted in black, and individual element components are plotted according to the legend. The inset (top left) zooms in on the silicon, magnesium, and carbon components for clarity. Positive DOS values are contributions from spin up electrons, and negative values are contributions from spin down electrons. At all studied pressures, electrons have energy above the Fermi level (0 eV in the plot), indicating a conducting liquid.

pressures examined, even 1 GPa, due primarily to the high iron content. With increasing pressure, the occupancy of the Fermi level increases.

The spin decomposition of the electronic density of states for all the elements, except for iron, show a clear complete pairing of electrons. There is equal contribution from the spin up and the spin down electrons. Iron, however, is asymmetric at all pressures examined. The uneven occupation of energy levels between spin up and spin down electrons indicates that the iron atoms preserve a local remnant magnetic moment in the melt. The value of the local magnetization is largest at 1 GPa, where the iron curves have the most asymmetry. With increasing pressure, the asymmetry decreases, and iron becomes less spin polarized, although some magnetization is still apparent even at 148 GPa.

The spin state of iron has important implications for the physical properties of melts and minerals. Spin transitions from high-spin to low-spin states in iron-bearing mantle compositions lead to densification at high pressures (Karki et al., 2018; Liu et al., 2020; McCammon et al., 2013; Speziale et al., 2005). Local spin state affects iron coordination and bond length in melts, with high-spin iron atoms being more highly coordinated with longer bonds (Ghosh & Karki, 2020). Additionally, the spin state of iron is known to affect the partitioning behavior of iron between solids and silicate melts (Maeda et al., 2017; Prescher et al., 2014). Previous work on iron spin states in melts and glasses disagrees on whether or not a spin transition occurs, and the completeness of that transition. Mossbauer and X-ray emission studies of silicate glasses find no evidence of a spin transition below 84 GPa (Lee, 2014; Mao et al., 2014; Prescher et al., 2014). However, higher pressure Mossbauer, X-ray emission, and nuclear forward scattering studies (up to 135 GPa) of silicate glasses indicate that a broad, partial spin transition may occur at higher

pressures (Gu et al., 2012; Maeda et al., 2017). Using *ab initio* molecular dynamics, Karki et al. (2018) finds that a spin transition occurs gradually beginning around 100 GPa in silicate melts. In our work, the local magnetization on the iron atoms flips more often between spin up and spin down with increasing pressure. At 93 GPa, the magnetization begins to flip between positive and negative values, suggesting the onset of a gradual spin transition. Our prediction that a spin transition initiates at about 93 GPa agrees with experimental measurements of a spin transition

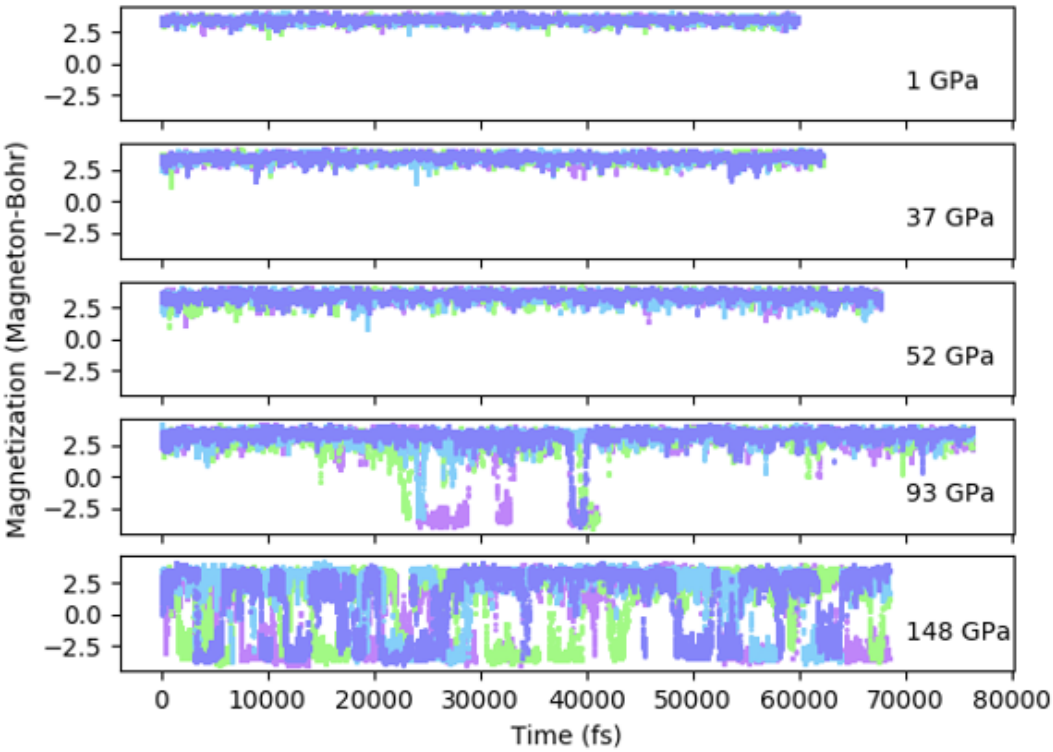

Figure 4.20: Magnetic moments of four iron atoms versus time across different pressures. With increasing pressure, the local magnetic moments of iron begin to flip, indicating a net loss in magnetism in the melt.

beginning at roughly 100 GPa. At higher pressures the flipping exhibits transient non-magnetized states that last for a few femtoseconds (Figure 4.20).

4.4 Conclusions

These simulations of a carbonate-silicate-metal melt highlight the important effect of high carbon content, which greatly affects the chemical and physical properties of the melt. Coordination numbers increase continuously with pressure, leading to unusual coexisting coordination environments. Coordination distributions broaden around non-preferred coordination states and with increasing temperature. Coordination states are long-lived at low pressure, and short-lived at high pressure, indicating the changing nature of the melt network with pressure. Silicon and carbon have the longest-lived coordination states, indicating their role as network formers. Bond lengths in the melt generally decrease with pressure, although increases are also observed when associated with coordination changes in the cations. Diffusion coefficients decrease with pressure and increase with temperature. Silicon and carbon generally have the lowest diffusivities, indicating that they are network formers. This volatile-bearing melt has a lower viscosity than pure silicate melts (Karki et al., 2009). Melts are conducting at all pressures, and iron has some magnetization, which diminishes with pressure.

Speciation is complicated, and many unusual species are present. The complicated nature of the melt stems largely from carbon's ability to behave as both a cation and an anion. Carbon forms bonds to all elements but magnesium, and begins to replace oxygen in the melt network with increasing pressure. Carbon bonding is highly dependent on both pressure and oxygen fugacity. With increasing pressure, C-O bonding becomes less dominant and is compensated by increases in C-C and C-Fe bonding. Additionally, C and Fe undergo redox exchange, and carbon oxidizes iron to become more reduced. As a result, carbon-carbon and carbon-iron clusters grow, and carbonate abundance decreases. In a more oxidized system, carbon reduces iron, forming

more oxidized species overall. Compared to previous work (Karki et al., 2020; Solomatova et al., 2019), our system has greater C-C bond abundances, indicating a propensity for carbon to bond with itself in carbon-rich melts at the expense of other types of bonding. Carbonatitic melts may be a parent melt for diamond formation or, coupled with the increasingly siderophile nature of carbon with increased pressure, for a dense C-Fe liquid.

CHAPTER 5

DENSITIES AND MISCIBILITIES OF CARBONATE-SILICATE-METAL MELTS

5.1 Introduction

Carbon plays a vital role at Earth's surface in biological and atmospheric processes, but the role of carbon in the deep Earth is less well understood. Carbon and other volatiles in the lower mantle are thought to be either remnants of an early magma ocean (Labrosse et al., 2007) or to derive from subducting slabs (Plank and Manning, 2019). However, reports vary on the carbon content of the Earth (Javoy, 1997; McDonough and Sun, 1995), the distribution of carbon between core and mantle (Dasgupta and Walker, 2008; Wood et al., 2013), the phase relations of carbon-bearing phases at depth (Merlini et al., 2012; Oganov et al., 2008), and the reactivity of carbon-bearing phases with the surrounding core and mantle. The existence and role of carbonates in particular in the lower mantle is highly contested. Multiple studies show that carbonates undergo melting (Li et al., 2017b), reduce to diamond or iron carbide (Rohrbach and Schmidt, 2011), or decarbonate (Drewitt et al., 2019) before they reach the lower mantle in subducting slabs. However, the stability of carbonate phases depends on a host of thermodynamic variables, including pressure, temperature, and oxygen fugacity. Reports of carbonate melt inclusions in deep Earth diamonds (Korsakov and Hermann, 2006) as well as petrologic experiments on solid carbonates in lower mantle phase assemblages (Dorfman et al, 2018; Lv et al., 2021) indicate that carbonates and carbonate melts may be stable and present in the lower mantle. However, few studies have examined carbonate melt interactions in the lower mantle.

Previous *ab initio* studies have examined carbonate melts (Koura et al., 1996; Li et al., 2017b; Xu et al., 2020), carbon-bearing silicate melts (Bajgain and Mookherjee, 2021; Ghosh et al., 2017; Ghosh and Karki, 2017; Ghosh et al., 2007), carbon and iron-bearing silicate melts (Karki et al., 2020; Solomatova et al., 2020; Solomatova and Caracas, 2021; Solomatova et al., 2019), and carbon partitioning between silicate and iron melts (Zhang and Yin, 2012). This work and the study in Chapter 4 represent the first *ab initio* studies with subequal amounts of carbon, silicon, and metal melt. In this study, we examine ternary melt mixtures of carbonate-silicate-metal melts. We simulate seven total endmember, binary, and ternary melt compositions (see Table 5.1) at pressures between 0-200 GPa and 4,000 K. We use the results of our simulations to evaluate melt densities, Gibbs free energies of mixing, and chemical speciation to understand the gravitational stability of melt compositions in the lower mantle, the miscibilities of binary and ternary melt mixtures, and the types of chemical species that exsolve from immiscible melt

Melt	Mg	Si	C	O	Fe	Total
$MgCO_3$	24	0	24	72	0	120
$MgSiO_3$	24	24	0	72	0	120
Fe	0	0	0	0	108	108
$Mg(C,Si)O_3$	24	12	12	72	0	120
$MgCO_3$ + Fe	24	0	24	72	13	133
$MgSiO_3$ + Fe	24	24	0	72	13	133
$Mg(C,Si)O_3$ + Fe	24	12	12	72	13	133

Table 5.1: Melt compositions used in this study. The numbers refer to the number of atoms included in the simulation.

compositions. From our results, we evaluate the implications of mixed carbonate-silicate-metal melt compositions for carbon sequestration and distribution throughout Earth's mantle and core.

5.2 Methods

Ab initio molecular dynamics simulations using the projector-augmented wave method (Kresse and Furthmuller, 1996) of density functional theory were performed with the Vienna *ab initio* simulation package (Blochl, 1994). We used the generalized gradient approximation in the Perdew-Burke-Ernzerhof form (Perdew et al., 1996) to treat electron exchange and correlation. The kinetic energy cutoffs for the plane-wave expansion of the wavefunctions were set to 600 eV. We used the canonical ensemble (NVT) with a Nosé-Hoover thermostat (Hoover, 1985; Nosé, 1984) with a time step of 1-2 fs for 18-80 ps, depending on the density. The Brillouin zone was sampled at the gamma point. The calculations were spin-polarized at all pressures. The mean-square displacement as a function of time shows a ballistic regime below approximately 1,000 fs, after which the atoms reach a diffusive regime. For the carbonate-silicate-metal melt composition, calculations were run with a minimum of two starting configurations, and results were averaged.

We work with seven melts to represent endmember ($MgCO_3$, $MgSiO_3$, and Fe), binary ($Mg(C,Si)O_3$, $MgCO_3$ + Fe, $MgSiO_3$ + Fe), and ternary ($Mg(C,Si)O_3$ + Fe) melt compositions (see Table 5.1), with supercells ranging from 108-133 atoms. Simulations span a pressure range of 0-200 GPa and all calculations are performed at 4,000 K. Bond distances were determined from the pair distribution functions. The first peak in the pair distribution function marks the radius of the first coordination sphere for the reference atom, and the first minimum translates to

the maximum acceptable bond distance for a bonding pair. The fitted minimum values were used in the speciation analysis to determine carbon clusters.

5.3 Results

5.3.1 Equations of state

Pressure-density relationships for simulated melts are plotted in Figure 5.1 (see also Tables C.1-C.7). Iron melt is the densest and $MgCO_3$ melt is the least dense, as expected. $MgSiO_3$ melt closely matches the behavior of pyrolite melt ($NaCa_2Fe_4Mg_{30}Al_3Si_{24}O_{89}$; Solomatova and Caracas, 2021; Solomatova et al., 2019), indicating its usefulness as a representative mantle composition. Pressure-density relationships are fit to third order Birch-

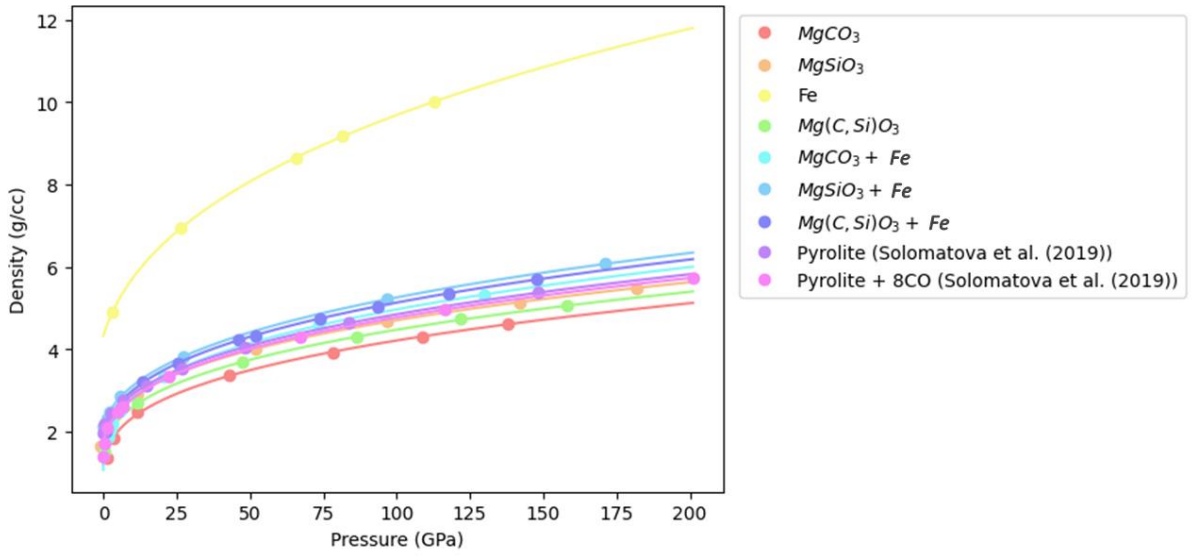

Figure 5.1: Densities of simulated melt compositions from this study and from Solomatova et al. (2019). Melts with more volatile species are less dense and melts with a metal component are denser. Data are fit to third-order Birch-Murnaghan equations of state.

Murnaghan equations of state for all melts except $MgCO_3$ + Fe, whose fit required only a second order Birch-Murnaghan equation. The third order Birch-Murnaghan equation is given by:

$$P(V) = \frac{3K_0}{2}\left[\left(\frac{V_0}{V}\right)^{\frac{7}{3}} - \left(\frac{V_0}{V}\right)^{\frac{5}{3}}\right]\left\{1 + \frac{3}{4}(K_0' - 4)\left[\left(\frac{V_0}{V}\right)^{\frac{2}{3}} - 1\right]\right\} \quad (5.1)$$

where P is the pressure, V is the volume, K_0 is the bulk modulus, V_0 is the zero pressure volume, and K_0' is the pressure derivative of the bulk modulus. Fit parameters are given in Table 5.2. Melts with a carbonate component are highly compressible, in line with previous reports on the effect of carbon on a melt's compressibility behavior (Ghosh et al., 2017; Ghosh et al., 2007; Sakamaki et al., 2011). There is a large tradeoff between K_0', K_0, and V_0 values for all melts, due to the fact that one continuous equation of state was fit across multiple structural transitions,

Melt	K_0 (GPa)	V_0 (Å^3)	K_0'
$MgCO_3$	2 (3)	2.8 (8) x 10^3	6 (2)
$MgSiO_3$	10 (2)	2.03 (7) x 10^3	5.9 (3)
Fe	19 (2)	2.32 (5) x 10^3	4.6 (1)
$Mg(C,Si)O_3$	5 (4)	2.3 (3) x 10^3	5.8 (9)
$MgCO_3$ + Fe	20 (5)	2.2 (2) x 10^3	4†
$MgSiO_3$ + Fe	11 (1)	2.40 (4) x 10^3	5.3 (1)
$Mg(C,Si)O_3$ + Fe	6 (3)	2.6 (2) x 10^3	5.9 (5)
Pyrolite[1]	12 (1)	1.83 (3) x 10^3	5.4 (1)
Pyrolite + 8CO[1]	5 (1)	2.36 (7) x 10^3	6.2 (3)

[1]From Solomatova et al. (2019)
[†]Held fixed

Table 5.2: Birch-Murnaghan equation of state fit parameters for simulated melt compositions.

which stem from coordination changes in the melt. However, the majority of coordination changes occur in the first 20 GPa (see Figure 4.12a), and above 20 GPa, the fits closely match the data.

Densities of liquids calculated from molecular dynamics (MD) methods have been shown to systematically deviate from experimental values depending on the approximation used for the exchange correlation functional (Zhang et al., 2013; Zhao et al., 2014) (see also section 3.2). However, melts calculated with the same methods allow for relative comparisons of density to be made. $MgCO_3$ and $Mg(C,Si)O_3$ melts are both less dense than $MgSiO_3$ and pyrolite melts, indicating that these melts would be buoyant in the mantle. $MgCO_3$ + Fe, $MgSiO_3$ + Fe, and $Mg(C,Si)O_3$ + Fe melts are denser than both $MgSiO_3$ and pyrolite melts and less dense than Fe melt, indicating that these melt compositions would sink in the mantle, and would be buoyantly stable at the core-mantle boundary.

5.3.2 Melt miscibilities

From our density calculations, we determine miscibilities of multicomponent melts by calculating the Gibbs free energy of mixing, ΔG_{mix}. ΔG_{mix} is calculated using the following equation:

$$\Delta G_{mix} = \Delta H_{mix} - T\Delta S_{mix} + \int P\Delta V_{mix} \quad (5.2)$$

where ΔH_{mix} is the enthalpy of mixing, T is the temperature, ΔS_{mix} is the entropy of mixing, P is the pressure, and ΔV_{mix} is the mixing volume. ΔH_{mix} is calculated at a reference condition, and we assume a regular symmetric form. We also assume ΔS_{mix} is ideal and therefore, fixed in pressure and temperature. ΔV_{mix} is a function of pressure and thus, its contribution to ΔG_{mix} is

found by integrating over pressure. Negative ΔG_{mix} values indicate a mixture is energetically favorable, and therefore miscible. We describe the calculation of each term in the equation in the following sections.

5.3.2.1 Mixing volumes

Using the Birch-Murnaghan equation of state fits, we calculate the molar volumes of the melts at pressures from 0 to 200 GPa (Figure 5.2, Tables C.1-C.7). Due to the non-stoichiometric nature of the melt mixtures, we calculate volumes per mole of atoms instead of per formula unit, allowing the melt volumes to be directly compared. Iron and iron-bearing melts have the largest molar volumes, while pyrolite melts have the smallest.

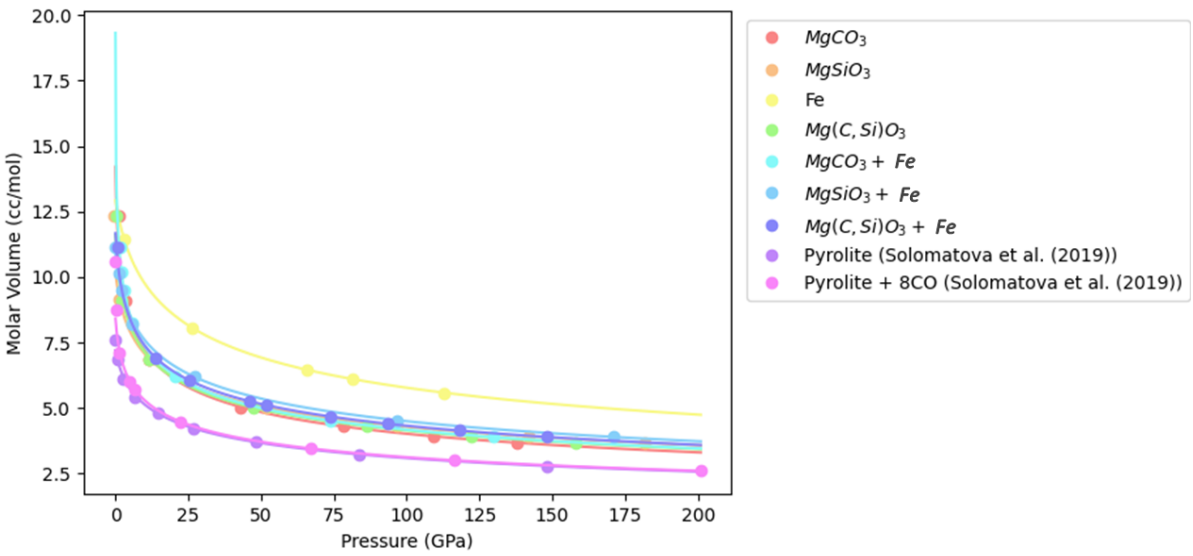

Figure 5.2: Molar volumes of simulated melts as a function of pressure. Due to the non-stoichiometric nature of the ternary melt composition, we report volumes for all melt compositions per mole of atoms for comparison purposes.

From the molar volumes of the melt, mixing volumes are calculated. To calculate mixing volumes, we compare the molar volume of our simulated mixtures with the sum of the molar volumes of the mixture components. The magnitude of the mixing volume indicates the nonideality of a melt mixture and represents the degree and nature of interaction between melt components. The mixing volume is the pressure derivative of ΔG_{mix}, and as such, is the tendency of a mixture to become more or less energetically favorable with pressure. Thus, the signs of the mixing volumes are suggestive of miscibility in multicomponent mixtures. This is especially true

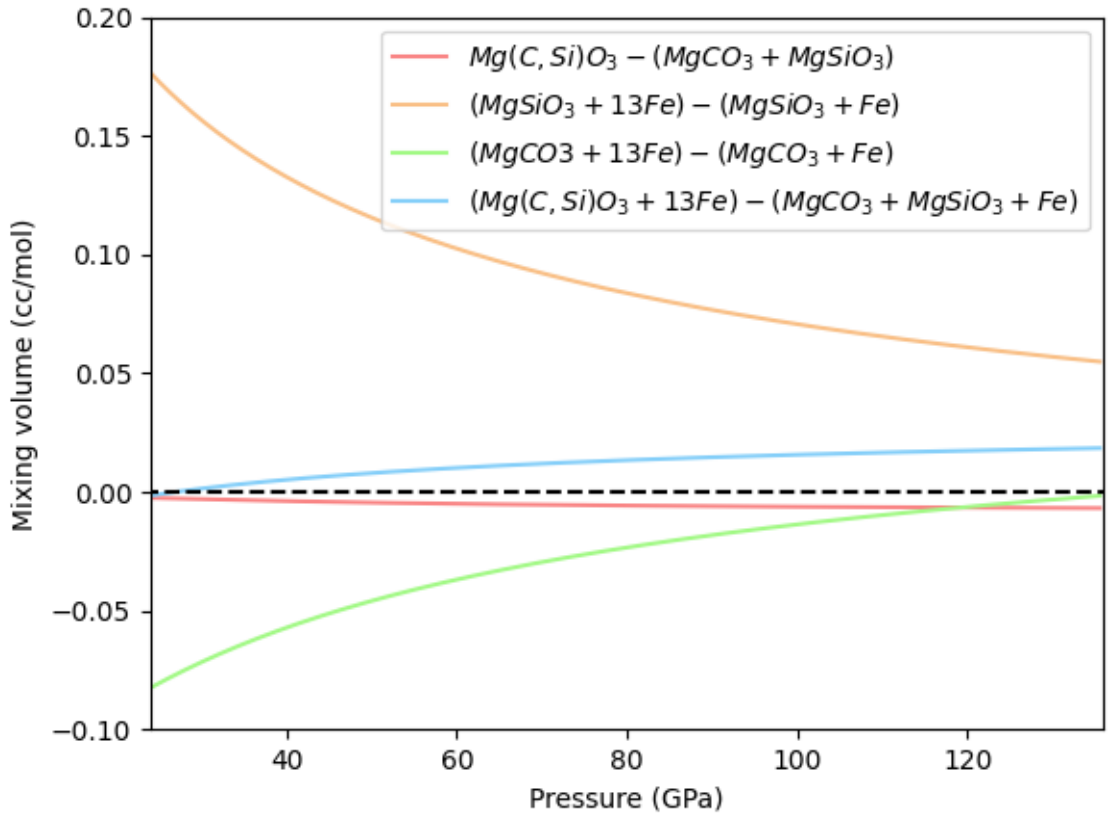

Figure 5.3: Mixing volumes as a function of pressure for simulated binary and ternary melts. Our carbonate-silicate and carbonate-iron melts have negative mixing volumes over the entire range of the lower mantle. The silicate-metal and carbonate-silicate-metal melts have positive mixing volumes through the entire lower mantle.

at high pressures, where we observe that the mixing volume term of ΔG_{mix} ($P\Delta V_{mix}$) dominates the contribution to ΔG_{mix} and thus, dictates the miscibility. Mixtures with positive mixing volumes become larger upon mixing and would become immiscible with increasing pressure. Mixtures with negative mixing volumes become smaller upon mixing and would become miscible at high pressures. The mixing volumes for the four multicomponent melts in this study are plotted as a function of pressure in Figure 5.3. Over the range of the lower mantle, $Mg(C,Si)O_3$ and $MgCO_3$ + Fe have negative mixing volumes, suggesting these melts are miscible, while $MgSiO_3$ + Fe and $Mg(C,Si)O_3$ + Fe have positive mixing volumes, suggesting these melts are immiscible.

In order to determine mixing volumes for any composition in the $MgCO_3$-$MgSiO_3$-Fe ternary system, the mixing volume data is fit to the following power series multicomponent mixing model (Ganguly, 2001; Wohl, 1946, 1953):

$$\Delta V_{mix} = \sum_{i \neq j} X_i X_j (W_{ij}^G X_{ji} + W_{ji}^G X_{ij}) + \sum_{i \neq j, \neq k} X_i X_j X_k C_{ijk} \qquad (5.3)$$

where ΔV_{mix} is the mixing volume, the W^G's are the binary interaction parameters, and C_{ijk} is the ternary interaction term. X_i, X_j, and X_k are the mole fractions of the i, j, and k components, and X_{ji} and X_{ij} are the projected mole fractions of the i and j components in the binary join i-j. X_{ij} is given analytically by $\frac{1}{2}(1+X_i-X_j)$. Similar to our calculation of molar volumes, in this analysis, we set the mole fractions by counting the number of atoms of each component, rather than the number of formula units. Thus, each iron atom in the model is essentially compared to an average atom of either an $MgCO_3$ or an $MgSiO_3$ unit. In this model, we assume that mixing along the binaries is symmetric, and thus $W^G_{ij} = W^G_{ji}$. From the model fits, we evaluate how mixing

volumes change along binary and ternary compositions. Mixing volumes and binary/ternary interaction parameters at specific lower mantle pressures are reported in Table 5.3.

Melt	Pressure (GPa)	Mixing parameter	Mixing volume (cc/mol)
$Mg(C,Si)O_3$	24	-0.01	-0.003
	50	-0.02	-0.005
	136	-0.03	-0.007
$MgCO_3$ + Fe	24	-0.94	-0.08
	50	-0.52	-0.05
	136	-0.02	-0.002
$MgSiO_3$ + Fe	24	2.00	0.18
	50	1.31	0.12
	136	0.62	0.05
$Mg(C,Si)O_3$ + Fe	24	-1.14	-0.002
	50	-0.66	0.008
	136	-0.13	0.018

Table 5.3: Binary/Ternary mixing parameters and calculated mixing volumes for binary and ternary melt mixtures at 24, 50, and 136 GPa for Figure 5.4.

Figure 5.4a-c displays mixing volumes along the binary joins $MgCO_3$-$MgSiO_3$, $MgCO_3$-Fe, and $MgSiO_3$-Fe at 24 GPa, 50 GPa, and 136 GPa, calculated using the fit parameters in Table 5.3. Mixing volumes are negative at all lower mantle conditions along the carbonate-silicate join, and mixing volumes become more negative with increasing pressure. Mixing volumes along the silicate-metal join also become more negative with pressure, but the mixing volumes are positive across all lower mantle pressure conditions. At higher pressures, we would expect silicate and metal melts to become miscible. Along the carbonate-metal join, mixing volumes are always negative, but mixing volumes become more positive with increasing pressure. The negative mixing volumes promote mixing within mantle pressures, but carbonate-metal melts will become

immiscible at pressures well above the core-mantle boundary pressure. Additionally, the magnitude of the mixing volumes represents the degree of interaction between the melts. Generally, silicate-metal melts have the most interaction, followed by carbonate-metal melts, and carbonate-silicate melts. Carbonate-silicate melt interaction terms are very small, even at their most negative at 136 GPa, indicating that this mixture is close to ideal.

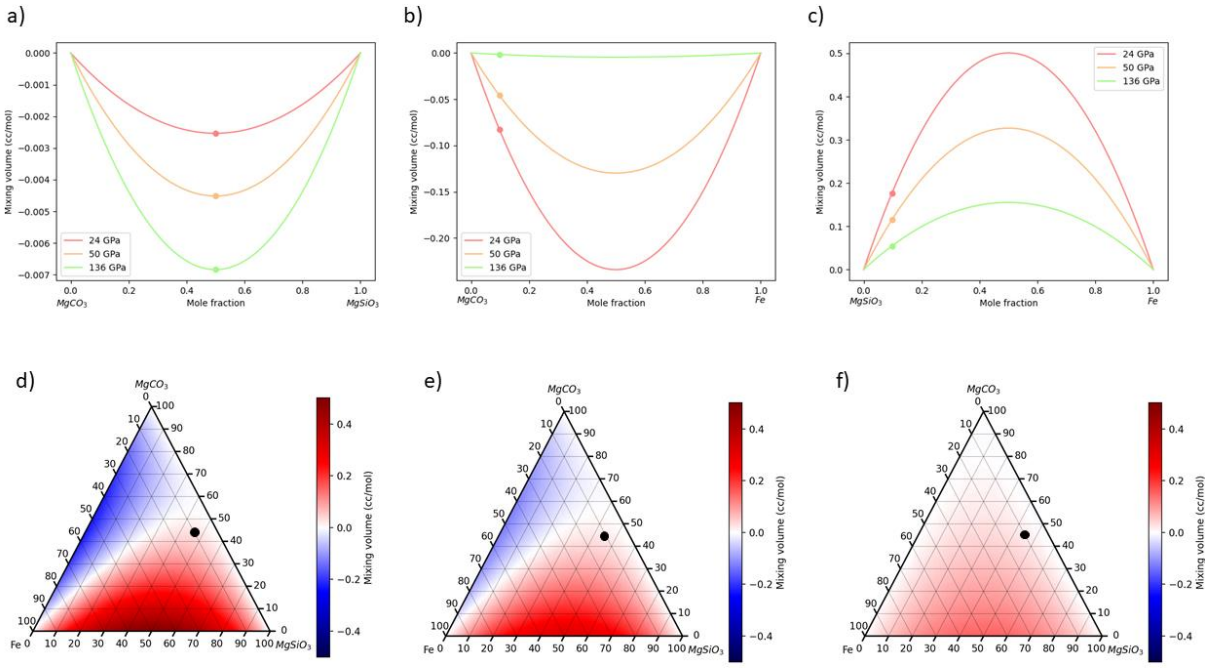

Figure 5.4: a-c) Mixing volumes for binary solutions of a) $MgCO_3$ and $MgSiO_3$; b) $MgCO_3$ and Fe; and c) $MgSiO_3$ and Fe at 24 GPa (red line), 50 GPa (orange line), and 136 GPa (green line). Simulated compositions are marked by data points, and lines are fits to the multicomponent mixing model. Both the $MgCO_3$ and $MgSiO_3$ binary and the $MgCO_3$ and Fe binary have negative mixing volumes at lower mantle pressures, indicating miscibility. The $MgSiO_3$ and Fe binary has positive mixing volumes across all lower mantle pressures, suggesting immiscibility. d-f) Mixing volumes for ternary solutions of $MgCO_3$, $MgSiO_3$, and Fe at d) 24 GPa; e) 50 GPa; and f) 136 GPa. Positive mixing volumes are shaded red and negative mixing volumes are shaded blue. The simulation composition used to fit the mixing model is marked by the data point, and always lies within the immiscible region of the plot.

Calculated mixing volumes for ternary compositions are also shown in Figure 5.4d-f (see also Table 5.3). At 24 GPa, melts with a greater than 50% carbonate component have negative mixing volumes. Below 50% carbonate percentage, mixing volumes are more negative with increasing iron percentage and more positive with increasing silicate percentage. With increasing pressure, the negative mixing volume regime shrinks and the positive mixing volume regime grows to cover more iron and carbonate-rich parts of the ternary plot. By 136 GPa, only compositions with greater than 70% carbonate and compositions close to the carbonate-metal and carbonate-silicate binaries have negative mixing volumes. Additionally, mixing volume

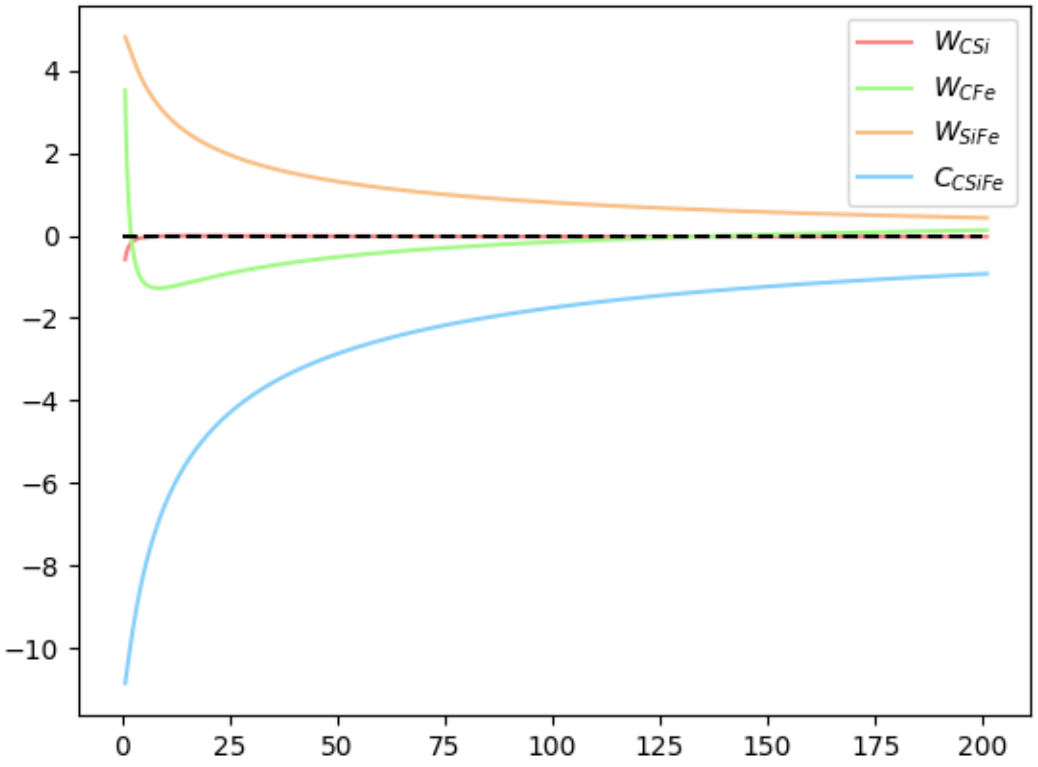

Figure 5.5: Binary and ternary interaction terms for the power series multicomponent model. The ternary interaction term has the largest magnitude, indicating the largest deviation from an ideal solution.

magnitudes decrease with increasing pressure, indicating that melts tend to become more ideal mixtures with increasing pressure. This conclusion is supported by the trends of the binary and ternary interaction parameters (Figure 5.5 and Table 5.3). With increasing pressure, the interaction parameters trend towards 0, indicating that the interaction between melt components becomes increasingly less important with depth.

5.3.2.2 Entropy of mixing

To calculate the entropy of mixing, we use the ideal entropy of mixing equation:

$$\Delta S_{mix} = -R(X_i lnX_i + X_j lnX_j + X_k lnX_k) \quad (5.4)$$

where R is the gas constant and X_i, X_j, and X_k are the mole fractions of the i, j, and k components, respectively. An example of $-T\Delta S_{mix}$ on the carbonate-silicate binary and its contribution to ΔG_{mix} is plotted in Figure 5.6.

5.3.2.3 Enthalpy of mixing

To calculate the enthalpy of mixing, we use the equation:

$$\Delta H_{mix} = \sum_{i \neq j} \beta_{ij} X_i X_j \quad (5.5)$$

where β_{ij} represents the binary parameter along the i-j binary, and X_i and X_j represent the mole fractions of the i and j components, respectively. To find appropriate values for β, we plot ΔG_{mix} at zero pressure (so the only contributions to ΔG_{mix} are from ΔH_{mix} and ΔS_{mix}) along each binary and choose a value for β that allows for limited miscibility near the binary endmembers. ΔG_{mix} is very sensitive to the choice of binary parameter, as evidenced in Figure 5.7, where ΔG_{mix} on the carbonate-silicate binary at 0 GPa is plotted for β values ranging from 95,000 – 135,000 J. To

better inform our selection of the binary parameters, we examine solubility experiments on binary systems in addition to our own binary mixture simulation results. A study of orthopyroxene solubility in carbonate melts reports that carbonate melts contain 4 atomic percent silicate at 2 GPa and 1273 K (Kamenetsky and Yaxley, 2015). Therefore, we select a value of 95,000 J for β on the carbonate-silicate join, which leads to more silicate solubility (8 atomic percent) in carbonate melts at higher temperatures (4,000 K). Silicate-metal melts are known to be immiscible (Fichtner et al., 2021), and our simulations show grouping of silicate and metal

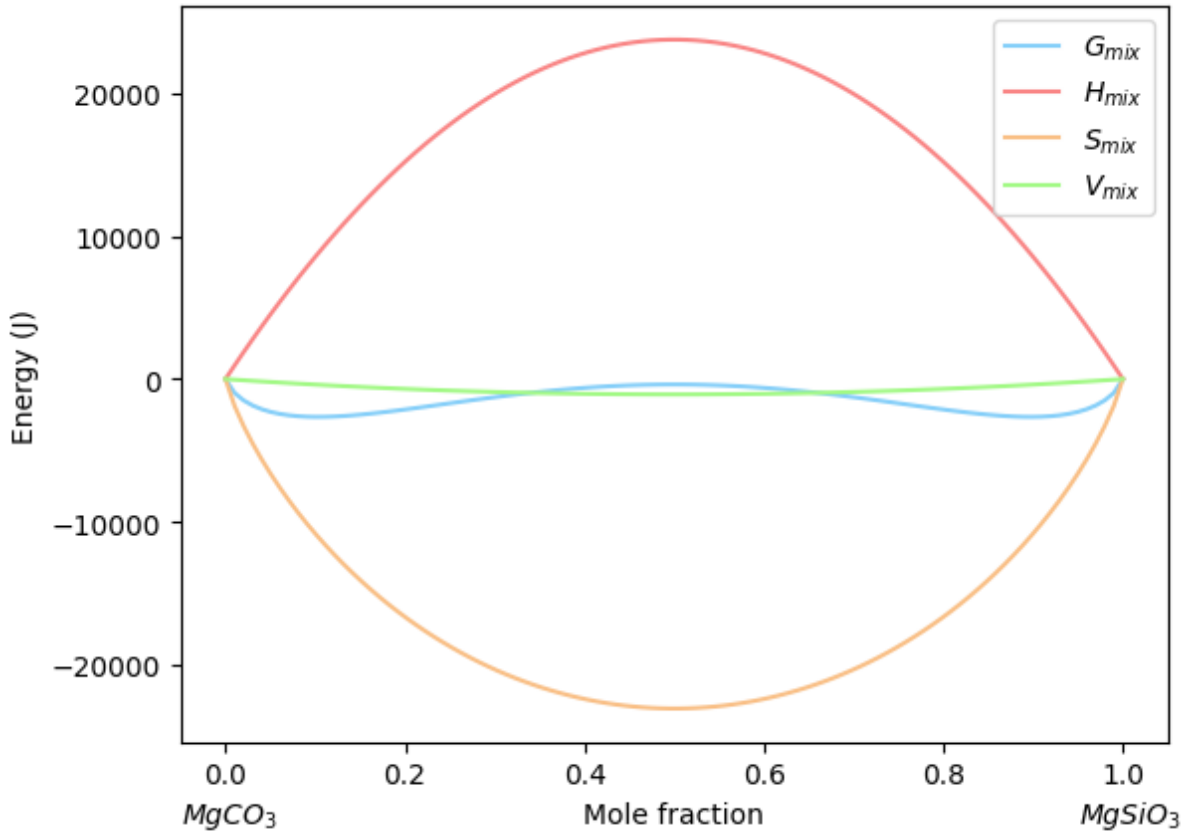

Figure 5.6: Calculated ΔG_{mix} (blue line) at 136 GPa on the $MgCO_3$-$MgSiO_3$ binary. The red line is the contribution of the ΔH_{mix} term to ΔG_{mix}. The orange line is the contribution of $-T\Delta S_{mix}$, and the green line is the contribution of $P\Delta V_{mix}$. The sum of the red, orange, and green lines yields ΔG_{mix}.

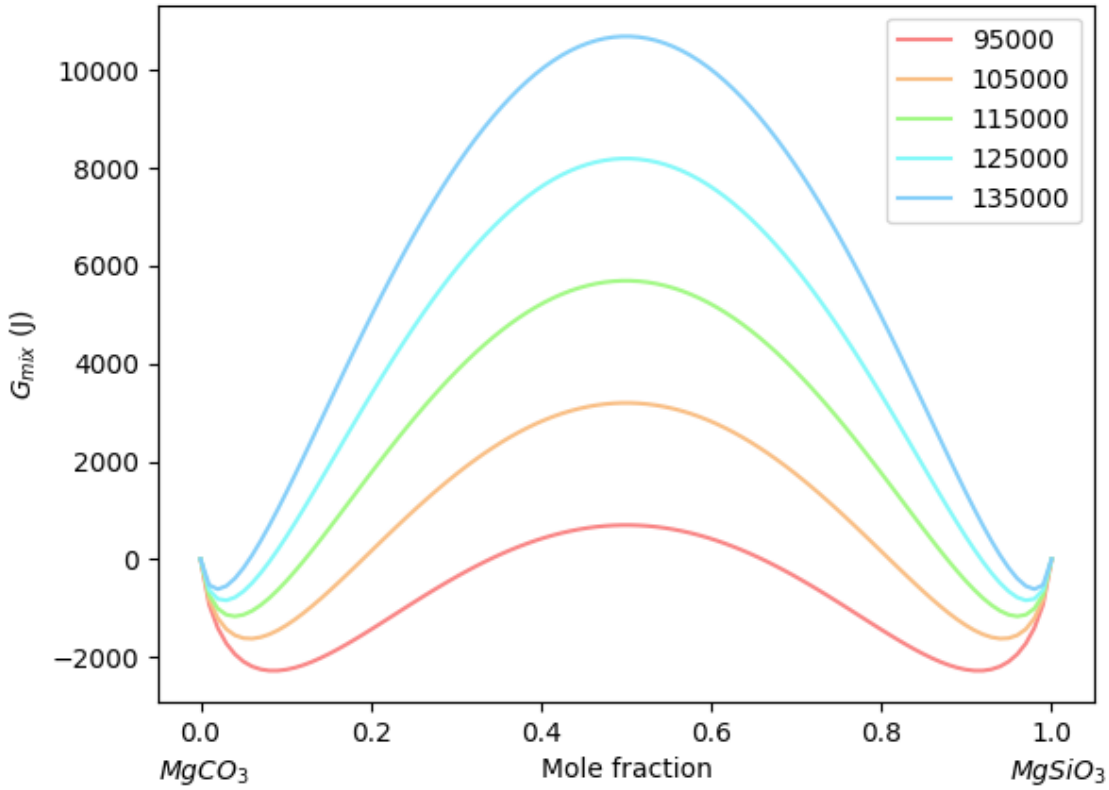

Figure 5.7: Calculated ΔG_{mix} at 0 GPa on the $MgCO_3$-$MgSiO_3$ binary for various values of β in the ΔH_{mix} term. ΔG_{mix} is very sensitive to the β value. We choose a β value of 120,000 for our calculations based on the miscibility of ternary melt compositions at low pressure.

atoms that is suggestive of immiscibility. Thus, we select a β parameter of 135,000 J, which leads to limited miscibility (2 atomic percent Fe in silicate melt) at 0 GPa and 4,000 K. Our carbonate-metal simulation shows less miscibility than the carbonate-silicate simulation and more miscibility than the silicate-metal simulation at 0 GPa. We select a value of 115,000 J for the β parameter, which leads to 4 atomic percent Fe in carbonate melt. The chosen parameters accurately describe the miscibility of the binary compositions at 0 GPa and 4,000 K. Based on the ternary mixing plot at 0 GPa (Figure 5.8), which shows limited miscibility near each of the

endmembers, we determine that there is no ternary interaction term for ΔH_{mix}. An example of ΔH_{mix} on the carbonate-silicate binary and its contribution to ΔG_{mix} is plotted in Figure 5.6.

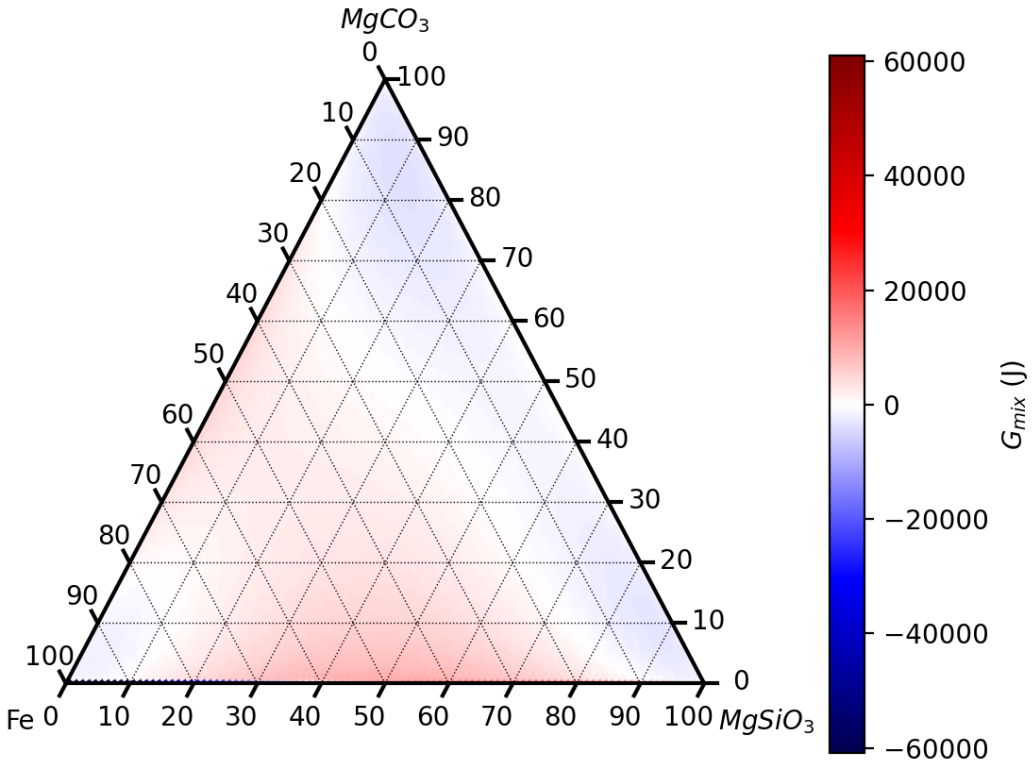

Figure 5.8: Calculated ΔG_{mix} at 0 GPa on the $MgCO_3$-$MgSiO_3$-Fe ternary. The shape of ΔG_{mix} is as expected with limited miscibility near the endmembers along each of the binaries.

5.3.2.4 Gibbs free energy of mixing

With the equations describing ΔH_{mix}, ΔS_{mix}, and ΔV_{mix}, we calculate how ΔG_{mix} evolves along binary and ternary compositions. Substituting equations 5.2, 5.3, and 5.4 into equation 5.1, we obtain:

$$\Delta G_{mix} = \sum_{i \neq j} \beta_{ij} X_i X_j - 4000 \sum_i -R(X_i ln X_i) + \int P\left(\sum_{i \neq j} X_i X_j \left(W_{ij}^G X_{ji} + W_{ij}^G X_{ij}\right) + \sum_{i \neq j, \neq k} X_i X_j X_k C_{ijk}\right) \quad (5.6)$$

ΔG_{mix} is plotted along the carbonate-silicate, carbonate-metal, and silicate-metal binaries in Figure 5.9. Because of our assumption than the enthalpy of mixing is ideal, the curves appear symmetric even though in a real system, the mixing binaries are typically asymmetric. $MgCO_3$ and $MgSiO_3$ have miscibility near the endmembers, but there is a large miscibility gap that forms at all lower mantle pressures. In the immiscible region, two melt compositions coexist, and these compositions are inferred from the minima of the ΔG_{mix} curves. The minima of the curves are plotted in Figure C.4, and are at ~9 and ~91 mole percent $MgCO_3$ at all pressures examined for the carbonate-silicate binary. ΔG_{mix} decreases with pressure, suggesting eventual closing of the miscibility gap at higher pressures than those reached by Earth's mantle. $MgCO_3$ and Fe also have a miscibility gap that begins to close with increasing pressure. At 24 GPa, the two coexisting melt compositions are at 6 and 94 mole percent $MgCO_3$, but by 136 GPa, the two coexisting melt compositions are at 38 and 62 $MgCO_3$ mole percent (Figure 5.10). $MgSiO_3$ and Fe are immiscible at all lower mantle pressures. The mixing volume component of ΔG_{mix} becomes increasingly important with pressure, illustrating the significance of calculating mixing volumes to predict mixing behavior of multicomponent melts at high pressure.

The ternary compositions (Figure 5.11) have a range of miscibilities that expand with increasing pressure. Miscible melt compositions are outlined by the solid gold lines, labelled with a 1, and are estimated from ΔG_{mix} values along each of the binaries. There are three miscibility fields, and each is located close to an endmember composition. As the carbonate-

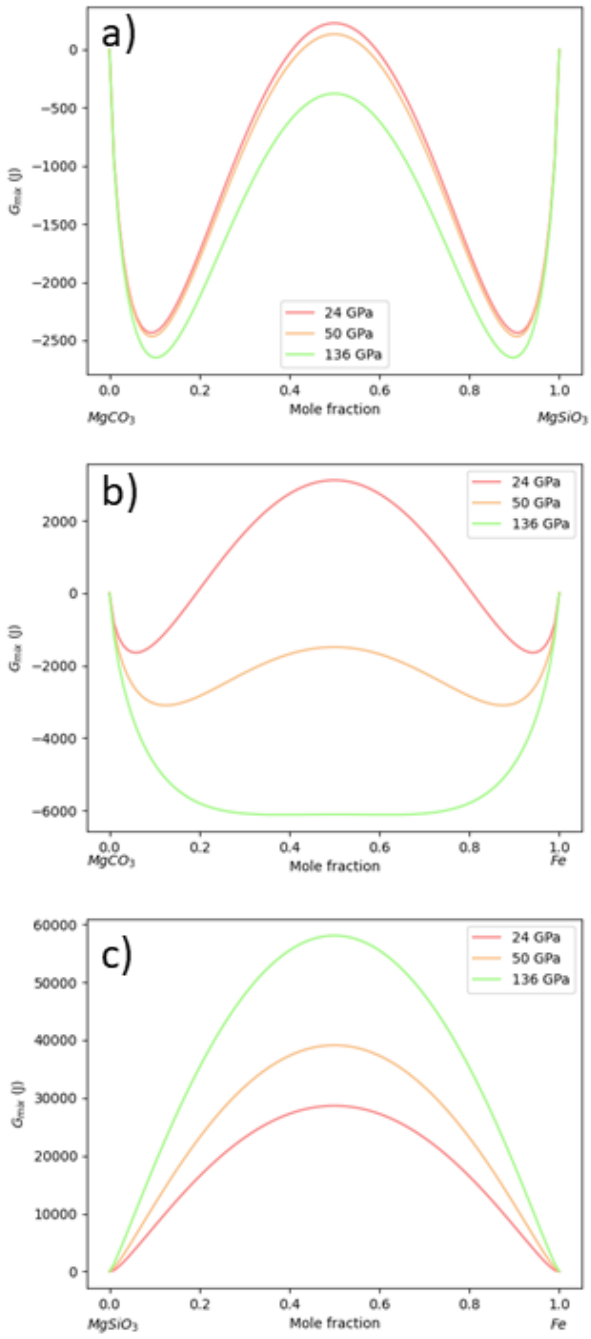

Figure 5.9: ΔG_{mix} for binary solutions of a) $MgCO_3$ and $MgSiO_3$; b) $MgCO_3$ and Fe; and c) $MgSiO_3$ and Fe at 24 GPa (red line), 50 GPa (orange line), and 136 GPa (green line). $MgCO_3$ and $MgSiO_3$ have limited miscibility near the endmembers that increases with pressure, and $MgSiO_3$ and Fe are immiscible at all pressures studied. $MgCO_3$ and Fe have limited miscibility at 24 GPa, and the miscibility gap closes with increasing pressure.

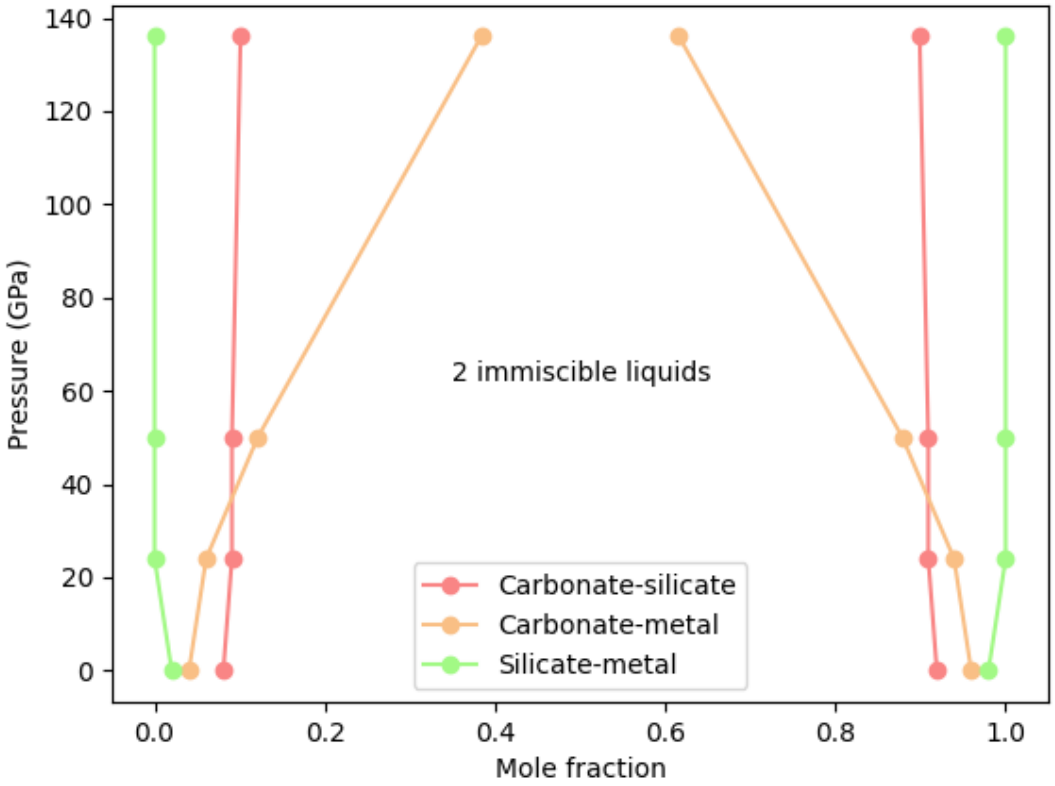

Figure 5.10: Phase diagram for binary melt mixtures with pressure. The central region inside each of the pairs of lines is the miscibility gap, where it is more energetically favorable to form two melt immiscible melt compositions. The miscibility gap closes with increasing pressure for carbonate-silicate and carbonate-metal mixtures, but widens for silicate-metal mixtures.

metal and the carbonate-silicate miscibility gaps close with pressure, the miscibility fields near the iron and $MgCO_3$ endmembers and near the $MgCO_3$ and $MgSiO_3$ endmembers grow to accommodate more mixing, as indicated by the increasing size of the regions drawn in Figure 5.11. In between the miscibility fields are two melt regions, labelled with a 2, and compositions that fall in these regions will exsolve two immiscible melts. Dashed gold lines represent example tie lines in these regions. The central triangle marked by the solid gold lines in each of the figures and labelled with a 3 is the three melt region, and compositions that fall in this region

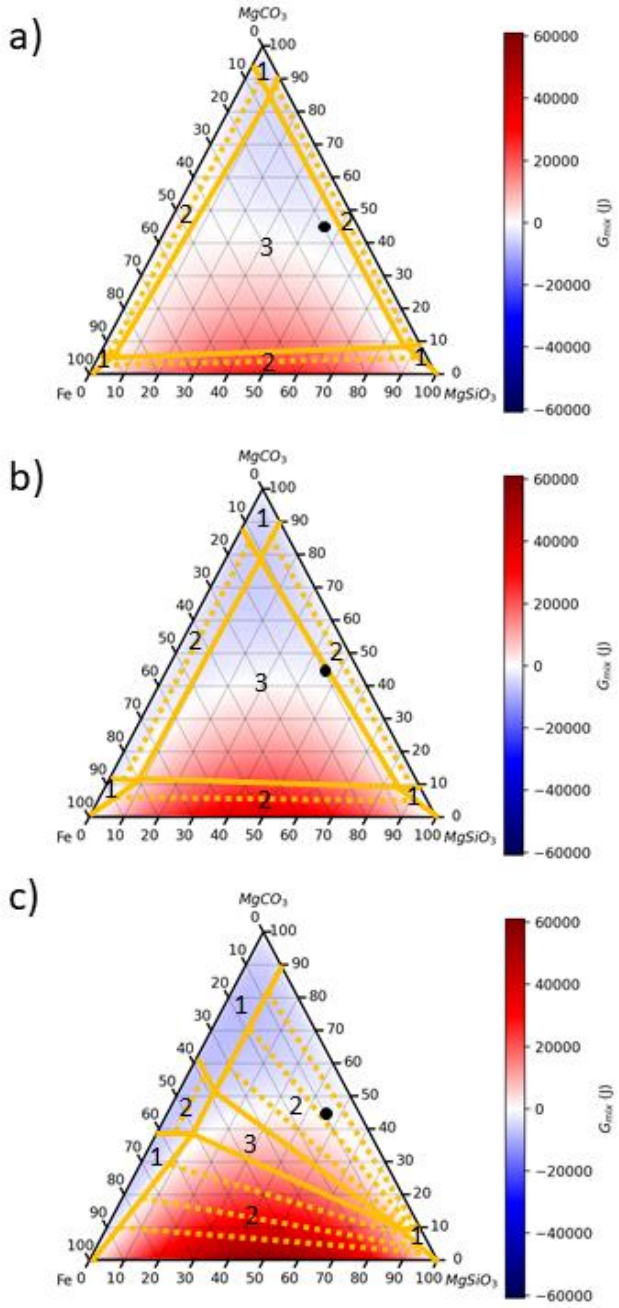

Figure 5.11: ΔG_{mix} for ternary solutions of $MgCO_3$, $MgSiO_3$, and Fe at a) 24 GPa; b) 50 GPa; and c) 136 GPa. Positive values of ΔG_{mix} are shaded red and negative values are shaded blue. Solid gold lines outline miscible melt compositions, two coexisting melt regions, and three coexisting melt regions, labelled with a 1, 2, or a 3, respectively, and are estimated from the ΔG_{mix} values on the binaries. Dashed gold lines are tie lines in the two melt regions. The ternary composition simulated for this study is labelled with a black dot.

will exsolve three immiscible melt compositions. With increasing pressure, the two melt regions grow and the three melt region shrinks, indicating the overall decrease in immiscibility in this system at high pressure. The chosen value for ΔH_{mix} affects the miscibilities of the melt mixtures. We estimated values for ΔH_{mix} based on chemical speciation and literature experiments, but without additional constraints there is some ambiguity in the selected value. The blue regions of the plot indicate compositions with negative ΔG_{mix} values, and thus, show a possible range of miscible compositions that are available under smaller ΔH_{mix} values. Nonetheless, the results based on these reasonable estimates of ΔH_{mix} illustrate the plausibility of reduced immiscibility with increasing pressure in the carbonate-metal system, such than an Fe-rich carbonate melt would be expected to segregate from other phases at the base of the mantle.

5.3.3 Cluster densities

As evidenced by Figure 5.11, many carbonate-silicate-metal melt compositions are immiscible at lower mantle conditions, even at the high-pressure conditions of the core-mantle boundary. In particular, the ternary melt composition simulated in this study falls into an immiscible melt region at all lower mantle conditions. Although *ab initio* molecular dynamics cannot model phase separation, the clustering of species we observe in our simulations is suggestive of melt separation. In this section, we identify the species that segregate in an example melt composition through speciation analysis and determine individual cluster densities to understand how elements distribute throughout the lower mantle.

A more complete speciation analysis of this melt composition is reported in Chapter 4. In general, we observe large increases in C-Fe and C-C bonding with pressure at the expense of C-

O bonding. No evidence of Fe-Si bonding is found at any pressure. These tendencies are in good agreement with the predicted miscibilities for binary solutions (Figure 5.9), which show limited miscibility of carbonate and silicate melts, more extensive miscibility of carbonate and metal melts at high pressure, and immiscibility of metal and silicate melts. In the melt, large carbon-carbon and carbon-iron clusters form, and have limited interaction with the silicate melt network, indicating the types of carbon-bearing species we might expect to segregate from a silicate melt. However, the extent of carbon-iron interaction is difficult to quantify. Carbon-iron clusters often consist of iron atoms surrounding a polymerized carbon core, which could be classified as either a diamond seed nucleus or an iron carbide cluster. To classify these clusters, we examine carbon bond abundances and compare them to results from statistical sampling. Statistical sampling is calculated by assuming that each cation has no chemical preference for any of the bonding atoms, and instead coordinates with a randomized selection from the available anions. In the case of the carbon clusters, we would expect 12% (13/108) of the carbon bonds to be C-Fe bonds, as there are 13 iron atoms from an available 108 coordinating anions for carbon (12 silicon, 72 oxygen, 11 carbon, and 13 iron). Additionally, we anticipate that 67% (72/108) of carbon bonds are to oxygen. Bond abundances greater than the abundances predicted from statistical sampling indicate that there is a chemical preference for the bonding element. In our cluster analysis, we classify carbon clusters with C-O bond abundances greater than 67% as carbonates and carbon clusters with C-Fe bond abundances greater than 12% as iron carbide. Clusters with less C-O and C-Fe abundances than expected from statistical sampling are classified as diamonds. In Figure 5.12, we plot the fraction of C-Fe bonds versus the fraction of C-O bonds for all carbon clusters that form in a simulation at either 1, 74, or 148 GPa. At all three pressures, clusters of each type

are formed, but the relative abundances of the cluster types evolve with pressure. Carbonates are the most abundant cluster type at 1 GPa and account for 49% of the total clusters, but that number drops to 31% at 74 GPa and 30% at 148 GPa. Iron carbides almost match the number of carbonate clusters at 1 GPa, at 48% of the total, and are the most abundant cluster type at 74 and 148 GPa, at 55% and 64% of the total, respectively. Diamond clusters are always the least abundant cluster type. They increase in abundance from 3% to 14% from 1 to 74 GPa, and then decrease in abundance to 5% at 148 GPa. In Chapter 4, we notice that the majority of changes in C-O and C-C bond abundances occur in the first 25 GPa. Thus, we expect diamond cluster

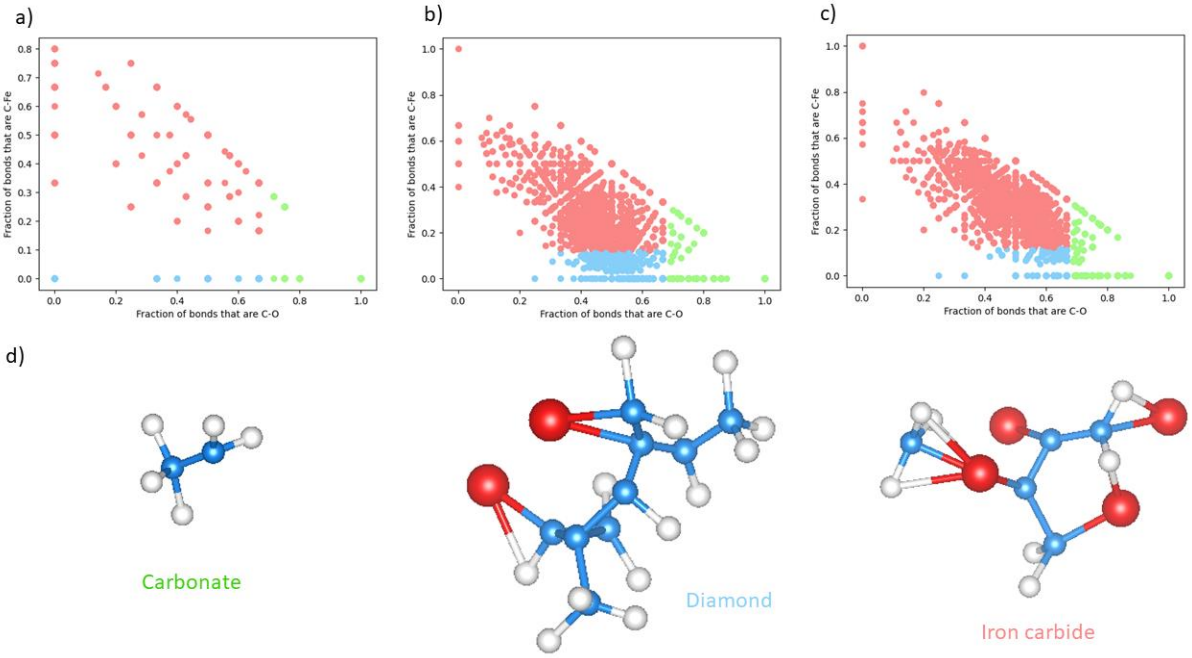

Figure 5.12: Carbon clusters identified at a) 1 GPa, b) 74 GPa, and c) 148 GPa. Clusters are plotted by fraction of bonds that are C-O and fraction of bonds that are C-Fe. Clusters with high C-O bond abundances are classified as carbonates (green). Clusters with high C-Fe bond abundances are classified as iron carbides (red). Clusters with low C-O and C-Fe bond abundances are classified as diamonds (blue). d) Examples of isolated carbon-iron-oxygen clusters classified as diamond, carbonate, and iron carbide from 74 GPa and 4,000 K. Carbon atoms are blue, oxygen atoms are white, and iron atoms are red.

formation to peak around 25 GPa, and this expectation is reflected in the relative increase in diamond cluster formation between 1 and 74 GPa. Similarly, we expect carbonate cluster abundance to decrease rapidly in the first 25 GPa, before plateauing, and this result is also reflected in the carbonate cluster abundances. Finally, the large and steadily increasing number of iron carbide clusters matches the speciation results in Chapter 4 and in Solomatova et al. (2019), which both report linear increases in C-Fe bond abundances with increasing pressure.

The composition and the volume of the carbon clusters determines their relative density within the mantle. Using the Bader charge analysis algorithm (Henkelman et al., 2006; Sanville et al., 2007; Tang et al., 2009; Yu and Trinkle, 2011), we calculate the volumes of individual atoms within carbon clusters to determine their densities. When calculating densities of iron carbide and diamond clusters, we remove the oxygen atoms from the density calculation. Densities of example carbon clusters isolated at 74 and 148 GPa are plotted in Figure 5.13. The

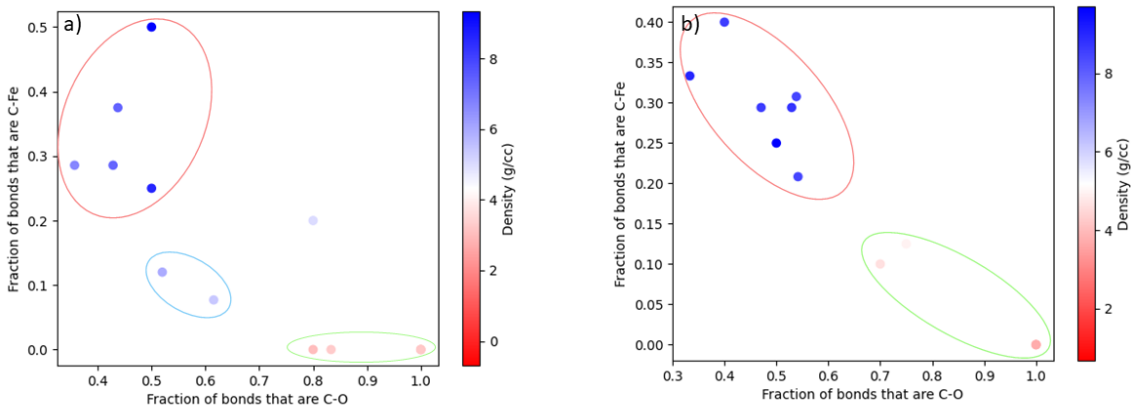

Figure 5.13: Carbon clusters identified from three separate snapshots at a) 74 GPa and b) 148 GPa and plotted by fraction of bonds that are C-O and fraction of bonds that are C-Fe. Circled points correspond to carbonates (green), iron carbides (red), and diamonds (blue). Data points are colored by density of the cluster. Clusters denser than $MgSiO_3$ (blue) will sink and clusters less dense than $MgSiO_3$ (red) will float.

selected clusters are grouped according to their classification as a carbonate, iron carbide, or diamond cluster. We directly compare the density of the cluster to the calculated density of $MgSiO_3$ melt at the same conditions. Iron carbide clusters are much denser than $MgSiO_3$ melt, and with enough time and aggregation, we expect these clusters to segregate from the multicomponent melt and sink to the core. Similarly, diamond clusters are denser than $MgSiO_3$ melt. Carbonate clusters are lighter than $MgSiO_3$ melt, and we expect these clusters to be buoyant within the mantle.

5.4 Implications

The role of carbonate melts in the deep Earth has been previously discussed (Ghosh et al., 2017; Kaminsky et al., 2015; Sanloup et al., 2019), with arguments both for and against their existence and their importance. Recent reports of carbonate stability in the lower mantle (Dorfman et al., 2018; Lv et al., 2021) and evidence of carbonate inclusions in deep Earth diamonds (Agrosì et al., 2019; Kaminsky et al., 2009) lends credence to the notion that carbonate melts exist and play a role in the lower mantle and at the core-mantle boundary. At these depths, carbonate melts likely interact with more common lower mantle melts such as silicate or metal melts. In this study, we predict the miscibility of carbonate melts with silicate and metal melts. We find that carbon is contained in miscible ternary melt compositions or exsolved from the melt in the form of iron carbide or diamond clusters. Based on our results, we evaluate the implications for carbon distribution and sequestration in the lower mantle and the core.

Carbon contained in ternary melt compositions could be a possible explanation for ULVZs. ULVZs have multiple proposed explanations, including FeSi formed through core-

mantle reactions (Mergner et al., 2021), hydrous phases such as (Al,Fe)OOH (Thompson et al., 2021), Fe-rich post perovskite (Garnero and McNamara, 2008), and patches of partial melt (Williams and Garnero, 1996). Partial melt is a likely explanation for ULVZs due to the 3:1 ratio of S-to-P wave velocity reduction (Garnero and McNamara, 2008; Williams and Garnero, 1996), and as such, carbonate-silicate-metal melts that are gravitationally stable at the core-mantle boundary could serve as an explanation. The miscibilities calculated for ternary melts at 136 GPa indicate that a multitude of melt compositions are possible (Figure 5.11c). We consider the densities of ternary melt compositions in Figure 5.14. All melt compositions with iron content greater than 10 atomic percent are denser than $MgSiO_3$ melt. However, only the ternary

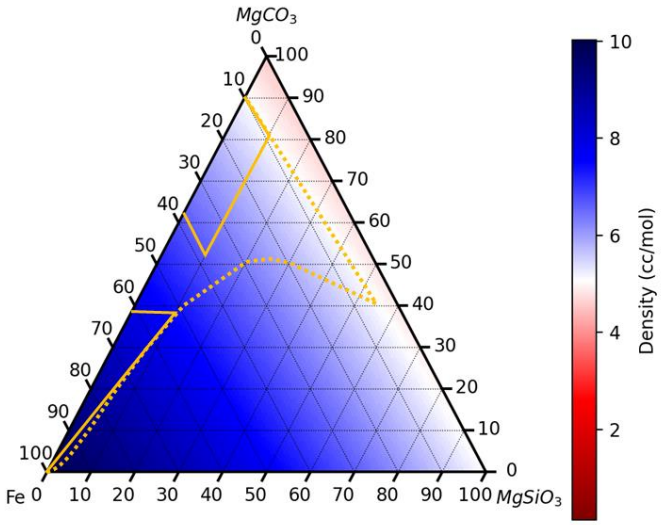

Figure 5.14: Densities of ternary melt compositions at 136 GPa compared to the density of $MgSiO_3$ melt. Melts denser than $MgSiO_3$ and less dense than pure Fe are colored blue, and would be buoyantly stable at the core-mantle boundary. Melts less dense than $MgSiO_3$ are colored red, and would float. Melts that are both miscible and denser than $MgSiO_3$ are indicated by the solid gold outlines and are candidate compositions for ULVZs or for carbon-rich outer core liquids. The dotted gold outline shows compositions that are both denser than $MgSiO_3$ and have negative ΔG_{mix} values.

compositions marked by the solid gold outlines on the plot are both miscible and denser than $MgSiO_3$ melt at these conditions. Two groups of melts emerge: an iron-rich, silicate-poor carbonate melt and a carbonate-rich, silicate-poor iron melt. Melts of these compositions could be formed from a deep Earth carbonatite melt interacting with metal melt at the core-mantle boundary. The iron-rich, silicate-poor carbonate melt has a density slightly larger than $MgSiO_3$ melt and would be gravitationally stable at the core-mantle boundary. It could serve as one possible explanation for ULVZs. The carbonate-rich, silicate-poor iron melt is so dense that it could sink into the outer core, dragging carbon and silicon with it. The dotted gold line maps out the regions of the plot where melts are both denser than $MgSiO_3$ and have negative ΔG_{mix} values. This outline serves to illustrate a range of miscible melt compositions that are possible with different values of ΔH_{mix}.

The majority of the ternary carbonate-silicate-metal melt compositions, however, are immiscible at the core-mantle boundary (Figure 5.11c), and we expect these melts to separate and to exsolve chemical species. Taking our simulated ternary melt composition as an example, we observe that the melt separates into three components at low pressure, and a silicate component and a carbon- and iron-bearing component at high pressure. Within the carbon-bearing components, we see clusters corresponding to iron carbide, diamond, and carbonate (Figure 5.12). The iron carbide and diamond clusters likely exsolve from the melt, as has been previously suggested (Dasgupta and Hirschmann, 2010; Karki et al., 2020; Mysen et al., 2011; Stagno et al., 2013). The majority of the clusters at 148 GPa are iron carbide (64%), and the propensity for carbon to bond with iron indicates carbon's high siderophility under these thermodynamic conditions. Iron carbide clusters are denser than the surrounding mantle (Figure

5.13), and thus, a significant amount of Earth's carbon contained in the lower mantle would bond with iron and sink to the core, matching previous predictions of carbon's fate under reduced conditions in the lower mantle (Karki et al., 2020; Rohrbach and Schmidt, 2011). In this scenario, carbon is being transported to the core, which not only prevents carbon from being recycled back to the Earth's surface, but also affects the evolution of the core's composition. An increasingly carbon-rich core composition would have implications for the core's density, sound velocities, and electrical and thermal conductivity (Fiquet et al., 2009; Ghosh and Karki, 2017; Wood et al., 2013). Additionally, the abundance of iron carbide clusters has implications for core-mantle differentiation in the early Earth. After the Moon-forming impact, metal and silicate melts would be well-mixed and siderophile elements would be segregated with iron into the core. Carbon's affinity for iron indicates that the majority of carbon present in the magma ocean would follow iron during core segregation, supporting the idea that carbon is a candidate element to explain the density deficit in the core (Prescher et al., 2015; Solomatova et al., 2019).

Additionally, we observe the formation of carbon polymers in our simulated ternary melt composition, which could be precursors for diamonds. Our simulations reveal a possible mechanism for diamond formation, where carbon polymers exsolve from a silicate melt. Previously, this formation mechanism was observed in oxygen-deficient carbon-bearing silicate melts (Ghosh et al., 2017), but the addition of iron in our simulations may actually increase carbon polymerization (Belonoshko et al., 2015). Our speciation analysis of this melt composition (see Chapter 4) indicates that carbon-carbon bond formation reaches a peak around 25 GPa, beyond which it plateaus. C-Fe bonding, however, increases linearly and with increasing depth, the percentage of diamond clusters decreases as iron carbide clusters are preferentially

formed. Thus, our analysis indicates a diamond formation zone around 25 GPa. This depth in the Earth matches reports of diamonds with a deep Earth origin, which are returned from either the transition zone or the top of the lower mantle (Smith et al., 2016; Stachel et al., 2005). However, our cluster analysis (Figure 5.12) indicates that diamonds are formed even at the core-mantle boundary, and these diamonds may be brought to the surface by deep mantle plumes. Diamonds with a lowermost mantle origin may be identified through compositional analysis of fluid inclusions. Diamonds containing silicate-poor metal-rich carbonate melt compositions that fall into the miscible melt region indicated in Figure 5.11c would indicate a core-mantle boundary origin and would provide evidence for carbonate-silicate-metal melt reactions in the lowermost mantle.

From our analysis of the densities and miscibilities of multicomponent melts, we examine example carbon distributions for various melt compositions at the pressure and temperature conditions of the core-mantle boundary. An equimolar composition (i.e. 1/3 Fe, 1/3 $MgCO_3$, and 1/3 $MgSiO_3$) falls into the three melt region of the ternary plot. Of the three melts that exsolve from this composition, 31% is iron-rich silicate-poor carbonate melt, 37% is carbonate-rich silicate-poor iron melt, and 32% is silicate melt. From mass balance calculations, we determine that 90% of the carbon in this composition is contained in potential ULVZ and outer core compositions (carbonate and iron melt) while 10% is contained in buoyant silicate melt. Thus, the majority of carbon remains in the Earth's deep interior while 10% is recycled back to the upper mantle. For our other three example compositions, we evaluate a carbonate-rich (10% Fe, 70% $MgCO_3$, 20% $MgSiO_3$), an iron-rich (80% Fe, 10% $MgCO_3$, 10% $MgSiO_3$), and a silicate-rich (10% Fe, 10% $MgCO_3$, and 80% $MgSiO_3$) composition. These compositions fall into the

two melt regions of the ternary plot, and exsolve two coexisting melt compositions. In the carbonate-rich composition, 86% is iron-bearing carbonate melt and 14% is silicate melt. In the iron-rich composition, 93% is carbon-bearing iron melt and 7% is silicate melt. In the silicate-rich composition, 90% is silicate melt and 10% is carbon-bearing iron melt. From mass balance calculations, we determine that 98%, 96%, and 31% of the available carbon is contained in potential ULVZ or outer core compositions for the carbonate-rich, iron-rich, and silicate-rich compositions, respectively. Thus, it appears that in carbonate- and iron-rich compositions, carbon is preferentially stored in lower mantle phases, and even in silicate-rich compositions, a significant fraction of the available carbon remains in the deep Earth. This analysis highlights the potential distribution of carbon between various carbon-bearing melts at the core-mantle boundary. Carbon appears to be preferentially stored in the deep Earth, indicating that the ultimate fate of Earth's carbon may be storage in the deep interior.

CHAPTER 6

CONCLUSIONS

This thesis describes the fate of carbonate phases subducted from the Earth's surface to the core-mantle boundary, probing their stabilities, reactivities, miscibilities, and physical properties with the goal of understanding the distribution and storage of carbon in the Earth. In Chapter 2, I examined the stability of solid carbonate phases when reacting with metal alloys as a possible pathway for carbon transport into the lower mantle. Chapter 4 used computational methods to study the speciation and coordination of carbonate melts interacting with silicate and metal melts in the lower mantle. In Chapter 5, the densities and miscibilities of carbonate-silicate-metal melts were calculated with computational methods and evaluated for carbon storage in the deep Earth. By examining carbonates in lower mantle phase assemblages, this thesis aims to determine a realistic distribution of carbon-bearing phases within the Earth.

Carbonates reacting with iron metal at high pressures have been shown to generate iron carbides, diamonds, and carbonate melts (Dorfman et al., 2018; Martirosyan et al., 2015a; Martirosyan et al., 2015b; Martirosyan et al., 2016; Palyanov et al., 2013; Zhu et al., 2019). Carbonates reacting with Fe_3Si have similar behavior, participating in various reactions to make perovskite phases, iron carbides, and oxides. The temperature at which the carbonate phase reacts, however, increases with pressure, indicating the increased stability of the carbonate phase relative to perovskites, carbides, and oxides with depth in the Earth. This increased stability additionally implies that carbon becomes less siderophile with respect to silicon with increasing pressure. When compared against a mantle geotherm (Anzellini et al., 2013), we find that the

stability range for $MgCO_3$ spans from 33-130 GPa and for $CaCO_3$ spans from 66-131 GPa. $MgCO_3$ appears to be more stable than $CaCO_3$ for the majority of the lower mantle, but due to a phase change in $CaCO_3$, $CaCO_3$ replaces $MgCO_3$ as the stable carbonate at 126 GPa. This work examines the stability of carbonate phases in an example lower mantle phase assemblage, and demonstrates the ability of carbonates to be preserved and transported to the lower mantle in subducting slabs. In phase assemblages with similar redox conditions, we would expect carbonate stability to persist, thus providing a source of oxidized carbon to the lower mantle.

Once carbonates are in the lower mantle, they are able to melt and react with other phases. The simulations in this thesis of a high-pressure carbonate-silicate-metal melt highlight the important effect of carbon content on chemical and physical properties of melts. In the subequal carbonate-silicate-metal melt composition, coordination numbers increase continuously with pressure, allowing for coexistence of multiple coordination environments, and the distributions of these coordination states broaden around non-preferred coordination environments and with increasing temperature. Bond lengths tend to increase with coordination changes in the melt, but otherwise shorten with pressure. Silicon and carbon have the longest-lived coordination states, indicating their role as network formers, but the lifetimes of coordination states for all elements decreases with pressure, indicating the changing nature of the melt network with pressure. Additionally, silicon and carbon generally have the lowest diffusivities of all the elements, indicating that they are network formers. Compared to less carbon-rich melts (Solomatova et al., 2019), carbon in the subequal carbonate-silicate-metal melt has a relatively low diffusivity, indicating that carbon-rich melts may be less well-mixed than their relatively carbon-poor counterparts. However, carbon-bearing melts have greater

diffusivities than carbon-free melts (Karki et al., 2009), indicating their relatively low viscosities compared to volatile-free melts. Due to the high iron content of the melt, it is conducting at all pressures. Iron has some magnetization, which diminishes above ~93 GPa upon the initialization of the iron spin transition.

In the subequal carbonate-silicate-metal melt composition, speciation is complicated, stemming from carbon's ability to behave as both a cation and an anion. With increasing pressure carbon begins to replace oxygen in the melt network, as C-O bond abundances decrease and are replaced by increases in C-C and C-Fe bonding. Carbon and iron undergo redox exchange, and carbon oxidizes iron to become more reduced. As a result, carbon polymers and carbon-iron clusters grow while carbonate abundances decrease. Our system has an excess of carbon polymers compared to less carbon-rich systems, indicating a propensity for carbon to bond with itself at the expense of other types of bonds. Thus, carbonate-silicate-metal melts may be a parent melt for diamond genesis, or for a dense C-Fe liquid.

Analysis of isolated carbon clusters confirms the trends observed in the speciation results. In the subequal carbonate-silicate-metal melt composition, we observe clustering of carbon and iron that is suggestive of species exsolution. We classify the clusters as carbonate, diamond, or iron carbide. A majority of the clusters are carbonates at low pressure, but we find that carbonate abundance decreases rapidly within the first 25 GPa, before stabilizing. Similarly, diamond abundance increases rapidly within the first 25 GPa, before falling off, indicating that the majority of diamonds are formed in the upper mantle, transition zone, or the top of the lower mantle. Iron-carbide abundances increase linearly with pressure. The propensity for carbon to bond with iron indicates that much of the carbon contained in the magma ocean early in Earth's

history was likely transported to the core during differentiation. Additionally, some component of carbon contained in the Earth's mantle today may ultimately end up in the core through interaction with the core or with free iron in the mantle. Density calculations of the individual clusters indicate that iron carbide and diamond clusters are gravitationally stable in the lower mantle, but carbonate clusters are buoyant and expected to rise through the mantle.

By examining the densities of carbonate, silicate, and metal melts and their binary and ternary mixtures, we determine which melt compositions are miscible, and which are immiscible and therefore likely to separate or to exsolve chemical species. Both carbonate-silicate and carbonate-metal melts have limited miscibility at low pressure. However, with increasing pressure, the miscibility gap for both melts begin to close, most substantially for carbonate-metal melt mixtures. Silicate-metal melts are immiscible at all lower mantle pressures. For ternary melt mixtures, mixing is limited to compositions close to the endmember compositions, but miscibility fields grow with increasing pressure. When comparing the densities of miscible melts at the core-mantle boundary with the density of $MgSiO_3$ melt, we find that compositions with less than 10% iron are buoyant, while all other miscible melt compositions are denser than the surrounding mantle. Two groups of miscible melt compositions emerge as candidate phases for carbon storage in the deep Earth: an iron-rich silicate-poor melt, and a carbonate-rich silicate-poor melt. The carbonate-rich melt composition could serve as a possible explanation for ultralow velocity zones, while the iron-rich melt composition is dense enough to sink into the core, bringing carbon and silicon with it. By combining the density and miscibility data, we calculate some example distributions of carbon into various carbon-bearing melts at the core-mantle boundary. In the majority of our analyses, most of the carbon is stored in potential ULVZ

or outer core compositions, indicating that the ultimate fate of carbon may be storage in the deep Earth.

The role of carbon in the deep Earth still remains incompletely understood, but mineral physics experiments are making strides to understand its distribution and cycling in the Earth's deep interior. Petrologic experiments on carbonates at lower mantle conditions, limited to studies performed in the last five years (Dorfman et al., 2018; Lv et al., 2021; Zhu et al., 2019), illustrate the potential for continued progress in this field of research. More experiments on carbon-bearing compositions are required to evaluate carbonate stability under a host of redox conditions, particularly compositions involving carbon, silicon, and iron in the same system. Additionally, *ab initio* simulations evaluating carbon-bearing melt mixtures are relatively new (Bajgain and Mookherjee, 2021; Ghosh et al., 2017; Ghosh and Karki, 2017; Karki et al., 2018), and few simulations study both carbon and iron in the same system (Karki et al., 2020; Solomatova and Caracas, 2021; Solomatova et al., 2019). The work in this thesis illustrates the effect carbon content has on speciation, indicating that more studies on a wider range of carbon-bearing compositions are necessary to understand carbon-bearing melt behavior in the lower mantle. Looking into the future, I anticipate mineral physics experiments will continue to be a powerful tool to produce constraints on carbon distribution and storage in the deep Earth, by expanding the compositions of carbon-bearing systems we examine.

APPENDIX A

SUPPLEMENTAL MATERIAL FOR CHAPTER 2

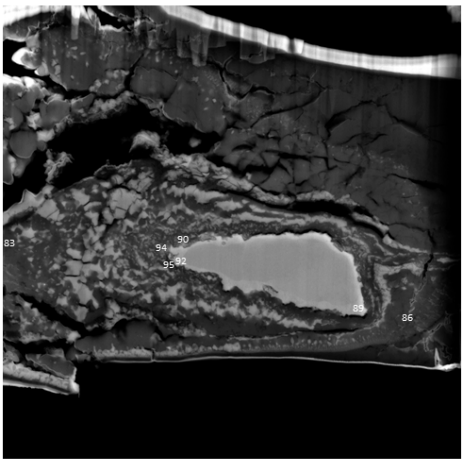

Point	O (%)	Si (%)	Ca (%)	Fe (%)	C (%)	Phases
83	58.15	18.78	17.56	5.51	0	$CaSiO_3$
86	50.35	0.79	23.54	2.36	22.85	$CaCO_3 + CaO$
89	7.79	14.77	1.91	75.54	0	$Fe_3(Si,O)$
90	44.52	18.73	1.76	34.99	0	$SiO_2 + Fe_3C/Fe_7C_3$
92	10.18	16.59	0.93	72.30	0	$Fe_3(Si,O)$
94	42.45	20.11	3.47	33.97	0	$SiO_2 + Fe_3C/Fe_7C_3$
95	49.55	21.21	8.88	20.26	0	$SiO_2 + Fe_3C/Fe_7C_3$

Figure A.1: EDS point analysis data not included in Chapter 2 text.

Pressure (GPa)	Reaction Temperature (K)
30	1514
32	1047
35	1485
40	1705
40	1508
48	1574
54	1842
55	1779
58	1778
69	2514
89	2763
106	2908

Table A.1: $CaCO_3$ reaction conditions.

Pressure (GPa)	Reaction Temperature (K)
29	1739
39	2183
46	2221
54	2378
37	2224
47	2390
58	2335
67	2552

Table A.2: $MgCO_3$ reaction conditions.

APPENDIX B

SUPPLEMENTAL MATERIAL FOR CHAPTER 4

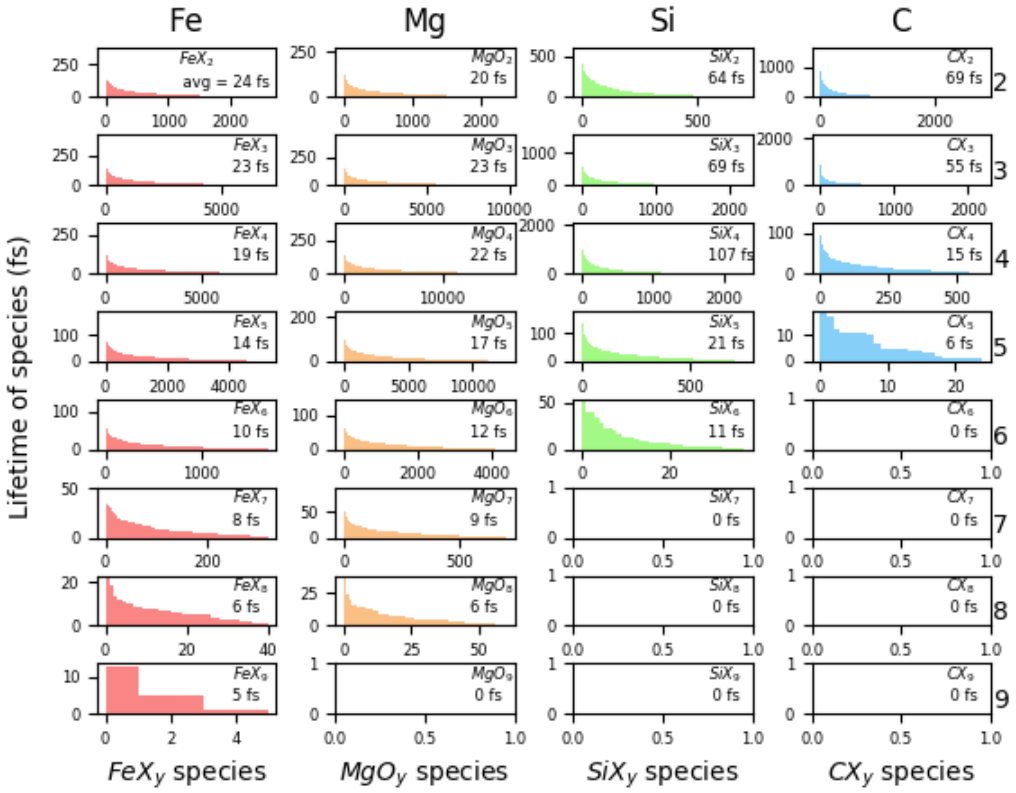

Figure B.1: Histogram of coordination state lifetimes for all cations at 4,000 K and 1 GPa. The x axis corresponds to the number of MX_y species, and the y axis corresponds to the lifetime of each species. Average coordination lifetimes are displayed in the top right corner of each plot. Coordination states that do not exist are left blank. Lifetime histograms are all skewed with a long tail.

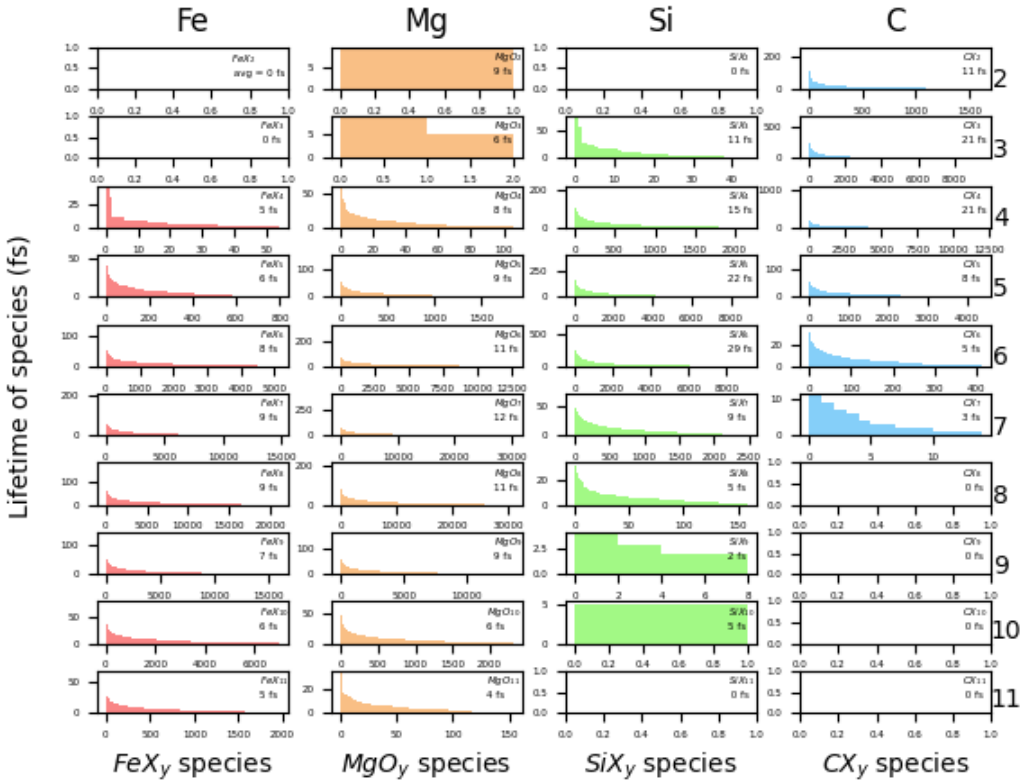

Figure B.2: Histogram of coordination state lifetimes for all cations at 4,000 K and 73 GPa. The x axis corresponds to the number of MX_y species, and the y axis corresponds to the lifetime of each species. Average coordination lifetimes are displayed in the top right corner of each plot. Coordination states that do not exist are left blank. Lifetime histograms are all skewed with a long tail.

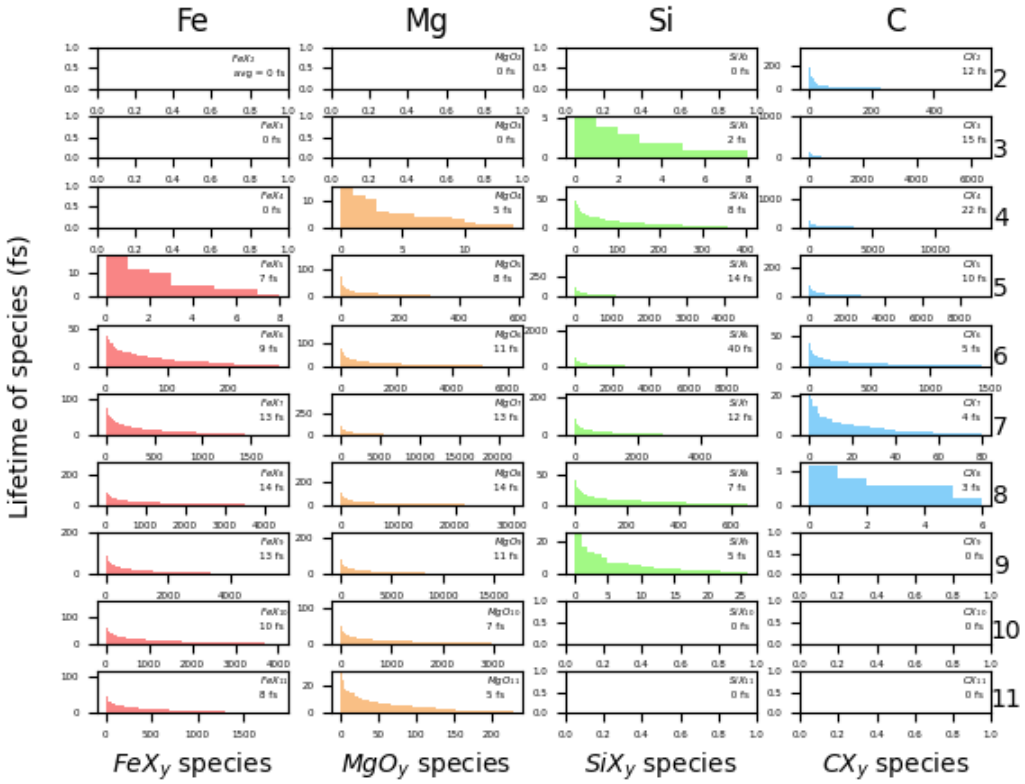

Figure B.3: Histogram of coordination state lifetimes for all cations at 4,000 K and 148 GPa. The x axis corresponds to the number of MX_y species, and the y axis corresponds to the lifetime of each species. Average coordination lifetimes are displayed in the top right corner of each plot. Coordination states that do not exist are left blank. Lifetime histograms are all skewed with a long tail.

Cell length (Å)	Pressure (GPa)	Temperature (K)	Maximum time (fs)	Number of starting configurations
13.5	0	2993	21710	2
11.5	10	2992	19574	2
11.0	21	2992	19960	2
10.5	40	2991	18246	2
13.5	1	3996	38659	2
11.5	14	3994	39443	2
11.0	25	3993	39814	2
10.7	37	3993	16808	5
10.5	46	3993	46695	2
10.4	52	3992	43561	6
10.1	74	3992	43956	2
9.9	93	3992	46910	2
9.7	118	3991	46030	2
9.5	148	3989	42940	2
9.5 (oxidized simulation)	151	3982	18000	1

Table B.1: Experimental conditions for simulations used in Chapter 4.

	Bond Length (Å) at 3,000 K and			
Bond	**0 GPa**	**10 GPa**	**21 GPa**	**40 GPa**
Si-O	1.64	1.64	1.63	1.65
Si-C	1.87	1.89	1.86	1.95
Mg-O	1.95	1.96	1.94	1.94
C-O	1.21	1.28	1.29	1.30
C-C	1.35	1.40	1.39	1.40
Fe-O	1.91	1.97	1.99	1.97
Fe-C	2.03	2.10	2.08	2.05

Table B.2: Bond length data at 3,000 K for Figure 4.4.

	Bond Length (Å) at 4,000 K and									
Bond	**1 GPa**	**14 GPa**	**25 GPa**	**46 GPa**	**52 GPa**	**74 GPa**	**93 GPa**	**118 GPa**	**148 GPa**	**151 GPa (oxidized simulation)**
Si-O	1.63	1.63	1.63	1.64	1.64	1.64	1.64	1.64	1.63	1.63
Si-C	1.95	1.89	1.86	1.85	1.86	1.84	1.82	1.83	1.79	1.79
Mg-O	1.94	1.94	1.94	1.91	1.91	1.89	1.87	1.86	1.84	1.83
C-O	1.20	1.27	1.28	1.30	1.30	1.30	1.31	1.31	1.30	1.30
C-C	1.27	1.36	1.39	1.40	1.40	1.41	1.41	1.40	1.39	1.39
Fe-O	1.9	1.95	1.95	1.94	1.94	1.93	1.91	1.90	1.88	1.87
Fe-C	2.07	2.05	2.05	2.06	2.04	1.97	1.94	1.91	.85	1.84

Table B.3: Bond length data at 4,000 K for Figure 4.4.

Species	Percent
C_2O_3	15.3
C_2O_2	9.0
FeC_2O_2	8.8
CO_4	7.4
C_3O_2	7.4
FeC_3O	5.6
C_3O	4.6
C_2O_3	3.7
Fe_2C_2O	2.2
FeC_2O_3	2.2
FeC_2O	2.2
FeC_3	1.8
FeC_2O_3	1.7
Fe_2C_3	1.7
FeC_4	1.5
SiC_2O_2	1.3
FeC_3O_2	1.2
$FeSiC_2$	1.2
$Fe_2C_2O_2$	1.2
Fe_2C_3O	1.2
SiC_3O	1.2
$FeCO_2$	1.2
$FeSiC_2O$	1.0
SiC_2O	0.8
C_4	0.8
Other	14.1

Table B.4: Carbon species abundances over the course of one simulation at 117 GPa and 4,000 K (from Figure 4.5).

		0 GPa	10 GPa	21 GPa	40 GPa
Percent of carbon bonds that are	C-O	81	60	55	51
	C-C	7	29	29	36
	C-Si	1	3	3	1
	C-Fe	10	8	14	11
Percent of iron bonds that are	Fe-O	95	96	94	95
	Fe-C	5	4	6	5
Percent of silicon bonds that are	Si-O	99	98	98	99
	Si-C	1	2	2	1

Table B.5: Bond abundance data at 3,000 K for Figure 4.6a.

		1 GPa	14 GPa	25 GPa	37 GPa	46 GPa	52 GPa	74 GPa	93 GPa	118 GPa	148 GPa	151 GPa (Oxidized simulation)
Percent of carbon bonds that are	C-O	87	63	58	56	53	54	52	50	51	51	49
	C-C	3	19	27	24	31	28	30	34	30	25	21
	C-Si	1	4	4	5	3	4	3	3	3	2	4
	C-Fe	8	15	11	15	13	15	15	13	16	21	26
Percent of iron bonds that are	Fe-O	96	93	96	93	95	94	94	95	93	90	91
	Fe-C	4	7	4	7	5	6	6	5	7	10	9
Percent of silicon bonds that are	Si-O	99	98	97	96	97	97	98	98	98	99	97
	Si-C	1	2	3	4	3	3	2	2	2	1	3

Table B.6: Bond abundance data at 4,000 K for Figure 4.6a.

		0 GPa	10 GPa	21 GPa	40 GPa
Average carbon coordination to	O	1.57	1.67	1.71	1.71
	C	0.14	0.81	0.89	1.21
	Si	0.03	0.09	0.08	0.05
	Fe	0.20	0.23	0.43	0.38
Average iron coordination to	O	3.41	5.47	5.96	6.52
	C	0.19	0.21	0.41	0.35
Average silicon coordination to	O	3.72	4.01	4.27	5.16
	C	0.03	0.09	0.08	0.05

Table B.7: Coordination data at 3,000 K for Figure 4.6b.

		1 GPa	14 GPa	25 GPa	37 GPa	46 GPa	52 GPa	74 GPa	93 GPa	118 GPa	148 GPa	151 GPa (Oxidized simulation)
Average carbon coordination to	O	1.70	1.77	1.74	1.80	1.77	1.82	1.87	1.87	1.97	2.06	2.08
	C	0.06	0.53	0.81	0.77	1.02	0.95	1.08	1.28	1.17	1.02	0.87
	Si	0.03	0.10	0.13	0.17	0.11	0.13	0.12	0.12	0.13	0.09	0.18
	Fe	0.16	0.43	0.33	0.49	0.44	0.50	0.55	0.47	0.63	0.86	1.11
Average iron coordination to	O	3.57	5.45	6.44	6.46	7.13	7.16	7.42	7.44	7.50	7.51	7.88
	C	0.15	0.39	0.30	0.45	0.41	0.46	0.51	0.43	0.58	0.80	0.78
Average silicon coordination to	O	3.47	4.11	4.37	4.65	4.97	5.11	5.42	5.61	5.79	5.91	5.78
	C	0.03	0.10	0.13	0.17	0.11	0.13	0.12	0.12	0.13	0.09	0.18

Table B.8: Coordination data at 4,000 K for Figure 4.6b.

	0 GPa	10 GPa	21 GPa	40 GPa
Average carbon cluster size	1.2	2.1	2.5	4.1

Table B.9: Average carbon cluster sizes at 3,000 K for Figure 4.8a.

	1 GPa	14 GPa	25 GPa	37 GPa	46 GPa	52 GPa	74 GPa	93 GPa	118 GPa	148 GPa
Average carbon cluster size	1.1	1.7	2.4	3.5	2.8	3.4	2.9	3.9	3.1	3.0
Average carbon iron cluster size	2.3	3.3	3.9		4.8	4.7	5.5	6.4	6.1	5.4

Table B.10: Average carbon and carbon iron cluster sizes at 4,000 K for Figure 4.8.

Carbonate species abundance	0 GPa	10 GPa	21 GPa	40 GPa
CO_x	68	31	20	14
CO	41	2	1	0
CO_2	16	5	5	0
CO_3	12	23	14	9
CO_4	0	1	1	4
CO_5	0	0	0	1

Table B.11: Carbonate species abundances reported as percentages at 3,000 K for Figure 4.9a.

Carbonate species abundance	1 GPa	14 GPa	25 GPa	46 GPa	52 GPa	74 GPa	93 GPa	118 GPa	148 GPa	151 (Oxidized Simulation)
CO_x	75	37	29	22	21	19	17	16	13	15
CO	29	3	1	0	0	0	0	0	0	0
CO_2	31	11	7	3	2	1	1	0	0	0
CO_3	15	22	18	14	12	8	6	4	3	2
CO_4	0	1	2	4	5	8	8	7	9	13
CO_5	0	0	1	1	1	3	2	4	0	0

Table B.12: Carbonate species abundances reported as percentages at 4,000 K for Figure 4.9a.

Species	1 GPa	14 GPa	25 GPa	46 GPa	52 GPa	74 GPa	93 GPa	118 GPa	148 GPa
CO	29	3	1	0	0	0	0	0	0
CO_2	31	11	7	3	2	1	1	0	0
CO_3	15	22	18	14	12	8	6	4	3
C_2O_2	2	9	14	14	15	12	8	9	5
C_3O	0	2	6	10	7	6	8	5	3
CO_4	0	1	2	4	5	8	8	7	9
C_2O_3	0	1	2	4	6	9	9	15	11
C_2O_2Fe	0	2	3	4	5	6	5	9	11
C_3O_2	0	1	1	3	3	4	8	7	4

Table B.13: Abundances of the nine most dominant species reported as percentages across all 4,000 K simulations for Figure 4.9b.

Average coordination number	0 GPa	10 GPa	21 GPa	40 GPa
Fe	3.6	5.7	6.4	6.9
C	1.9	2.8	3.1	3.4
Si	3.7	4.1	4.4	5.2
Mg	4.0	5.7	6.3	6.9

Table B.14: Average coordination numbers for all cations at 3,000 K for Figure 4.12a.

Average coordination number	1 GPa	14 GPa	25 GPa	37 GPa	46 GPa	52 GPa	74 GPa	93 GPa	118 GPa	148 GPa	151 GPa (oxidized simulation)
Fe	3.7	5.8	6.7	6.9	7.5	7.6	7.8	7.9	8.1	8.3	8.7
C	1.9	2.8	3.0	3.2	3.3	3.4	3.6	.37	3.9	4.0	4.2
Si	3.5	4.2	4.5	4.8	5.1	5.2	5.5	5.7	5.9	6.0	6.0
Mg	4.0	5.8	6.5	6.6	7.0	7.2	7.4	7.6	7.8	7.8	7.9

Table B.15: Average coordination numbers for all cations at 4,000 K for Figure 4.12a.

Coordination number	1 GPa	14 GPa	25 GPa	46 GPa	52 GPa	74 GPa	93 GPa	118 GPa	148 GPa
1	1	0	0	0	0	0	0	0	0
2	10	0	0	0	0	0	0	0	0
3	30	2	1	0	0	0	0	0	0
4	35	10	5	0	0	0	0	0	0
5	18	25	17	3	3	2	1	1	0
6	5	31	29	15	15	10	8	7	4
7	1	21	27	31	31	27	26	24	20
8	0	9	15	30	30	34	35	35	33
9	0	3	5	15	15	19	21	23	26
10	0	1	1	5	5	6	7	8	11
11	0	0	0	1	1	1	2	2	3
12	0	0	0	0	0	0	0	1	1

Table B.16: Abundances of Fe coordination numbers reported as percentages at 4,000 K for Figure 4.12b and Figure 4.14.

Coordination number	1 GPa	14 GPa	25 GPa	46 GPa	52 GPa	74 GPa	93 GPa	118 GPa	148 GPa
2	5	0	0	0	0	0	0	0	0
3	24	1	0	0	0	0	0	0	0
4	39	9	2	0	0	0	0	0	0
5	25	30	14	6	4	2	1	1	1
6	7	37	35	26	21	14	11	8	8
7	1	18	33	39	38	36	34	30	30
8	0	4	13	23	28	35	38	40	41
9	0	0	2	5	8	13	14	18	18
10	0	0	0	0	1	2	2	3	3

Table B.17: Abundances of Mg coordination numbers reported as percentages at 4,000 K for Figure 4.12c and Figure 4.14.

Coordination number	1 GPa	14 GPa	25 GPa	46 GPa	52 GPa	74 GPa	93 GPa	118 GPa	148 GPa
1	1	0	0	0	0	0	0	0	0
2	9	1	0	0	0	0	0	0	0
3	32	8	3	1	0	0	0	0	0
4	55	64	50	21	14	6	3	1	1
5	3	25	40	50	47	37	28	19	13
6	0	2	7	27	36	52	61	67	72
7	0	0	0	1	3	5	7	11	13
8	0	0	0	0	0	0	0	1	1

Table B.18: Abundances of Si coordination numbers reported as percentages at 4,000 K for Figure 4.12d and Figure 4.14.

Coordination number	1 GPa	14 GPa	25 GPa	46 GPa	52 GPa	74 GPa	93 GPa	118 GPa	148 GPa
1	36	4	2	0	0	0	0	0	0
2	37	25	17	8	7	3	2	2	1
3	25	56	61	50	48	38	31	26	17
4	1	14	19	36	40	49	56	59	60
5	0	1	1	5	5	9	10	12	20
6	0	0	0	0	0	1	1	1	2

Table B.19: Abundances of C coordination numbers reported as percentages at 4,000 K for Figure 4.12e and Figure 4.14.

Coordination number	1 GPa	74 GPa	148 GPa
1	25	0	0
2	28	0	0
3	30	0	0
4	25	7	0
5	19	9	8
6	14	11	12
7	11	12	14
8	8	12	14
9	5	10	13
10	0	8	10
11	0	7	8
12	0	6	7
13	0	6	6
14	0	2	6
15	0	1	5
16	0	0	3

Table B.20: Lifetimes of Fe coordination numbers reported in femtoseconds at 4,000 K for Figure 4.15a.

Coordination number	1 GPa	74 GPa	148 GPa
1	21	0	0
2	25	9	0
3	29	7	0
4	27	11	7
5	22	12	12
6	16	15	16
7	13	16	18
8	8	15	18
9	0	12	15
10	0	9	10
11	0	6	7
12	0	12	6
13	0	0	1

Table B.21: Lifetimes of Mg coordination numbers reported in femtoseconds at 4,000 K for Figure 4.15b.

Coordination number	1 GPa	74 GPa	148 GPa
1	36	0	0
2	83	0	0
3	95	12	13
4	157	20	11
5	28	29	20
6	9	39	54
7	0	13	16
8	0	8	9
9	0	3	6
10	0	5	0

Table B.22: Lifetimes of Si coordination numbers reported in femtoseconds at 4,000 K for Figure 4.15c.

Coordination number	1 GPa	74 GPa	148 GPa
1	160	11	8
2	80	16	13
3	92	28	20
4	17	27	31
5	6	12	15
6	0	7	9
7	0	4	3

Table B.23: Lifetimes of C coordination numbers reported in femtoseconds at 4,000 K for Figure 4.15d.

Atom	1 GPa	74 GPa	148 GPa
Fe	1.0	1.2	1.2
C	1.1	0.8	0.7
Si	2.5	3.1	3.2
Mg	1.6	1.6	1.6
O	-1.3	-1.4	-1.4

Table B.24: Oxidation states of elements at 4,000 K for Figure 4.17a.

Percent of bonds that are C-O	Carbon oxidation state
0.5	0.6
0.5	0.1
0.5	0.8
0.5	0.6
0.5	0.1
0.5	0.9
0.5	0.4
0.6	1.9
0.7	1.2
0.7	1.3
0.7	1.2
1	2.0
1	0.8
1	1.4
1	0.9
1	2.0
1	1.0
1	1.9
1	0.6
1	0.5
1	1.2
1	1.1
1	0.5
1	1.1
1	2.0
1	1.7
1	2.0
1	1.2
1	0.3
1	0.7
1	0.7
1	1.8
1	1.7
1	1.9
1	1.0
1	2.0

Table B.25: Carbon oxidation state as a function of percent of bonds that are C-O at 1 GPa and 4,000 K for Figure 4.17b.

Percent of bonds that are C-O	Carbon oxidation state
0	0
0	0.4
0	0.6
0	0.2
0	0.3
0	0.4
0.25	0.1
0.25	0.3
0.25	0.2
0.3	0
0.3	0.4
0.3	0.5
0.3	0.4
0.5	1.0
0.5	1.0
0.5	1.1
0.5	0.4
0.5	0.4
0.5	0.6
0.5	1.4
0.7	0.4
0.7	1.1
0.7	1.5
0.7	1.0
0.7	0.8
0.7	0.7
0.7	1.2
0.75	1.3
0.75	1.5
0.75	1.6
0.75	1.6
0.75	1.6
0.8	1.9
1	2.1
1	2.2
1	2.2

Table B.26: Carbon oxidation state as a function of percent of bonds that are C-O at 74 GPa and 4,000 K for Figure 4.17b.

Percent of bonds that are C-O	Carbon oxidation state
0	0.3
0.2	0
0.2	0.9
0.25	0.3
0.25	0.3
0.25	0.2
0.25	0.6
0.3	0.4
0.3	0.2
0.4	0.2
0.4	0.6
0.4	0.1
0.5	1.5
0.5	0.9
0.5	1.3
0.5	0.3
0.5	0.7
0.5	0.1
0.5	1.1
0.5	0.3
0.5	1.1
0.6	1.6
0.6	1.0
0.7	0.6
0.7	1.3
0.75	1.8
0.75	1.6
0.75	1.3
0.75	1.7
0.75	1.3
0.75	1.6
0.75	1.2
0.75	1.7
1	2.4
1	2.2
1	2.0

Table B.27: Carbon oxidation state as a function of percent of bonds that are C-O at 148 GPa and 4,000 K for Figure 4.17b.

Percent of bonds that are C-O	Carbon oxidation state
0	1.5
0	0.7
0	0.3
0	1.0
0.2	0.4
0.2	0
0.25	0.8
0.25	0.1
0.25	0.3
0.25	0.6
0.3	0.2
0.3	0.7
0.4	0.8
0.5	1.0
0.5	0.6
0.5	0.7
0.5	0.7
0.5	0
0.5	0.4
0.6	0.7
0.6	1.2
0.7	1.7
0.75	1.4
0.75	1.4
0.75	1.0
0.75	1.5
0.75	1.4
0.75	1.3
0.8	1.8
0.8	1.1
1	2.2
1	2.1
1	2.1
1	2.2
1	1.6
1	2.2

Table B.28: Carbon oxidation state as a function of percent of bonds that are C-O at 151 GPa and 4,000 K (oxidized simulation) for Figure 4.17b.

Atom	0 GPa	10 GPa	21 GPa	40 GPa
Fe	14.3	6.7	6.4	2.8
C	24.1	3.9	2.7	1.8
Si	5.5	3.1	2.2	1.4
Mg	13.3	6.2	5.0	2.3
O	11.4	4.7	4.0	2.3

Table B.29: Diffusivity values at 3,000 K reported as 10^9 m^2/s for Figure 4.18a.

Atom	1 GPa	14 GPa	25 GPa	46 GPa	52 GPa	74 GPa	93 GPa	118 GPa	148 GPa
Fe	27.8	15.8	8.9	6.6	5.7	3.8	2.6	1.7	1.0
C	34.4	10.9	6.4	3.6	3.5	2.4	1.5	1.4	1.2
Si	18.7	7.5	5.2	3.6	3.7	1.7	1.2	0.8	0.6
Mg	26.2	12.3	8.4	4.9	4.6	2.7	1.8	1.2	0.7
O	24.9	12.2	8.8	5.9	5.1	3.8	2.1	1.4	1.0

Table B.30: Diffusivity values at 4,000 K reported as 10^9 m^2/s for Figure 4.18b.

Coordination number	5 GPa, 3000 K	5 GPa, 4000 K	46 GPa, 3000 K	46 GPa, 4000 K
2	6	8	0	0
3	18	21	0	0
4	24	26	0	0
5	22	20	3	4
6	18	14	16	16
7	8	8	30	31
8	2	3	29	29
9	0	1	15	14
10	0	0	5	5
11	0	0	1	1

Table B.31: Fe coordination number abundances for Figure 4.13.

Coordination number	5 GPa, 3000 K	5 GPa, 4000 K	46 GPa, 3000 K	46 GPa, 4000 K
2	2	3	0	0
3	12	16	0	0
4	26	29	0	1
5	28	27	5	6
6	22	17	24	26
7	8	7	41	39
8	1	1	24	22
9	0	0	5	5

Table B.32: Mg coordination number abundances for Figure 4.13.

Coordination number	5 GPa, 3000 K	5 GPa, 4000 K	46 GPa, 3000 K	46 GPa, 4000 K
2	2	6	0	0
3	10	24	0	0
4	80	58	12	22
5	7	10	46	49
6	0	1	41	26
7	0	0	1	1

Table B.33: Si coordination number abundances for Figure 4.13.

Coordination number	5 GPa, 3000 K	5 GPa, 4000 K	46 GPa, 3000 K	46 GPa, 4000 K
2	27	33	5	8
3	47	35	44	51
4	5	6	46	36
5	0	0	5	5

Table B.34: C coordination number abundances for Figure 4.13.

APPENDIX C

SUPPLEMENTAL MATERIAL FOR CHAPTER 5

Melt	Pressure (GPa)	Density (g/cc)	Molar Volume (cc/mol)
$MgCO_3$	1.12	1.37	12.31
	3.64	1.85	9.11
	11.5	2.46	6.85
	42.9	3.36	5.02
	78.2	3.92	4.30
	109.0	4.31	3.91
	138.0	4.61	3.66

Table C.1: Densities and molar volumes of $MgCO_3$ melt at different pressures for Figure 5.1 and Figure 5.2.

Melt	Pressure (GPa)	Density (g/cc)	Molar Volume (cc/mol)
$MgSiO_3$	-0.76	1.63	12.32
	1.35	2.2	9.13
	11.5	2.93	6.85
	51.9	4.0	5.02
	96.6	4.67	4.30
	142.0	5.14	3.91
	182.0	5.49	3.66

Table C.2: Densities and molar volumes of $MgSiO_3$ melt at different pressures for Figure 5.1 and Figure 5.2.

Melt	Pressure (GPa)	Density (g/cc)	Molar Volume (cc/mol)
Fe	3.16	4.89	11.42
	26.2	6.94	8.05
	65.9	8.6	6.46
	81.5	9.17	6.09
	113.0	10.02	5.57

Table C.3: Densities and molar volumes of Fe melt at different pressures for Figure 5.1 and Figure 5.2.

Melt	Pressure (GPa)	Density (g/cc)	Molar Volume (cc/mol)
$Mg(C,Si)O_3$	0.24	1.5	12.31
	2.28	2.03	9.1
	11.5	2.69	6.87
	47.3	3.68	5.02
	86.2	4.29	4.31
	122.0	4.73	3.9
	158.0	5.05	3.66

Table C.4: Densities and molar volumes of carbonate-silicate melt at different pressures for Figure 5.1 and Figure 5.2.

Melt	Pressure (GPa)	Density (g/cc)	Molar Volume (cc/mol)
$MgCO_3$ + 13Fe	1.66	1.86	12.31
	2.28	2.03	9.1
	3.07	2.18	6.87
	5.8	2.51	5.02
	20.4	3.34	4.31
	73.6	4.57	3.9
	130.0	5.33	3.66

Table C.5: Densities and molar volumes of carbonate-metal melt at different pressures for Figure 5.1 and Figure 5.2.

Melt	Pressure (GPa)	Density (g/cc)	Molar Volume (cc/mol)
$MgSiO_3$ + 13Fe	-0.02	2.12	11.11
	1.14	2.32	10.18
	2.01	2.48	9.48
	5.83	2.87	8.24
	27.1	3.81	6.19
	96.8	5.21	4.52
	171.0	6.07	3.88

Table C.6: Densities and molar volumes of silicate-metal melt at different pressures for Figure 5.1 and Figure 5.2.

Melt	Pressure (GPa)	Density (g/cc)	Molar Volume (cc/mol)
$Mg(C,Si)O_3$ + 13Fe	0.86	1.99	11.12
	13.6	3.21	6.89
	25.4	3.67	6.03
	46.2	4.22	5.24
	51.9	4.34	5.1
	73.8	4.74	4.67
	93.4	5.04	4.39
	118.0	5.35	4.14
	148.0	5.7	3.88

Table C.7: Densities and molar volumes of carbonate-silicate-metal melt at different pressures for Figure 5.1 and Figure 5.2.

REFERENCES

Agrosì, G., Tempesta, G., Mele, D., Caggiani, M.C., Mangone, A., Della Ventura, G., Cestelli-Guidi, M., Allegretta, I., Hutchison, M.T., Nimis, P., and Nestola, F. (2019), Multiphase inclusions associated with residual carbonate in a transition zone diamond from Juina (Brazil). Lithos, 350-351, 105279.

Akahama, Y. and Kawamura, H. (2006) Pressure calibration of diamond anvil Raman gauge to 310 GPa. Journal of Applied Physics 100, 043516.

Andersen, O.K. (1975) Linear methods in band theory. Physical Review B 12, 3060-3083.

Antončík, E. (1959) Approximate formulation of the orthogonalized plane-wave method. Journal of Physics and Chemistry of Solids 10, 314-320.

Anzellini, S., Dewaele, A., Mezouar, M., Loubeyre, P. and Morard, G. (2013) Melting of iron at Earth's inner core boundary based on fast X-ray diffraction. Science 340, 464-466.

Arapan, S. and Ahuja, R. (2010) High-pressure phase transformations in carbonates. Physical Review B 82.

Arima, M., Kozai, Y. and Akaishi, M. (2002) Diamond nucleation and growth by reduction of carbonate melts under high-pressure and high-temperature conditions. Geology 30, 691.

Armstrong, L.S., Hirschmann, M.M., Stanley, B.D., Falksen, E.G. and Jacobsen, S.D. (2015) Speciation and solubility of reduced C–O–H–N volatiles in mafic melt: Implications for volcanism, atmospheric evolution, and deep volatile cycles in the terrestrial planets. Geochimica et Cosmochimica Acta 171, 283-302.

Bajgain, S. K., and Mookherjee M. (2021), Carbon bearing aluminosilicate melt at high pressure. Geochimica et Cosmochimica Acta, 312, 106-123.

Belonoshko, A.B., Lukinov, T., Rosengren, A., Bryk, T., and Litasov, K.D. (2015), Synthesis of heavy hydrocarbons at the core-mantle boundary. Scientific Reports, 5, 18382.

Biellmann, C., Gillet, P., Guyot, F.o., Peyronneau, J. and Reynard, B. (1993) Experimental evidence for carbonate stability in the Earth's lower mantle. Earth and Planetary Science Letters 118, 31-41.

Blochl, P. E. (1994), Projector augmented-wave method. Physical Review B, 50(24), 17953-17979.

Bodeving, S., Williams-Jones, A.E., and Swinden, S. (2017), Carbonate–silicate melt immiscibility, REE mineralising fluids, and the evolution of the Lofdal Intrusive Suite, Namibia. Lithos, 268-271, 383-398.

Boulard, E., Gloter, A., Corgne, A., Antonangeli, D., Auzende, A.L., Perrillat, J.P., Guyot, F. and Fiquet, G. (2011) New host for carbon in the deep Earth. Proceedings of the National Academy of Sciences of the United States of America 108, 5184-5187.

Boulard, E., Pan, D., Galli, G., Liu, Z., and Mao, W.L. (2015), Tetrahedrally coordinated carbonates in Earth's lower mantle. Nature Communications, 6, 6311.

Brey, G., Brice, W.R., Ellis, D.J., Green, D.H., Harris, K.L. and Ryabchikov, I.D. (1983) Pyroxene-carbonate reactions in the upper mantle. Earth and Planetary Science Letters 62, 63-74.

Campbell, A.J., Danielson, L., Righter, K., Seagle, C.T., Wang, Y.B. and Prakapenka, V.B. (2009) High pressure effects on the iron-iron oxide and nickel-nickel oxide oxygen fugacity buffers. Earth and Planetary Science Letters 286, 556-564.

Caracas, R., Hirose, K., Nomura, R., and Ballmer, M.D. (2019), Melt–crystal density crossover in a deep magma ocean. Earth and Planetary Science Letters, 516, 202-211.

Cerantola, V., Bykova, E., Kupenko, I., Merlini, M., Ismailova, L., McCammon, C., Bykov, M., Chumakov, A.I., Petitgirard, S., Kantor, I., Svitlyk, V., Jacobs, J., Hanfland, M., Mezouar, M., Prescher, C., Ruffer, R., Prakapenka, V.B. and Dubrovinsky, L. (2017) Stability of iron-bearing carbonates in the deep Earth's interior. Nature Communications 8, 15960.

Chao, E.C.T., Fahey, J.J., Littler, J. and Milton, D.J. (1962) Stishovite, SiO_2, a very high pressure new mineral from Meteor Crater, Arizona. Journal of Geophysical Research 67, 419-421.

Chi, H., Dasgupta, R., Duncan, M.S. and Shimizu, N. (2014) Partitioning of carbon between Fe-rich alloy melt and silicate melt in a magma ocean – Implications for the abundance and origin of volatiles in Earth, Mars, and the Moon. Geochimica et Cosmochimica Acta 139, 447-471.

Choudhary, K. and Tavazza, F. (2019) Convergence and machine learning predictions of Monkhorst-Pack *k*-points and plane-wave cut-off in high-throughput DFT calculations. Computational Materials Science 161.

Clift, P.D. (2017) A revised budget for Cenozoic sedimentary carbon subduction. Reviews of Geophysics 55, 97-125.

Dalou, C., Koga, K.T., Hammouda, T. and Poitrasson, F. (2009) Trace element partitioning between carbonatitic melts and mantle transition zone minerals: Implications for the source of carbonatites. Geochimica et Cosmochimica Acta 73, 239-255.

Dasgupta, R., Chi, H., Shimizu, N., Buono, A.S., and Walker, D. (2013), Carbon solution and partitioning between metallic and silicate melts in a shallow magma ocean: Implications for the origin and distribution of terrestrial carbon. Geochimica et Cosmochimica Acta, 102, 191-212.

Dasgupta, R. and Hirschmann, M.M. (2006) Melting in the Earth's deep upper mantle caused by carbon dioxide. Nature 440, 659-662.

Dasgupta, R., and Hirschmann, M.M. (2010), The deep carbon cycle and melting in Earth's interior. Earth and Planetary Science Letters, 298(1-2), 1-13.

Dasgupta, R., Hirschmann, M.M., and Smith, N.D. (2007), Water follows carbon: CO_2 incites deep silicate melting and dehydration beneath mid-ocean ridges. Geology, 35(2), 135.

Dasgupta, R. and Walker, D. (2008) Carbon solubility in core melts in a shallow magma ocean environment and distribution of carbon between the Earth's core and the mantle. Geochimica et Cosmochimica Acta 72, 4627-4641.

Dobretsov, N.L. and Shatskiy, A.F. (2012) Deep carbon cycle and geodynamics: the role of the core and carbonatite melts in the lower mantle. Russian Geology and Geophysics 53, 1117-1132.

de Koker, N. P., Stixrude, L., and Karki, B.B. (2008), Thermodynamics, structure, dynamics, and freezing of Mg_2SiO_4 liquid at high pressure. Geochimica et Cosmochimica Acta, 72(5), 1427-1441.

Dorfman, S. M., Badro, J., Nabiei, F., Prakapenka, V., Cantoni, M., and P. Gillet (2018), Carbonate stability in the reduced lower mantle. Earth and Planetary Science Letters, 489, 84-91.

Drewitt, J.W.E., Walter, M.J., Zhang, H., McMahon, S.C., Edwards, D., Heinen, B.J., Lord, O.T., Anzellini, S. and Kleppe, A.K. (2019) The fate of carbonate in oceanic crust subducted into Earth's lower mantle. Earth and Planetary Science Letters 511, 213-222.

Du, X., Wu, M., Tse, J.S., and Pan, Y. (2017), Structures and transport properties of $CaCO_3$ melts under Earth's mantle conditions. ACS Earth and Space Chemistry, 2(1), 1-8.

Fichtner, C. E., Schmidt, M.W., Liebske, C., Bouvier, A.S., and Baumgartner, L.P. (2021), Carbon partitioning between metal and silicate melts during Earth accretion. Earth and Planetary Science Letters, 554, 116659.

Finger, L. W., and Hazen, R.M. (2000), Systematics of high-pressure silicate structures. Reviews in Mineralogy and Geochemistry, 41(1), 123-155.

Fiquet, G., Badro, J., Gregoryanz, E., Fei, Y. and Occelli, F. (2009) Sound velocity in iron carbide (Fe_3C) at high pressure: Implications for the carbon content of the Earth's inner core. Physics of the Earth and Planetary Interiors 172, 125-129.

Fischer, R.A., Campbell, A.J., Caracas, R., Reaman, D.M., Dera, P. and Prakapenka, V.B. (2012) Equation of state and phase diagram of Fe-16Si alloy as a candidate component of Earth's core. Earth and Planetary Science Letters 357, 268-276.

Fischer, R.A., Campbell, A.J., Caracas, R., Reaman, D.M., Heinz, D.L., Dera, P. and Prakapenka, V.B. (2014) Equations of state in the Fe-FeSi system at high pressures and temperatures. Journal of Geophysical Research: Solid Earth 119, 2810-2827.

Fischer, R.A., Campbell, A.J., Lord, O.T., Shofner, G.A., Dera, P. and Prakapenka, V.B. (2011) Phase transition and metallization of FeO at high pressures and temperatures. Geophysical Research Letters 38.

Fischer, R. A., Cottrell, E., Hauri, E., Lee, K.K.M., and Le Voyer, M. (2020), The carbon content of Earth and its core. Proceedings of the National Academy of Sciences of the United States of America 117, 8743-8749.

Fischer, R.A., Nakajima, Y., Campbell, A.J., Frost, D.J., Harries, D., Langenhorst, F., Miyajima, N., Pollok, K. and Rubie, D.C. (2015) High pressure metal-silicate partitioning of Ni, Co, V, Cr, Si, and O. Geochimica Et Cosmochimica Acta 167, 177-194.

Frost, D.J., Liebske, C., Langenhorst, F., McCammon, C.A., Tronnes, R.G. and Rubie, D.C. (2004) Experimental evidence for the existence of iron-rich metal in the Earth's lower mantle. Nature 428, 409-412.

Gaillard, F., Malki, M., Iacono-Marziano, G., Pichavant, M. and Scaillet, B. (2008) Carbonatite melts and electrical conductivity in the asthenosphere. Science 322, 1363-1365.

Ganguly, J. (2001) Thermodynamic modeling of solid solutions, Geiger, C.A. (Ed.), Solid Solutions in Silicate and Oxide Systems. European Mineralogical Union Notes in Mineralogy, Etvs University Press, Budapest, pp. 37-70.

Garnero, E.J. and McNamara, A.K. (2008) Structure and dynamics of Earth's lower mantle. Science 320, 626-628.

Gavryushkin, P.N., Martirosyan, N.S., Inerbaev, T.M., Popov, Z.I., Rashchenko, S.V., Likhacheva, A.Y., Lobanov, S.S., Goncharov, A.F., Prakapenka, V.B. and Litasov, K.D. (2017) Aragonite-II and $CaCO_3$-VII: new high-pressure, high-temperature polymorphs of $CaCO_3$. Crystal Growth and Design 17, 6291-6296.

Gavryushkin, P.N., Sagatova, D.N., Sagatov, N. and Litasov, K.D. (2021) Formation of Mg-orthocarbonate through the reaction $MgCO_3 + MgO = Mg_2CO_4$ at Earth's lower mantle P–T conditions. Crystal Growth & Design 21, 2986-2992.

Genge, M.J., Price, G.D. and Jones, A.P. (1995) Molecular dynamics simulations of $CaCO_3$ melts to mantle pressures and temperatures: implications for carbonatite magmas. Earth and Planetary Science Letters 131, 225-238.

Ghosh, D. B., Bajgain, S.K., Mookherjee, M., and Karki, B.B. (2017), Carbon-bearing silicate melt at deep mantle conditions. Scientific Reports, 7(1), 848.

Ghosh, D. B., and Karki, B.B. (2017), Transport properties of carbonated silicate melt at high pressure. Science Advances, 3(12), e1701840.

Ghosh, D. B., and Karki, B.B. (2020), Effects of valence and spin of Fe in $MgSiO_3$ melts: Structural insights from first-principles molecular dynamics simulations. Geochimica et Cosmochimica Acta, 279, 107-118.

Ghosh, D. B., Karki, B.B., and Stixrude, L. (2014), First-principles molecular dynamics simulations of $MgSiO_3$ glass: Structure, density, and elasticity at high pressure, American Mineralogist, 99(7), 1304-1314.

Ghosh, S., Ohtani, E., Litasov, K., Suzuki, A. and Sakamaki, T. (2007) Stability of carbonated magmas at the base of the Earth's upper mantle. Geophysical Research Letters 34.

Grewal, D. S., Dasgupta, R., and Aithala S. (2021), The effect of carbon concentration on its core-mantle partitioning behavior in inner Solar System rocky bodies. Earth and Planetary Science Letters, 571, 117090.

Gu, C., Catalli, K., Grocholski, B., Gao, L, Alp, E., Chow, P., Xiao, Y., Cynn, H., Evans, W.J., and Shim, S.H. (2012), Electronic structure of iron in magnesium silicate glasses at high pressure. Geophysical Research Letters, 39(24).

Hamann, D.R., Schlüter, M. and Chiang, C. (1979) Norm-conserving pseudopotentials. Physical Review Letters 43, 1494-1497.

Hammouda, T. (2003) High-pressure melting of carbonated eclogite and experimental constraints on carbon recycling and storage in the mantle. Earth and Planetary Science Letters 214, 357-368.

Hayden, L.A. and Watson, E.B. (2008) Grain boundary mobility of carbon in Earth's mantle: a possible carbon flux from the core. Proceedings of the National Academy of Sciences of the United States of America 105, 8537-8541.

Hayes, J.M. and Waldbauer, J.R. (2006) The carbon cycle and associated redox processes through time. Philosophical Transactions of the Royal Society B: Biological Sciences 361, 931-950.

Henkelman, G., Arnaldsson, A., and Jónsson, H. (2006), A fast and robust algorithm for Bader decomposition of charge density. Computational Materials Science, 36(3), 354-360.

Herring, C. (1940) A new method for calculating wave functions in crystals. Physical Review 57, 1169-1177.

Hoover, W. G. (1985), Canonical dynamics: Equilibrium phase-space distributions. Physical Review A: General Physics, 31(3), 1695-1697.

Isshiki, M., Irifune, T., Hirose, K., Ono, S., Ohishi, Y., Watanuki, T., Nishibori, E., Takata, M. and Sakata, M. (2004) Stability of magnesite and its high-pressure form in the lowermost mantle. Nature 427, 60-63.

Javoy, M. (1997) The major volatile elements of the Earth: Their origin, behavior, and fate. Geophysical Research Letters 24, 177-180.

Kakizawa, S., Inoue, T., Suenami, H. and Kikegawa, T. (2015) Decarbonation and melting in $MgCO_3$–SiO_2 system at high temperature and high pressure. Journal of Mineralogical and Petrological Sciences 110, 179-188.

Kamenetsky, V.S. and Yaxley, G.M. (2015) Carbonate–silicate liquid immiscibility in the mantle propels kimberlite magma ascent. Geochimica et Cosmochimica Acta 158, 48-56.

Kaminsky, F.V., Ryabchikov, I.D. and Wirth, R. (2015) A primary natrocarbonatitic association in the Deep Earth. Mineralogy and Petrology 110, 387-398.

Kaminsky, F., Wirth, R., Matsyuk, S., Schreiber, A. and Thomas, R. (2009) Nyerereite and nahcolite inclusions in diamond: evidence for lower-mantle carbonatitic magmas. Mineralogical Magazine 73, 797-816.

Karki, B. B., Bhattarai, D., Mookherjee, M., and Stixrude, L. (2009), Visualization-based analysis of structural and dynamical properties of simulated hydrous silicate melt. Physics and Chemistry of Minerals, 37(2), 103-117.

Karki, B. B., Bhattarai, D., and Stixrude, L. (2007), First-principles simulations of liquid silica: Structural and dynamical behavior at high pressure, Physical Review B, 76(10).

Karki, B. B., Ghosh, D.B., and Banjara, D. (2020), Mixed incorporation of carbon and hydrogen in silicate melts under varying pressure and redox conditions. Earth and Planetary Science Letters, 549, 116520.

Karki, B. B., Ghosh, D.B., Maharjan, C., Karato, S,-i., and Park, J. (2018), Density-pressure profiles of Fe-bearing $MgSiO_3$ liquid: Effects of valence and spin states, and implications for the chemical evolution of the lower mantle. Geophysical Research Letters, 45(9), 3959-3966.

Kelemen, P. B., and Manning, C.E. (2015), Reevaluating carbon fluxes in subduction zones, what goes down, mostly comes up. Proceedings of the National Academy of Sciences of the United States of America, 112(30), E3997-4006.

Kerrick, D.M. (2001) Present and past nonanthropogenic CO_2 degassing from the solid earth. Reviews of Geophysics 39, 565-585.

Kim, E.J., Fei, Y. and Lee, S.K. (2018) Effect of pressure on the short-range structure and speciation of carbon in alkali silicate and aluminosilicate glasses and melts at high pressure up to 8 GPa: ^{13}C, ^{27}Al, ^{17}O, and ^{29}Si solid-state NMR study. Geochimica et Cosmochimica Acta 224, 327-343.

Kraft, S., Knittle, E. and Williams, Q. (1991) Carbonate stability in the Earth's mantle: A vibrational spectroscopic study of aragonite and dolomite at high pressures and temperatures. Journal of Geophysical Research 96, 17997.

Kohn, W. and Sham, L.J. (1965) Self-consistent equations including exchange and correlation effects. Physical Review 140, A1133-A1138.

Korsakov, A. V., and Hermann, J. (2006), Silicate and carbonate melt inclusions associated with diamonds in deeply subducted carbonate rocks. Earth and Planetary Science Letters, 241(1-2), 104-118.

Koura, N., Kohara, S., Takeuchi, K., Takahashi, S., Curtiss, L.A., Grimsditch, M., and Saboungi, M.-L. (1996), Alkali carbonates: Raman spectroscopy, *ab initio* calculations, and structure. Journal of Molecular Structure, 382(3), 163-169.

Kresse, G., and Furthmuller, J. (1996), Efficient iterative schemes for *ab initio* total-energy calculations using a plane-wave basis set. Physical Review B: Condensed Matter, 54(16), 11169-11186.

Kubicki, J. D., and Stolper, E.M. (1995), Structural roles of CO_2 and $[CO_3]^{2-}$ in fully polymerized sodium aluminosilicate melts and glasses. Geochimica et Cosmochimica Acta, 59(4), 683-698.

Kushiro, I. (1975) Carbonate-silicate reactions at high presures and possible presence of dolomite and magnesite in the upper mantle. Earth and Planetary Science Letters 28, 116-120.

Labrosse, S., Hernlund, J.W. and Coltice, N. (2007) A crystallizing dense magma ocean at the base of the Earth's mantle. Nature 450, 866-869.

Lee, S. K. (2014), Absence of pressure-induced electron spin-state transition of iron in silicate glasses upon compression. American Mineralogist, 99(5-6), 877-878.

Lee, W. J., and Wyllie, P.J. (1998), Processes of crustal carbonatite formation by liquid immiscibility and differentiation, elucidated by model systems. Journal of Petrology, 39(11-12), 2005-2013.

Lesher, C. E., Hervig, R.L., and Tinker, D. (1996), Self diffusion of network formers (silicon and oxygen) in naturally occurring basaltic liquid. Geochimica et Cosmochimica Acta, 60(3), 405-413.

Li, J., Mao, H.K., Fei, Y., Gregoryanz, E., Eremets, M. and Zha, C.S. (2002) Compression of Fe_3C to 30 GPa at room temperature. Physics and Chemistry of Minerals 29, 166-169.

Li, M., McNamara, A.K., Garnero, E.J. and Yu, S. (2017a) Compositionally-distinct ultra-low velocity zones on Earth's core-mantle boundary. Nature Communications 8, 177.

Li, X., Zhang, Z., Lin, J.F., Ni, H., Prakapenka, V.B. and Mao, Z. (2018) New high-pressure phase of $CaCO_3$ at the topmost lower mantle: Implication for the deep-mantle carbon transportation. Geophysical Research Letters 45, 1355-1360.

Li, Y., Dasgupta, R. and Tsuno, K. (2015) The effects of sulfur, silicon, water, and oxygen fugacity on carbon solubility and partitioning in Fe-rich alloy and silicate melt systems at 3 GPa and 1600 °C: Implications for core–mantle differentiation and degassing of magma oceans and reduced planetary mantles. Earth and Planetary Science Letters 415, 54-66.

Li, Z.Y., Li, J., Lange, R., Liu, J.C., and Mintzer, B. (2017), Determination of calcium carbonate and sodium carbonate melting curves up to Earth's transition zone pressures with implications for the deep carbon cycle. Earth and Planetary Science Letters, 457, 395-402.

Liu, J., Fu, S. and Lin, J.-F. (2020) Spin transition of iron in deep-mantle ferromagnesite, Carbon in Earth's Interior, pp. 115-125.

Liu, J., Lin, J.-F., Prakapenka, V.B., Prescher, C. and Yoshino, T. (2016) Phase relations of Fe_3C and Fe_7C_3 up to 185 GPa and 5200 K: Implication for the stability of iron carbide in the Earth's core. Geophysical Research Letters 43, 12,415-412,422.

Liu, L., Yang, L., Zhuang, C., Yang, G., Yi, L., Liu, H., Sun, F., Gu, X., Wang, H. and Xu, J. (2021) Diffusion of CO_2 in magnesite under high pressure and high temperature from molecular dynamics simulations. Geofluids 2021, 1-9.

Lobanov, S.S., Dong, X., Martirosyan, N.S., Samtsevich, A.I., Stevanovic, V., Gavryushkin, P.N., Litasov, K.D., Greenberg, E., Prakapenka, V.B., Oganov, A.R. and Goncharov, A.F. (2017) Raman spectroscopy and x-ray diffraction of sp^3 $CaCO_3$ at lower mantle pressures. Physical Review B 96.

Lv, M., Dorfman, S.M., Badro, J., Borensztajn, S., Greenberg, E., and Prakapenka, V.B. (2021), Reversal of carbonate-silicate cation exchange in cold slabs in Earth's lower mantle. Nature Communications, 12(1), 1712.

Maeda, F., Kamada, S., Ohtani, E., Hirao, N., Mitsui, T., Masuda, R., Miyahara, M., and McCammon, C. (2017), Spin state and electronic environment of iron in basaltic glass in the lower mantle. American Mineralogist, 102(10), 2106-2112.

Manning, C.E., Shock, E.L. and Sverjensky, D.A. (2013) The chemistry of carbon in aqueous fluids at crustal and upper-mantle conditions: experimental and theoretical constraints. Reviews in Mineralogy and Geochemistry 75, 109-148.

Mao, Z., Lin, J.F., Yang, J., Wu, J., Watson, H.C., Xiao, Y., Chow, P., and Zhao, J. (2014), Spin and valence states of iron in Al-bearing silicate glass at high pressures studied by synchrotron Mossbauer and X-ray emission spectroscopy. American Mineralogist, 99(2-3), 415-423.

Martirosyan, N.S., Litasov, K.D., Shatskiy, A. and Ohtani, E. (2015a) The reactions between iron and magnesite at 6 GPa and 1273–1873 K: Implication to reduction of subducted carbonate in the deep mantle. Journal of Mineralogical and Petrological Sciences 110, 49-59.

Martirosyan, N.S., Litasov, K.D., Shatskiy, A.F. and Ohtani, E. (2015b) Reactions of iron with calcium carbonate at 6 GPa and 1273–1873 K: Implications for carbonate reduction in the deep mantle. Russian Geology and Geophysics 56, 1322-1331.

Martirosyan, N. S., Yoshino, T., Shatskiy, A., Chanyshev, A.D., and Litasov, K.D. (2016), The $CaCO_3$-Fe interaction: Kinetic approach for carbonate subduction to the deep Earth's mantle. Physics of the Earth and Planetary Interiors, 259, 1-9.

Marty, B. (2012) The origins and concentrations of water, carbon, nitrogen and noble gases on Earth. Earth and Planetary Science Letters 313-314, 56-66.

Marx, D. and Hutter, J. (2009) *Ab initio* molecular dynamics: basic theory and advanced methods. Cambridge University Press.

McDonough, W.F. (2003) Compositional model for the Earth's core, in *The Mantle and Core* (Ed. R. W. Carlson), Vol. 3 *Treatise on Geochemistry* (Eds. H. D. Holland and K. K. Turekian), Elsevier-Pergamon, Oxford, pp. 547-568.

McDonough, W.F. and Sun, S.s. (1995) The composition of the Earth. Chemical Geology 120, 223-253.

McCammon, C., Glazyrin, K., Kantor, A., Kantor, I., Kupenko, I., Narygina, O., Potapkin, V., Prescher, C., Sinmyo, R., Chumakov, A., Rüffer, R., Sergueev, Il, Smirnov, G., Dubrovinsky, L.

(2013), Iron spin state in silicate perovskite at conditions of the Earth's deep interior. High Pressure Research, 33(3), 663-672.

Mergner, V., Kupenko, I., Spiekermann, G., Petitgirard, S., Libon, L., Chariton, S., Krug, M., Steinbrügge, R., Sergueev, I. and Sanchez-Valle, C. (2021) Sound velocities in FeSi at lower mantle conditions and the origin of ultralow-velocity zones. Geophysical Research Letters 48.

Merlini, M., Cerantola, V., Gatta, G.D., Gemmi, M., Hanfland, M., Kupenko, I., Lotti, P., Müller, H. and Zhang, L. (2017) Dolomite-IV: Candidate structure for a carbonate in the Earth's lower mantle. American Mineralogist 102, 1763-1766.

Merlini, M., Crichton, W.A., Hanfland, M., Gemmi, M., Muller, H., Kupenko, I. and Dubrovinsky, L. (2012) Structures of dolomite at ultrahigh pressure and their influence on the deep carbon cycle. Proceedings of the National Academy of Sciences of the United States of America 109, 13509-13514.

Mysen, B.O., Kumamoto, K., Cody, G.D. and Fogel, M.L. (2011) Solubility and solution mechanisms of C–O–H volatiles in silicate melt with variable redox conditions and melt composition at upper mantle temperatures and pressures. Geochimica et Cosmochimica Acta 75, 6183-6199.

Nosé, S. (1984), A unified formulation of the constant temperature molecular dynamics methods. The Journal of Chemical Physics, 81(1), 511-519.

Oganov, A.R., Glass, C.W. and Ono, S. (2006) High-pressure phases of $CaCO_3$: Crystal structure prediction and experiment. Earth and Planetary Science Letters 241, 95-103.

Oganov, A. R., Ono, S., Ma, Y., Glass, C.W., and Garcia, A. (2008), Novel high-pressure structures of $MgCO_3$, $CaCO_3$ and CO_2 and their role in Earth's lower mantle. Earth and Planetary Science Letters, 273(1-2), 38-47.

Ono, S., Kikegawa, T. and Ohishi, Y. (2007) High-pressure transition of $CaCO_3$. American Mineralogist 92, 1246-1249.

Ono, S., Kikegawa, T., Ohishi, Y. and Tsuchiya, J. (2005) Post-aragonite phase transformation in $CaCO_3$ at 40 GPa. American Mineralogist 90, 667-671.

Palyanov, Y.N., Bataleva, Y.V., Sokol, A.G., Borzdov, Y.M., Kupriyanov, I.N., Reutsky, V.N. and Sobolev, N.V. (2013) Mantle-slab interaction and redox mechanism of diamond formation. Proceedings of the National Academy of Sciences of the United States of America 110, 20408-20413.

Payne, M.C., Joannopoulos, J.D., Allan, D.C., Teter, M.P. and Vanderbilt, D.H. (1986) Molecular dynamics and *ab initio* total energy calculations. Physical Review Letters 56, 2656.

Payne, M.C., Teter, M.P., Allan, D.C., Arias, T.A. and Joannopoulos, J.D. (1992) Iterative minimization techniques for *ab initio* total-energy calculations: molecular dynamics and conjugate gradients. Reviews of Modern Physics 64, 1045-1097.

Perdew, J.P. (1979) Orbital functional for exchange and correlation: self-interaction correction to the local density approximation. Chemical Physics Letters 64, 127-130.

Perdew, J.P. (1986) Density-functional approximation for the correlation energy of the inhomogeneous electron gas. Physical Review B: Condensed Matter 33, 8822-8824.

Perdew, J. P., Burke, K., and Ernzerhof, M. (1996), Generalized gradient approximation made simple. Physical Review Letters, 77(18), 3865-3868.

Phillips, J.C. and Kleinman, L. (1959) New method for calculating wave functions in crystals and molecules. Physical Review 116, 287-294.

Plank, T. and Manning, C.E. (2019) Subducting carbon. Nature 574, 343-352.

Prescher, C., Dubrovinsky, L., Bykova, E., Kupenko, I., Glazyrin, K., Kantor, A., McCammon, C., Mookherjee, M., Nakajima, Y., Miyajima, N., Sinmyo, R., Cerantola, V., Dubrovinskaia, N., Prakapenka, V., Ruffer, R., Chumakov, A. and Hanfland, M. (2015) High Poisson's ratio of Earth's inner core explained by carbon alloying. Nature Geoscience 8, 220-223.

Prescher, C. and Prakapenka, V.B. (2015) DIOPTAS: a program for reduction of two-dimensional X-ray diffraction data and data exploration. High Pressure Research 35, 223-230.

Prescher, C., Weigel, C., McCammon, C., Narygina, O., Potapkin, V., Kupenko, I., Sinmyo, R., Chumakov, A.I., and Dubrovinsky, L. (2014), Iron spin state in silicate glass at high pressure: Implications for melts in the Earth’s lower mantle. Earth and Planetary Science Letters, 385, 130-136.

Presnall, D.C. and Gudfinnsson, G.H. (2005) Carbonate-rich melts in the oceanic low-velocity zone and deep mantle. Geological Society of America Special Paper 388, 207-216.

Richet, P., Mao, H.-K. and Bell, P.M. (1988) Static compression and equation of state of CaO to 1.35 Mbar. Journal of Geophysical Research: Solid Earth 93, 15279-15288.

Rohrbach, A., and Schmidt, M.W. (2011), Redox freezing and melting in the Earth's deep mantle resulting from carbon-iron redox coupling. Nature, 472(7342), 209-212.

Ross, M., Mao, H.K., Bell, P.M. and Xu, J.A. (1986) The equation of state of dense argon - a comparison of shock and static studies. Journal of Chemical Physics 85, 1028-1033.

Ross, N.L. (1997) The equation of state and high-pressure behavior of magnesite. American Mineralogist 82, 682-688.

Sakamaki, T., Ohtani, E., Urakawa, S., Terasaki, H. and Katayama, Y. (2011) Density of carbonated peridotite magma at high pressure using an X-ray absorption method. American Mineralogist 96, 553-557.

Sanloup, C., Hudspeth, J.M., Afonina, V., Cochain, B., Konôpková, Z., Lelong, G., Cormier, L. and Cavallari, C. (2019) Polymerized 4-fold coordinated carbonate melts in the deep mantle. Frontiers in Earth Science 7.

Sano, Y. and Williams, S.N. (1996) Fluxes of mantle and subducted carbon along convergent plate boundaries. Geophysical Research Letters 23, 2749-2752.

Santos, S.S.M., Marcondes, M.L., Justo, J.F. and Assali, L.V.C. (2019) Stability of calcium and magnesium carbonates at Earth's lower mantle thermodynamic conditions. Earth and Planetary Science Letters 506, 1-7.

Santos, S.S.M., Marcondes, M.L., Justo, J.F. and Assali, L.V.C. (2020) Calcium carbonate at high pressures and high temperatures: A first-principles investigation. Physics of the Earth and Planetary Interiors 299, 106327.

Sanville, E., Kenny, S.D., Smith, R., and Henkelman, G. (2007), Improved grid-based algorithm for Bader charge allocation. Journal of Computational Chemistry, 28(5), 899-908.

Sen, S., Widgeon, S.J., Navrotsky, A., Mera, G., Tavakoli, A., Ionescu, E., and Riedel, R. (2013), Carbon substitution for oxygen in silicates in planetary interiors. Proceedings of the National Academy of Sciences of the United States of America, 110(40), 15904-15907.

Slater, J.C. (1937) Wave functions in a periodic potential. Physical Review 51, 846-851.

Smit, K.V., Stachel, T., Luth, R.W. and Stern, R.A. (2019) Evaluating mechanisms for eclogitic diamond growth: An example from Zimmi Neoproterozoic diamonds (West African craton). Chemical Geology.

Smith, E. M., Shirey, S.B., Nestola, F., Bullock, E.S., Wang, J., Richardson, S.H., and Wang, W. (2016), Large gem diamonds from metallic liquid in Earth's deep mantle. Science, 354(6318), 1403-1405.

Soler, J.M. and Williams, A.R. (1989) Simple formula for the atomic forces in the augmented-plane-wave method. Physical Review B: Condensed Matter 40, 1560-1564.

Solomatova, N. V., and Caracas, R. (2019), Pressure-induced coordination changes in a pyrolitic silicate melt from *ab initio* molecular dynamics simulations. Journal of Geophysical Research: Solid Earth, 124(11), 11232-11250.

Solomatova, N. V., and Caracas, R. (2021), Buoyancy and structure of volatile-rich silicate melts. Journal of Geophysical Research: Solid Earth, 126(2), e2020JB021045.

Solomatova, N., Caracas, R. and Cohen, R. (2020) Carbon speciation and solubility in silicate melts, Carbon in Earth's Interior, pp. 179-194.

Solomatova, N. V., Caracas, R., and Manning, C.E. (2019), Carbon sequestration during core formation implied by complex carbon polymerization. Nature Communications, 10(1).

Speziale, S., Milner, A., Lee, V.E., Clark, S.M., Pasternak, M.P., and Jeanloz, R. (2005), Iron spin transition in Earth's mantle. Proceedings of the National Academy of Sciences of the United States of America, 102(50), 17918-17922.

Stachel, T., and Luth, R.W. (2015), Diamond formation — Where, when and how?. Lithos, 220-223, 200-220.

Stagno, V., Frost, D.J., McCammon, C.A., Mohseni, H., and Fei, Y. (2015), The oxygen fugacity at which graphite or diamond forms from carbonate-bearing melts in eclogitic rocks. Contributions to Mineralogy and Petrology, 169(2).

Stagno, V., Ojwang, D.O., McCammon, C.A. and Frost, D.J. (2013) The oxidation state of the mantle and the extraction of carbon from Earth's interior. Nature 493, 84-88.

Stagno, V., Stopponi, V., Kono, Y., Manning, C.E. and Irifune, T. (2018) Experimental determination of the viscosity of Na_2CO_3 melt between 1.7 and 4.6 GPa at 1200–1700 °C: Implications for the rheology of carbonatite magmas in the Earth's upper mantle. Chemical Geology 501, 19-25.

Stagno, V., Tange, Y., Miyajima, N., McCammon, C.A., Irifune, T., and Frost, D.J. (2011), The stability of magnesite in the transition zone and the lower mantle as function of oxygen fugacity. Geophysical Research Letters, 38(19).

Stixrude, L., Lithgow-Bertelloni, C., Kiefer, B. and Fumagalli, P. (2007) Phase stability and shear softening in $CaSiO_3$ perovskite at high pressure. Physical Review B 75.

Stracke, A. (2012) Earth's heterogeneous mantle: A product of convection-driven interaction between crust and mantle. Chemical Geology 330-331, 274-299.

Sun, C. and Dasgupta, R. (2019) Slab–mantle interaction, carbon transport, and kimberlite generation in the deep upper mantle. Earth and Planetary Science Letters 506, 38-52.

Takafuji, N., Fujino, K., Nagai, T., Seto, Y. and Hamane, D. (2006) Decarbonation reaction of magnesite in subducting slabs at the lower mantle. Physics and Chemistry of Minerals 33, 651-654.

Tang, W., Sanville, E., and Henkelman G., (2009), A grid-based Bader analysis algorithm without lattice bias. Journal of Physics: Condensed Matter, 21(8), 084204.

Tao, R., Zhang, L., Li, S., Zhu, J., and Ke, S. (2018), Significant contrast in the Mg-C-O isotopes of carbonate between carbonated eclogite and marble from the S.W. Tianshan UHP subduction zone: Evidence for two sources of recycled carbon. Chemical Geology, 483, 65-77.

Thompson, E.C., Campbell, A.J. and Tsuchiya, J. (2021) Elastic properties of the pyrite-type FeOOH-AlOOH system from first-principles calculations. Geochemistry, Geophysics, Geosystems 22.

Thomson, A. R., Walter, J.M., Kohn, S.C., and Brooker, R.A. (2016), Slab melting as a barrier to deep carbon subduction. Nature, 529(7584), 76-79.

Vanderbilt, D. (1990) Soft self-consistent pseudopotentials in a generalized eigenvalue formalism. Physical Review B: Condensed Matter 41, 7892-7895.

Vennari, C.E. and Williams, Q. (2018) A novel carbon bonding environment in deep mantle high-pressure dolomite. American Mineralogist 103, 171-174.

Verlet, L. (1967) Computer "experiments" on classical fluids. I. Thermodynamical properties of Lennard-Jones molecules. Physical Review 159, 98-103.

Williams, Q. and Garnero, E.J. (1996) Seismic evidence for partial melt at the base of Earth's mantle. Science 273, 1528-1530.

Williams, Q., and Jeanloz, R. (1988), Spectroscopic evidence for pressure-induced coordination changes in silicate glasses and melts. Science 239(4842), 902-905.

Wohl, K. (1946) Thermodynamic evaluation of binary and ternary liquid systems. Transactions of the American Institute of Chemical Engineers 42, 215-249.

Wohl, K. (1953) Thermodynamic evaluation of binary and ternary liquid systems. Chemical Engineering Progress 49, 218-221.

Wood, B.J., Li, J. and Shahar, A. (2013) Carbon in the core: Its influence on the properties of core and mantle. Reviews in Mineralogy and Geochemistry 75, 231-250.

Xu, M., Jing, Z., Bajgain, S.K., Mookherjee, M., Van Orman, J.A., Yu, T., and Wang, Y. (2020), High-pressure elastic properties of dolomite melt supporting carbonate-induced melting in deep upper mantle. Proceedings of the National Academy of Sciences of the United States of America, 117(31), 18285-18291.

Xue, X., Kanzaki, M., Tronnes, R.G., and Stebbins, J.F. (1989), Silicon coordination and speciation changes in a silicate liquid at high pressures. Science, 245(4921), 962-964.

Yu, M., and Trinkle, D.R. (2011), Accurate and efficient algorithm for Bader charge integration. The Journal of Chemical Physics, 134(6), 064111.

Zhang, L., Yuan, H., Meng, Y. and Mao, H.K. (2018a) Discovery of a hexagonal ultradense hydrous phase in (Fe,Al)OOH. Proceedings of the National Academy of Sciences of the United States of America 115, 2908-2911.

Zhang, Y., and Yin, Q.Z. (2012), Carbon and other light element contents in the Earth's core based on first-principles molecular dynamics. Proceedings of the National Academy of Sciences of the United States of America, 109(48), 19579-19583.

Zhang, Z., Mao, Z., Liu, X., Zhang, Y. and Brodholt, J. (2018b) Stability and reactions of $CaCO_3$ polymorphs in the Earth's deep mantle. Journal of Geophysical Research: Solid Earth.

Zhang, Z., Stixrude, L. and Brodholt, J. (2013) Elastic properties of $MgSiO_3$ -perovskite under lower mantle conditions and the composition of the deep Earth. Earth and Planetary Science Letters 379, 1-12.

Zhao, G., Mu, H.F., Tan, X.M., Wang, D.H. and Yang, C.L. (2014) Structural and dynamical properties of $MgSiO_3$ melt over the pressure range 200–500 GPa: *Ab initio* molecular dynamics. Journal of Non-Crystalline Solids 385, 169-174.

Zhu, F., Li, J., Liu, J., Lai, X., Chen, B. and Meng, Y. (2019) Kinetic control on the depth distribution of superdeep diamonds. Geophysical Research Letters 46, 1984-1992.